The Pennsylvania State University

The Graduate School

Eberly College of Science

TOPOLOGICAL INSULATOR SYSTEMS WITH MAGNETISM

A Dissertation in

Physics

by

Joon Sue Lee

Submitted in Partial Fulfillment
of the Requirements
for the Degree of

Doctor of Philosophy

December 2014

The dissertation of Joon Sue Lee was reviewed and approved* by the following:

Nitin Samarth
Professor of Physics
George A. and Margaret M. Downsbrough Department Head of Physics
Dissertation Advisor
Chair of Committee

Jainendra K. Jain
Evan Pugh & Erwin Mueller Professor of Physics

Jun Zhu
Professor of Physics

Suman Datta
Professor of Electrical Engineering

*Signatures are on file in the Graduate School

ABSTRACT

This dissertation describes topological insulator systems hybridized with magnetism. The Dirac surface states induced by strong spin-orbit interaction can be modified by breaking time-reversal symmetry that protects the surface state. We study the modified surface states of topological insulators by introducing magnetism by doping magnetic atoms or interfacing a magnetic layer to the surface. Also, we explore potential spintronics applications of topological insulators by utilizing magnetic tunnel junctions to evidence the inherently spin-polarized texture of the topological insulator surface state. For this dissertation research, single crystalline topological insulator thin films grown by molecular beam epitaxy have been employed.

From the motivation of breaking time-reversal symmetry in the surface state, the first experiments study the structural, magnetic, and magneto-transport properties of a magnetically doped, three-dimensional topological insulator, bismuth telluride doped with Mn. We observed ferromagnetism with a Curie temperature up to 17 K in films with ~2-10% Mn concentrations. The observed ferromagnetism is independent of carrier density in the Mn-doped bismuth telluride films, suggesting that it is not mediated by charge carriers.

The next topological insulator system with magnetism is a hybrid topological insulator/ferromagnet heterostructure as a new approach for topological insulator hybrid systems using a dilute magnetic semiconductor $Ga_{1-x}Mn_xAs$. A highly resistive $Ga_{1-x}Mn_xAs$ with out-of-plane magnetic anisotropy is cleanly interfaced with a topological insulator $Bi_{2-x}Sb_xTe_{3-y}Se_y$ by molecular beam epitaxy. Magneto-transport measurements on a top-gated heterostructure device show a crossover from positive magneto-conductance to negative magneto-conductance as well as a systematic emergence of an anomalous Hall effect as the temperature is lowered or as the chemical potential approaches the Dirac point. The results are possibly interpreted as the modification of the surface state at the interface by the adjacent, ferromagnetic $Ga_{1-x}Mn_xAs$ layer.

The last topological insulator system with magnetism is a topological insulator channel with a magnetic tunnel junction on it. We seek a potential role of topological insulators in spintronics as generators of carrier spin polarization. Electrical detection of the inherent spin polarization of the topological insulator surface state was demonstrated using a permalloy/Al_2O_3 magnetic tunnel junction on a $(Bi,Sb)_2Te_3$ channel. The observed hysteretic spin signals occurring at the magnetic switching field of the ferromagnet permalloy layer can be interpreted as the projection of the current-induced spin polarization on a topological insulator surface onto the magnetization of the ferromagnet via tunneling.

TABLE OF CONTENTS

LIST OF FIGURES

LIST OF TABLES

ACKNOWLEDGEMENTS

I'm indebted to many people in and out of the lab for my Ph.D. journey. First of all, I would like to express my sincerest gratitude to my research advisor, Professor Nitin Samarth. With his knowledge and enthusiasm for physics, he guided me what is important in my field of study and what needs to be done for my dissertation research. I am grateful for his kind, patient encouragements when I met with some difficulties and frustrations. My committee members, Professor Jainendra K. Jain, Professor Jun Zhu, and Professor Suman Datta, deserve thanks for serving on my dissertation committee and for helpful comments.

I want to thank my collaborators and former and current group members. I wish to thank Dr. Anthony Richardella for lots of discussions, helps, and significant contributions to my research projects; Dr. Meng Zhu for helping me to learn low-temperature transport measurements and III-V MBE growth; and Dr. Benjamin Cooley for teaching me II-VI MBE growth. I would also like to thank Dr. Duming Zhang and Abhinav Kandala for useful and lively discussions on topological insulator projects; Dr. David Rench and Robert Fraleigh for SQUID measurements; Professor Chao-xing Liu for valuable discussions and theoretical supports; Dr. Weiwei Zhao for helping me to use dilution fridge; Dr. Julie A. Borchers at NIST for polarized neutron reflectivity measurements; Dr. Jing Tao at Brookhaven National Lab for TEM measurements; Thomas Flanagan for various LabVIEW programs. My appreciation extends to my labmates, Yu Pan, James Kally, Di Xiao, Eric Kamp, Susan Kempinger, Daniil Finkel, Dr. Jing Liang, Dr. Kriti Kohli, Dr. Andrew Balk, Dr. Mark Wilson, and Ming Yang for both professional and personal contributions.

I would like to give thanks to my family—my parents, Bang Weon Lee and Soon Ran Cho, my sisters, Joonha Lee and Jun Young Lee, and my wife, Hye Young (Grage) Rhee—for all their love and support in all my pursuits. Without this endless source of encouragement and

prayer, my Ph.D. journey would never have been possible. I give my special thanks to my loving wife Hye Young who has always understood and faithfully supported me during the final stages of my Ph.D.

I gratefully acknowledge the funding sources. My work was supported by ARO through the MURI program, by ONR, by DARPA, and by C-SPIN, one of six centers or STARnet, a Semiconductor Research Corporation program sponsored by MARCO and DARPA.

Chapter 1

Introduction

Topological insulator

In recent years, a new field of electrical states of matter, that of topological insulators, has been rapidly developing in condensed-matter physics [1, 2, 3]. Lots of theoretical as well as experimental efforts to understand physics in topological insulators have been made, and many research groups are seeking new particles, such as Majorana fermions [4], and possible applications of topological insulators for spintronics and quantum computing [5].

Topological insulators have an insulating bulk band and metallic boundaries (gapless edges or surface states) when placed next to an ordinary insulator or a vacuum. The metallic boundaries of topological insulators are protected by time-reversal (TR) symmetry, which will be discussed later in this section. The term topology comes from a mathematical study of the properties that remain under continuous deformations, including stretching, bending or twisting. For a classic example, a doughnut and a coffee cup have the same topology: they both have a hole through the entire shape and can be deformed smoothly from one to the other. On the other hand, a ball cannot be reshaped into a doughnut without cutting a hole in the ball. Thus a ball and a doughnut are in different topological equivalence classes. In condensed-matter physics, general Hamiltonians of many-particle systems with a bulk energy gap can be considered in terms of topology. A smooth deformation without cutting a hole can be replaced with a change in the Hamiltonian without closing the bulk energy gap. If two quantum states of the same topological class are placed next to each other, the gap at the interface between the two states does not need

to be closed. However, if two quantum states of different topological classes are interfaced, there will be gapless states at the interface. For example, when a topologically non-trivial insulator is facing a vacuum, there are gapless states between the insulator and vacuum.

The electronic states of matter can be categorized by the quantum-mechanical behavior of electrons in materials. The most basic state of matter is the insulating state, in which an energy gap separates the occupied valence band states from the empty conduction band states. Since the electrons of such an insulator (also called an "atomic insulator") are bound to atoms in closed orbitals, this insulating state is electrically inert and requires an input of extra energy to force out an electron.

In the early 1980s, a new quantum state was discovered in electrical systems, which shows the integer and the fractional quantum Hall effects [6, 7]. In the quantum Hall state, the electrons circulate in quantized orbits with an external magnetic field perpendicular to the two-dimensional (2D) electron gas, rather like electrons bound to atoms in an atomic insulator. The circulating electrons make the bulk of the 2D material insulating; however, an electrical current flows along the edges, as shown in Figures 1-1(a) and (b). The quantum-mechanically quantized circular orbits of electrons lead to quantized Landau levels $\epsilon_n = \hbar\omega_c(n + 1/2)$ with the cyclotron frequency $\omega_c = eB/m$. An energy gap $\hbar\omega_c$ separates the occupied states from the empty states, similarly to the energy gap in an atomic insulator.

A new quantum state in materials with a strong spin-orbit coupling, showing the quantum spin Hall effect, was theoretically predicted in 2006 [8]. In such quantum spin Hall insulators, also called 2D topological insulators, the role of the external magnetic field is played by the strong spin-orbit coupling. Each of the spin-up and spin-down electrons is in its own quantum Hall state, responding to opposite spin-orbit interactions. The bulk of a 2D topological insulator is insulating, with an energy gap separating the occupied and empty states, but the edges of the insulator have the spin-up and spin-down electrons propagating in opposite directions, as

illustrated in Figures 1-1(c) and (d). Shortly after the prediction of this new state, the quantum spin Hall state was experimentally observed in HgTe/CdTe quantum wells in 2007 [9].

The three-dimensional (3D) form of the quantum spin Hall effect with metallic surface states (the 3D version of the edge states) was theoretically predicted in a semiconducting alloy $Bi_{1-x}Sb_x$ with a large spin-orbit coupling [10], and, soon after, studies of spin-resolved, angle-resolved photoemission spectroscopy (ARPES) measurements mapped out the surface state of the proposed 3D topological insulator $Bi_{1-x}Sb_x$ in k-space [11]. The quantum spin Hall state (2D topological insulator) and 3D topological insulator will be detailed in the following subsections.

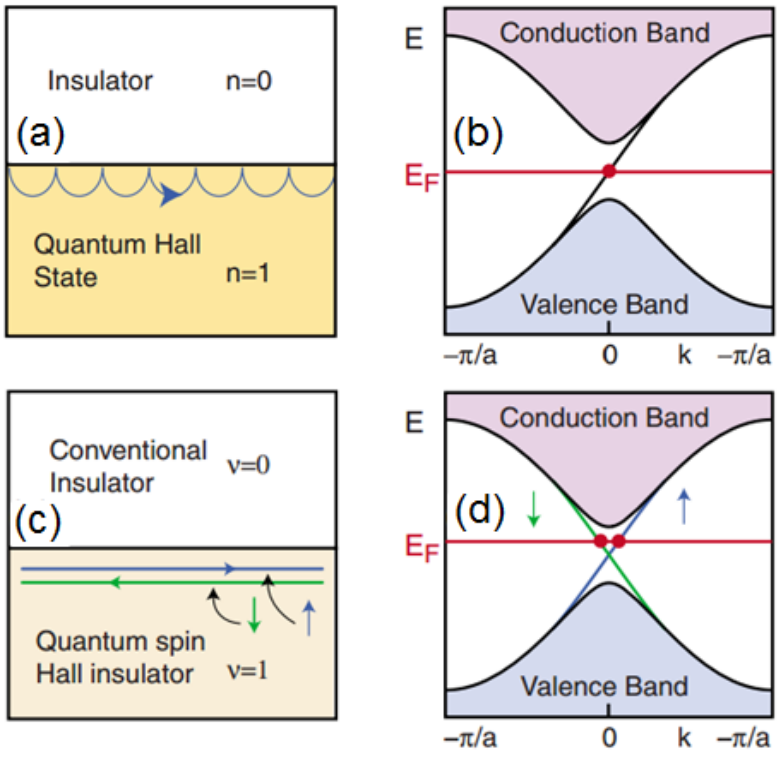

Figure 1-1. The edge states in the quantum Hall state (a,b) and the quantum spin Hall state (c,d). (a) A skipping cyclotron orbit at the interface between a quantum Hall insulator and an insulator. (b) An electrical structure of a semi-infinite strip shows a single edge state connecting the valence band and the conduction band. (c) At the interface between a quantum spin Hall insulator and a conventional insulator, spin-up and spin-down electrons propagate in opposite directions. (d) An electrical structure of two edge states with opposite spin directions. From reference [1].

2D topological insulator as a quantum spin Hall insulator

The edge states of the quantum spin Hall insulator show a "spin-filtered" property that spin-up and spin-down electrons propagate in the opposite directions. These propagation modes are strongly protected from backscattering by TR symmetry. TR symmetry refers to any symmetry of physical laws or systems under TR transformation. In the quantum spin Hall insulator case, TR switches both the direction of electron motion and the direction of spin, swapping the two propagation modes. Thus, the edge states of quantum spin Hall insulators are invariant under TR.

Observation of the edge states protected by TR symmetry is the key for the experimental realization of the quantum spin Hall effect. An initial proposal of the quantum spin Hall effect in graphene [12] turned out to be difficult to experimentally realize due to the weak spin-orbit interaction in graphene, which only opens an extremely small gap [13]. However, a quantized charge conductance in a quantum well structure of an HgTe thin layer sandwiched between two layers of CdTe, proposed by Bernevig and co-workers [8], was indeed experimentally observed by Konig and co-workers [9].

In the HgTe/CdTe semiconductor quantum well systems, the electronic state changes from a "normal" to an "inverted" type as the thickness of the quantum well varies. The barrier material CdTe has a normal ordering of the s-type Γ_6 band (conduction band) lying above the p-type Γ_8 band (valence band), while the well material HgTe has an inverted ordering of the Γ_6 band lying below the Γ_8 band, as shown in Figure 1-2(a). The band inversion is due to the strong spin-orbit coupling of the HgTe layer and depends on the thickness d of the HgTe layer. For d thinner than a certain critical thickness d_c, predicted to be around 6.5 nm, the quantum well is in the normal regime, where the energy of the lowest-energy conduction subband E1 is higher than

the energy of the highest-energy valence subband H1. For $d > d_c$, the quantum well is in the inverted regime, where H1 is above E1 [Figure 1-2(b)]. Thus, when $d = d_c$, the energy gap closes.

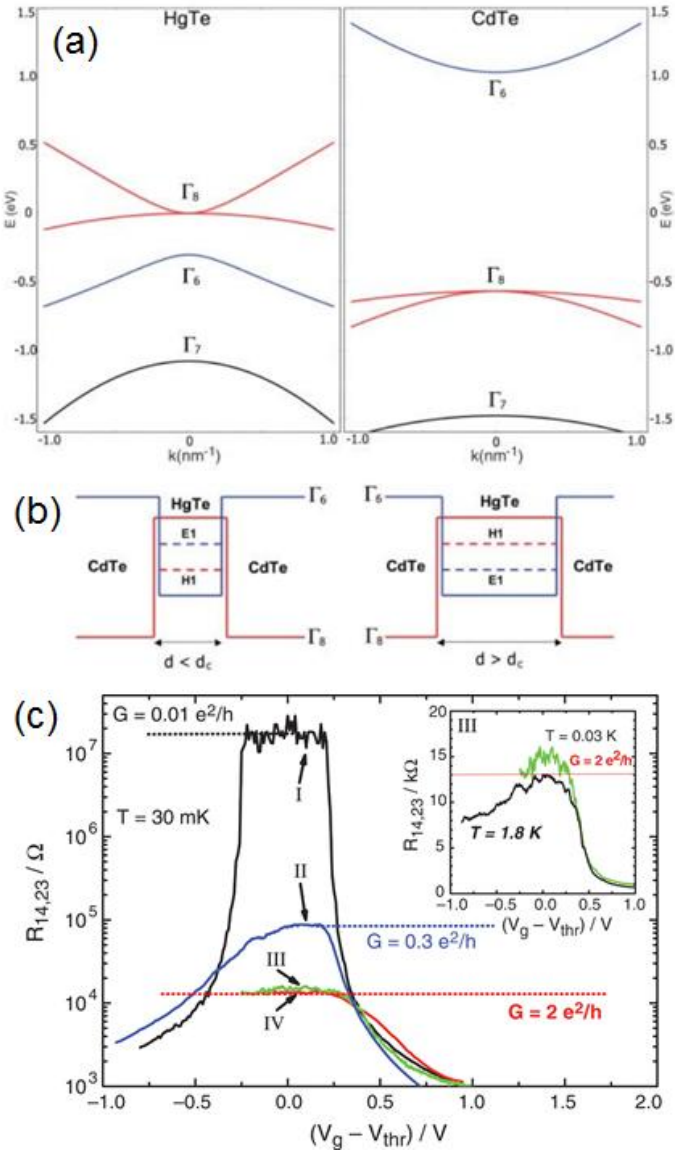

Figure 1-2. Theoretical prediction (a,b) and experimental observation (c) of the quantum spin Hall state. (a) Bulk energy bands of HgTe and CdTe near the Γ point. (b) The quantum wells in the normal regime ($d < d_c$) and in the inverted regime ($d > d_c$). (c) Experimental data of the longitudinal four-terminal resistance, $R_{14,23}$, in normal regime (d = 5.5 nm) (I) and in the inverted regime (d = 7.3 nm) (II, III, and IV) with respect to the gate voltage measured with B = 0 T at T = 30 mK. The inset shows $R_{14,23}(V_g)$ of two samples of the same device size (III) at 30 mK (green) and 1.8 K (black). From references [8] and [9].

The transition at $d = d_c$ is a topological quantum phase transition between a conventional, insulating phase and the quantum spin Hall phase with a single pair of helical edge states.

Konig and co-workers verified the prediction of the quantum spin Hall effect by measuring the resistance of HgTe/CdTe quantum wells with various HgTe thicknesses [9]. Thick quantum wells in the inverted regime (d > 6.3 nm) show the quantized resistance plateau of $R = h/e^2$ while thin quantum wells in the normal regime (d < 6.3 nm) have almost infinite resistance, as shown in Figure 1-2(c). The quantized resistance is due to the perfectly conducting edge states with the chemical potential tuned into the bulk band gap by applied gate voltage.

Surface states in 3D topological insulators

Similarly to the case of 2D topological insulators, theoretical predictions of a generalized form of the quantum spin Hall state in 3D were made before the experimental realization of the 3D form [14, 15, 16]. The term "topological insulator" was first used by Moore and Balents [15] to describe such TR-invariant band structures in 3D systems. Like the edge states of the 2D insulators, the electron propagation to any direction on a surface of a 3D topological insulator is strongly locked with the direction of its spin. This "surface state" is protected against backscattering by the TR symmetry. Under TR transformation, both the directions of the electron propagation and spin switch to be another propagation mode that has existed before the TR transformation. As predicted by Fu and Kane [10], the surface state was experimentally probed by ARPES on a surface of $Bi_{1-x}Sb_x$, the first 3D topological insulator [11].

Searches for promising candidates of 3D topological insulators were made on heavy-element, small-bandgap semiconductors in which spin-orbit coupling is strong enough to invert the electronic band structure at the Γ point but smaller than the size of the band gap in energy

scale. The efforts led to a discovery of so-called 2nd generation 3D topological insulators: Bi_2Se_3, Bi_2Te_3, and Sb_2Te_3 [17, 18, 19, 20]. The surface states of the Bi_2Se_3 family consist of a single Dirac cone with each electron's spin perpendicular to its momentum.

Though protected by the TR symmetry, the gapless surface state of the Bi_2Se_3 family can be modified by quantum tunneling between the two oppositely spin-textured topological surface states from the top and bottom surfaces. Figure 1-3 shows the tunneling-dependent evolution of spin configuration across the metal-to-insulator transition in Bi_2Se_3 ultrathin films grown by molecular beam epitaxy (MBE) [21]. Below the 6 quintuple layers (QL: unit crystal layer of Bi_2Se_3 constituting five atomic layers of Se-Bi-Se-Bi-Se), the thickness of the film is comparable to the decay length of the surface states into the bulk, resulting in an energy gap.

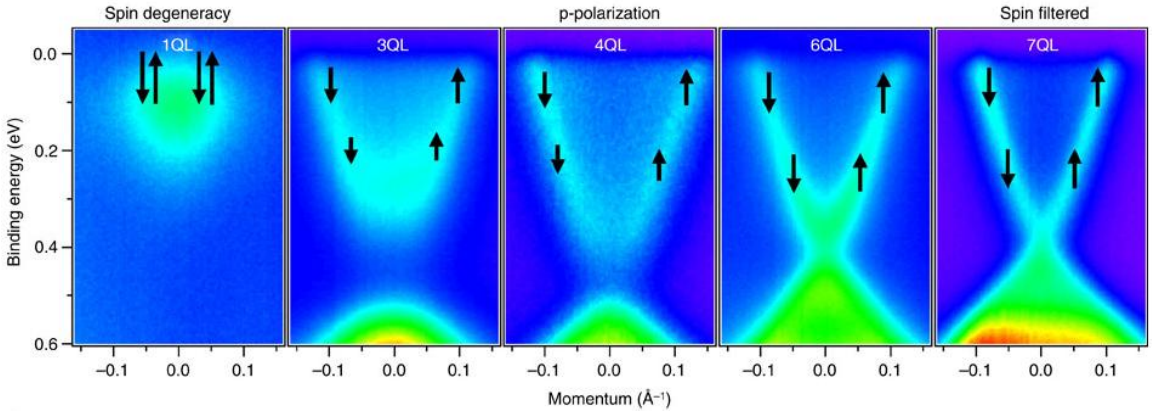

Figure 1-3. ARPES data on Bi_2Se_3 ultrathin films (1 QL, 3 QL, 4 QL, 6 QL and 7 QL). The black arrows depict the spin configuration in the surface state. From reference [21].

Magnetic surface phases modified by broken TR symmetry

The properties of surface states in topological insulators can be modified when the TR symmetry is broken and an energy gap is induced at the Dirac point as a result. One can break the TR symmetry by applying an external magnetic field, doping the topological insulator surface with magnetic atoms, or interfacing a magnetic material [22]. The magnetic surface phases modified by broken TR symmetry have motivated several fundamental and applied phenomena, such as half-integer quantum Hall effect, topological magneto-electric effect [22, 23], induction of a magnetic monopole [24], topological Kerr and Faraday rotation [22], and quantized quantum Hall effect [25, 26]. In the following subsections, I will review some of these emerging quantum phenomena.

TR symmetry breaking in 3D topological insulators

The effective Hamiltonian of the surface state to the leading order in k_x and k_y has the following matrix form [2]:

$$H_{surf}(k_x, k_y) = \epsilon\mathbb{I} + \hbar v_F(\sigma^x k_y - \sigma^y k_x), \tag{1.1}$$

where $\mathbb{I}$ is the 2×2 identity matrix, $\hbar$ is the Plank constant, v_F is the Fermi velocity, and $\sigma^{x,y,z}$ are the Pauli matrices. One can set $\epsilon = 0$ for simplicity, but the effective surface Hamiltonian H_{surf} is still even under TR.

Now I analyze perturbations to the effective surface Hamiltonian by adding momentum-independent perturbation $H_1 = \sum_{a=x,y,z} m_a \sigma^a$. The perturbed Hamiltonian becomes

$$H_{surf}(k_x, k_y) = \epsilon\mathbb{I} + \hbar v_F(\sigma^x k_y - \sigma^y k_x) + \sum_{a=x,y,z} m_a \sigma^a \tag{1.2}$$

with the eigenvalue

$$E_k = \pm\sqrt{(\hbar v_F k_y + m_x)^2 + (\hbar v_F k_x - m_y)^2 + {m_z}^2}. \quad (1.3)$$

Thus, non-zero m_z is the only term to induce an energy gap. The mass term $m_z\sigma^z$ is odd under time reversal. In other words, the mass term $m_z\sigma^z$ breaks the TR symmetry in the topological insulator surface states.

Spin-resolved ARPES measurements on magnetic topological insulator Bi_2Se_3 films doped with Mn demonstrated that an energy gap was opened at the Dirac point with magnetically induced spin reorientation phenomena [27]. Interestingly, the measured electronic states exhibit hedgehog-like spin textures at low energies as a result of the TR symmetry breaking on the surface, as shown in the illustration in Figure 1-4(b).

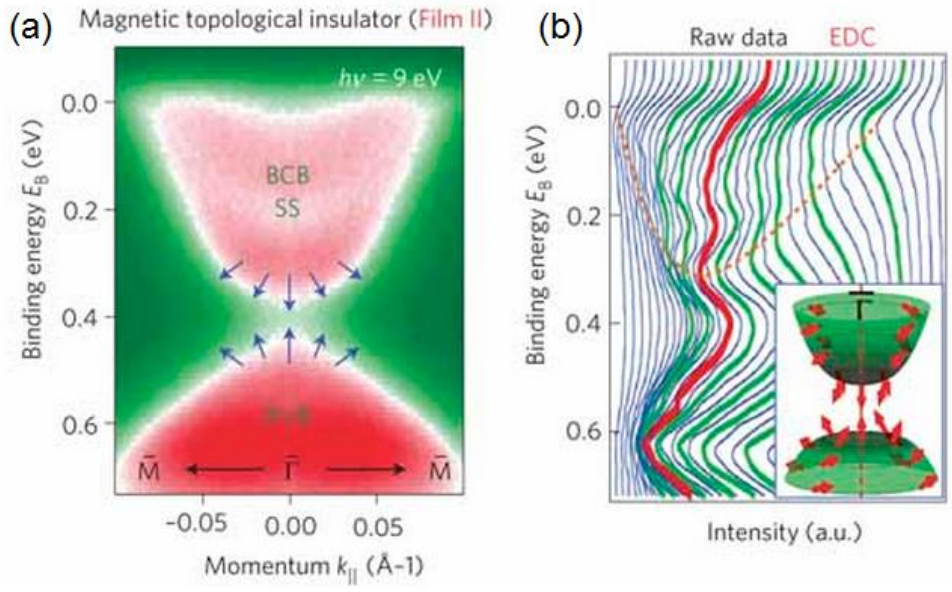

Figure 1-4. (a) Spin-integrated dispersion from a Mn-doped Bi_2Se_3 film with 2.5 % Mn concentration. (b) Energy distribution curves (EDCs) with spin-resolved measurements highlighted in green and red. From reference [27].

Quantum phenomena by broken-TRS

Half-integer quantum Hall effect

Adding a mass term $m_z\sigma^z$ to the effective surface Hamiltonian results in the half-integer quantum Hall effect. The Hall conductance of a generic two-band system can be determined by the Thouless, Kohmoto, Nightingale, and den Nijs (TKNN) formula [7]:

$$\sigma_H = \frac{e^2}{h}\int \frac{d^2k}{2\pi}\Omega_{xy} = n\frac{e^2}{h}. \tag{1.4}$$

The integer *n* is identified as an integral of the Bloch wave functions over the Brillouin zone (BZ). With an assumption of a perturbation periodic in time, a Hamiltonian which is periodic in both time and *k* can be topologically mapped into a torus. A torus is topologically equivalent to a gapped band structure that can be deformed continuously without closing the band gap. The topological invariant is denoted by *n*, the Chern number, which is associated with the Berry phase that appears in the Bloch wave function around a closed loop of a periodic BZ. As introduced in Equation (1.4), the Chern number of the topological insulator surface with broken TR symmetry can be calculated by integrating the Berry curvature Ω_{xy}, which is obtained by Berry vector potential.

$$\mathrm{n} = \frac{1}{2\pi}\int dk_x \int dk_y\, \Omega_{xy} = \frac{1}{2\pi}\int dk_x \int dk_y \frac{m_z}{2({m_z}^2 + k^2)^{3/2}} = \frac{1}{2}\frac{m_z}{|m_z|} \tag{1.5}$$

From the result above, the Hall conductance is given by

$$\sigma_H = \frac{m_z}{|m_z|}\frac{e^2}{2h}\ . \tag{1.6}$$

We can see that the half-integer Hall conductance remains finite even in the limit of $m_z \to 0$, and when m_z value changes across 0, the sign of σ_H jumps to the opposite and $\Delta\sigma_H = \frac{m_z}{|m_z|}\frac{e^2}{h}$.

Topological magneto-electric effect

A magneto-electric effect is defined as induction of a magnetization by an electric field or induction of a charge polarization by a magnetic field. Consider a cylindrical geometry which has a side surface gapped by the broken TR symmetry. The TR symmetry can be broken by introducing magnetic order or putting a ferromagnetic material on the surface of the topological insulator, as shown in Figure 1-5(a). The direction of the magnetization of the ferromagnet is assumed as the direction pointing outwards.

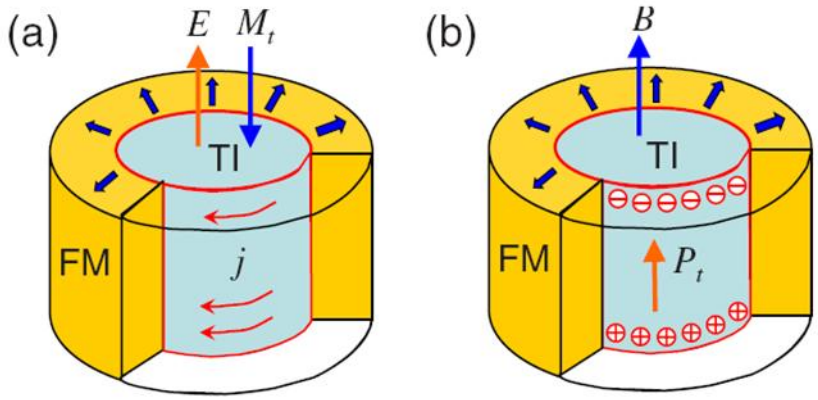

Figure 1-5. Schematics of a cylindrical geometry illustrating (a) a magnetization induced by an electric field due to the surface Hall current and (b) a charge polarization induced by a magnetic field. The magnetization of the FM layer points outwards. From reference [22].

When an electric field is applied parallel to the side surface, a tangential circulating current is induced on the side surface ($j_t = \sigma_H E$). With a unit vector normal to the surface ($\hat{n}$),

$$\boldsymbol{j} = \frac{m}{|m|}\frac{e^2}{2h}\hat{n} \times \mathbf{E} \tag{1.7}$$

with $m/|m|$ determined by the direction of the surface magnetization. The tangential circulating current is identical to the surface-bound current generated by a magnetization $M = \frac{j_t}{c} = \frac{m}{|m|}\frac{e^2}{2hc}$ with the direction opposite to the electric field, such as

$$\boldsymbol{M}_t = -\frac{m}{|m|}\frac{e^2}{2hc}\mathbf{E} \tag{1.8}$$

The total magnetization of the system is $\boldsymbol{M} = \boldsymbol{M}_c + \boldsymbol{M}_t$**,** where $\boldsymbol{M}_c$ is the conventional magnetic response. Thus, the modified constituent equation to the conventional equation $\boldsymbol{H} = \boldsymbol{B} - 4\pi\boldsymbol{M}_c$ is

$$\boldsymbol{H} = \boldsymbol{B} - 4\pi\boldsymbol{M}_c + \frac{m}{|m|}\frac{2e^2}{\hbar c}\mathbf{E} \tag{1.9}$$

Similarly, a topological contribution to the charge polarization can be induced by a magnetic field. In Figure 1-5(b), when the magnetic field $\boldsymbol{B}$ turns on from zero, a circulating electric field is generated and a Hall current is induced in the direction parallel to the magnetic field $\boldsymbol{B}$**.** As a result, electric charges are accumulated at the top and bottom surfaces. The electric polarization is

$$\boldsymbol{P}_t = \frac{m}{|m|}\frac{e^2}{2hc}\mathbf{B}\,. \tag{1.10}$$

Combined with the conventional electric polarization $\boldsymbol{P}_c$, the modified constituent equation to the conventional equation $\boldsymbol{D} = \boldsymbol{E} + 4\pi\boldsymbol{P}_c$ becomes

$$\boldsymbol{D} = \boldsymbol{E} + 4\pi\boldsymbol{P}_c - \frac{m}{|m|}\frac{2e^2}{\hbar c}\mathbf{B}\,. \tag{1.11}$$

By introducing the fine structure constant $\alpha = e^2/\hbar c$, we can rewrite the modified constituent equations of Equations (1.9) and (1.11) as

$$\begin{aligned}\boldsymbol{H} &= \boldsymbol{B} - 4\pi\boldsymbol{M}_c + 2P_3\alpha\mathbf{E}\\ \boldsymbol{D} &= \boldsymbol{E} + 4\pi\boldsymbol{P}_c - 2P_3\alpha\mathbf{B}\end{aligned} \tag{1.12}$$

with the quantum of Hall conductance $P_3 \equiv \frac{m}{2|m|} = \pm\frac{1}{2}$. The resulting equations [Equation (1.12)] show the induced magnetization by an electric field and the induced charge polarization by a magnetic field, which represents the topological magneto-electric effect.

Magnetic monopole

It is well known that the problem of an electric charge on a dielectric half plane can be solved by introducing image electric charge [28]. If the dielectric half plane is a surface of a 3D topological insulator with ferromagnetic ordering, an image magnetic monopole is induced in addition to the image electric charge. Since the surface has an energy gap because of the broken TR symmetry, the surface half-integer quantum Hall effect, as well as the topological magneto-electric effect, needs to be considered.

As shown in Figure 1-6, (i) the upper-half space ($z > 0$) is occupied by a conventional insulator with dielectric constant ε_1 and magnetic permeability μ_1, (ii) while the lower-half space ($z < 0$) is occupied by a topological insulator with dielectric constant ε_2 and magnetic permeability μ_2. A point electric charge q is located at $(0,0,d)$, and this problem can be solved by the method of images. It is assumed that for (i) in the upper-half space, the electric field is given by q/ε_1 at $(0,0,d)$ and an image charge q_2 at $(0,0,-d)$; the magnetic field is given by an image magnetic monopole g_2 at $(0,0,-d)$, while for (ii) in the lower-half space, the electric field is given by q/ε_1 at $(0,0,d)$ and an image charge q_1 at $(0,0,d)$; the magnetic field is given by an image magnetic monopole g_1 at $(0,0,d)$.

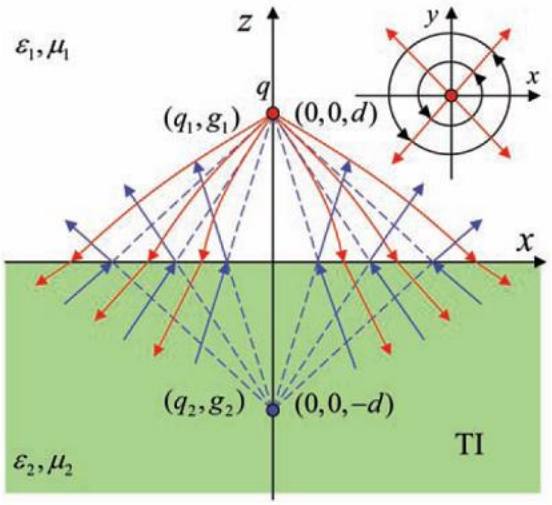

Figure 1-6. Illustration of geometry of a topological insulator interfaced with a conventional insulator. (a) Image electric charge and image magnetic monopole are induced by bringing a point electric charge. Inset shows the circulating surface current (black circles) with the in-plane component of the electric field (red arrows). From reference [24].

For the calculation of image charge and image magnetic monopole, boundary conditions by Maxwell equations at $z = 0$ as well as the electric and magnetic potentials that satisfy Laplace's equation are utilized. One important note is that $\boldsymbol{H_2}$ and $\boldsymbol{D_2}$ in Maxwell equations for topological insulator regime ($z < 0$) are the modified constituent equations [Equation (1.12)] of the topological magneto-electric effect. After some algebra, one would get

$$q_1 = q_2 = \frac{1}{\epsilon_1}\frac{(\epsilon_1 - \epsilon_2)\left(\frac{1}{\mu_1} + \frac{1}{\mu_2}\right) - 4\alpha^2 P_3^2}{(\epsilon_1 + \epsilon_2)\left(\frac{1}{\mu_1} + \frac{1}{\mu_2}\right) + 4\alpha^2 P_3^2}$$

$$g_1 = -g_2 = \frac{4\alpha P_3}{(\epsilon_1 + \epsilon_2)\left(\frac{1}{\mu_1} + \frac{1}{\mu_2}\right) + 4\alpha^2 P_3^2} q\,. \tag{1.13}$$

The results show that an electric charge near a surface of a topological insulator induces both an image electric charge and an image magnetic monopole. This image is a dyon, which is defined as a particle with both electric and magnetic charge. Of course, there are no physical

magnetic charges g_1 and g_2. The source of the induced magnetic field is a surface current. By rewriting Ampere's law $\nabla \times \boldsymbol{H} = \boldsymbol{J}$ with the modified constituent equation [Equation (1.12)], the following describes the topological magneto-electric effect:

$$\nabla \times \boldsymbol{B} = 2\alpha P_3 \delta(z)\hat{n} \times \boldsymbol{E} \tag{1.14}$$

where $\hat{n}$ is the normal vector of the surface and $\delta(z)$ is Dirac delta function. The right-hand side corresponds to a surface current density $\boldsymbol{j} = \sigma^{xy}(\hat{n} \times \boldsymbol{E})$ induced by the in-plane component of the electric field, as shown in the inset to Figure 1-6, and this is the quantized Hall current discussed in the topological magneto-electric effect section. The magnetic field induced by this surface current can be viewed as the magnetic field induced by an image magnetic monopole on the opposite side of the surface.

Quantum anomalous Hall effect

The anomalous Hall effect [29] occurs typically in a ferromagnetic phase with the spin-orbit coupling. In this effect, the Hall voltage (a voltage transverse to the electric current) includes additional contribution depending on the magnetization of the ferromagnetic phase. The quantum anomalous Hall effect is a quantized version of the anomalous Hall effect.

In the quantum spin Hall effect, two edge state channels are propagating in opposite directions, which are determined by the spin orientation of the occupying electrons. When one of the edge state channels is suppressed by spontaneous magnetic moments in the topological insulator system, the quantized anomalous Hall effect can arise. After the theoretical prediction and experimental observation of the quantum spin Hall state in HgTe quantum wells, the quantum anomalous Hall effect was proposed in the magnetically doped $Hg_{1-y}Mn_yTe$ quantum wells [30]. The claim was that the spin polarization of the Mn atoms would cause the quantum anomalous Hall effect on the limit of vanishing spin-orbit coupling and large enough exchange splitting.

However, the quantum anomalous Hall effect in the $Hg_{1-y}Mn_yTe$ system has not been seen since Mn atoms do not order spontaneously in the system.

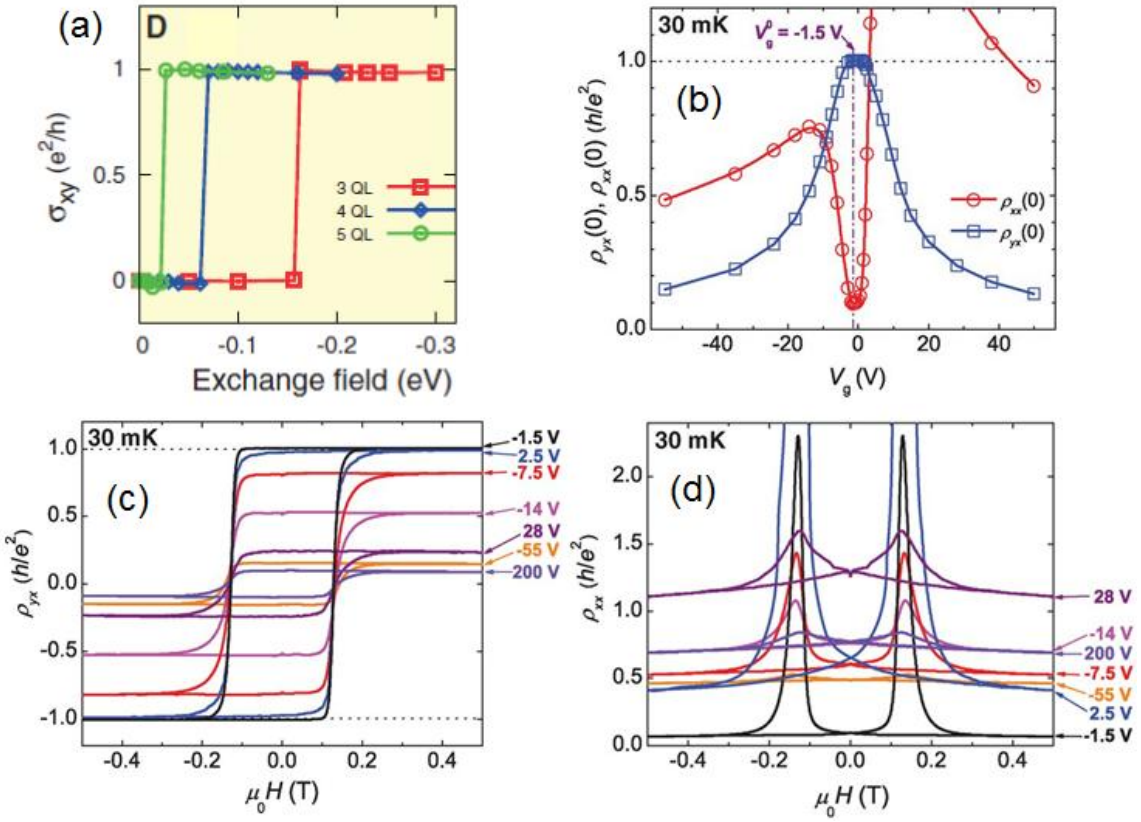

Figure 1-7. Theoretical prediction (a) and experimental demonstration (b-d) of the quantum anomalous Hall effect. (a) The calculated Hall conductance as a function of the ferromagnetic exchange field for three, four, and five QL Bi2Se3 films. After the quantum anomalous Hall transition, the Hall conductance becomes e^2/h. (b) Experimental data of gate-voltage dependence of longitudinal (red) and Hall (blue) resistivities at 30 mK. The Hall resistivity approaches to the predicted quantum value with a gate-voltage of -1.5 V, which was assumed to place the Fermi energy in the opened energy gap. (c,d) The magnetic field dependence of the Hall (c) and longitudinal (d) resistivity with different gate-voltages at 30 mK. From references [25, 26].

Alternatively, the quantum anomalous Hall effect was predicted in ultrathin films of Bi_2Se_3 tetradymite family, where 3D topological insulators cross over to 2D topological insulators, doped with proper transition metals (Cr or Fe) [25]. These systems satisfy the important criteria

for realizing the quantum anomalous Hall state: 1) a ferromagnetic 2D insulator with broken TR symmetry; and 2) a band inversion transition due to the strong spin-orbit coupling. Recently, the prediction was experimentally verified in ultrathin films of magnetic topological insulator Cr-doped $(Bi,Sb)_2Te_3$ when the gate-tuned Fermi level is located in the magnetic energy gap [26]. As the theory predicted, the Hall resistance approaches the quantized value h/e^2 at zero magnetic field while the longitudinal resistance almost vanishes under a strong magnetic field [Figures 1-7(b)-(d)].

Potential spintronics applications

Spintronics is a field of electronics by control and manipulation of electron spin degree of freedom in solid-state systems [31]. The topological quantum phenomena that are associated with the broken TR symmetry in the topological insulator surface states, as discussed in the previous sections, suggest new possible routes towards potential spintronics applications by manipulating spins in topological insulator systems with a presence of exchange coupling.

Generally, studies of spintronics involve the generation of carrier spin polarization, spin dynamics, and spin-polarized transport. In the spintronics point of view, topological insulators, even without the use of quantum phenomena by the broken TR symmetry, are expected to be spin generators due to the spin-polarized Dirac surface state induced by the strong spin-orbit interaction. The potential spintronics applications using a topological insulator as a spin generator will be discussed in the following subsections.

Topological insulator as a spin generator

Apart from the potential applications of the topological quantum phenomena by broken TR symmetry, the inherent spin-polarized surface state of a 3D topological insulator is expected to play a potential role in spintronics as a generator of carrier spin polarization. In the surface state, an electron has its spin helically locked with its momentum. Due to this spin-momentum locking, a topological insulator can generate spin polarization merely by flowing a current.

Electrical detection of the spin-polarized current on a topological insulator surface is a great challenge toward spintronics device applications. Some theoretical proposals suggested the resulting changes in magneto-resistance across a topological insulator channel involving ferromagnetic metal contacts for injection or detection of the spin-polarized current [32, 33]. Suppose a topological insulator channel with a ferromagnetic electrode (FM) on the left and a non-magnetic electrode (NM) on the right separated by a distance L from each other, as illustrated in Figure 1-8(a). A spin-polarized current (I) is injected from the FM contact into the topological insulator channel, and the voltage drop between the electrodes is calculated as [32]:

$$V = \frac{2\pi IL}{e^2 k_F l} + \frac{4\pi I\eta}{e^2 k_F} \tag{1.15}$$

with mean free path *l* and the degree of spin polarization parameterized by η. The first term of Equation (1.15) represents the usual ohmic behavior while the second term constitutes a new magneto-resistance effect by the topological insulator surface state. The second term depends on the degree and direction of the polarization of the FM electrode (η). If the chemical potential of the topological insulator channel could be tuned by applying gate-voltage, the proposed device would possibly function as a transistor.

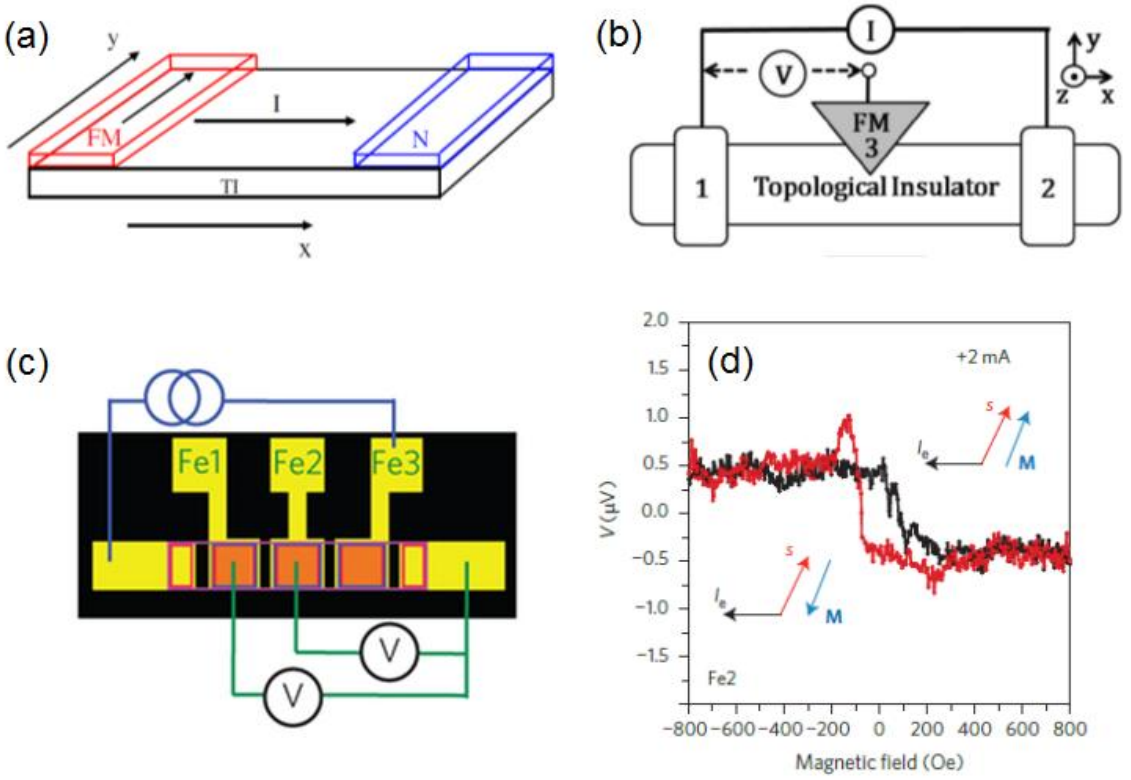

Figure 1-8. (a) A schematic of a device to detect the spin polarization in a topological insulator. An FM electrode can inject spin-polarized current into the topological insulator channel. The resulting voltage drop across the channel contains a contribution related to the cross product of the FM polarization and current. (b) In the potentiometric setup, an FM electrode is used as a voltage probe to detect voltage change proportional to the dot product of spin-polarized current and the magnetic polarization. (c) A measurement setup on a schematic of a device geometry using Fe/Al_2O_3 contacts on a Bi_2Se_3 channel. (d) Experimental data when the magnetization of Fe layer is parallel or anti-parallel to the direction of the inherent spin polarization with a DC current of 2 mA at 8 K. From references [32, 33, 34].

Another proposal was made on a setup of a three-terminal potentiometric with an FM electrode in the middle of a 3D topological insulator channel as a voltage probe [33], as shown in Figure 1-8(b). The detected voltage is proportional to the projection of the spin polarization onto the detector FM magnetization. In other words, the voltage change when reversing the FM spin-polarization is directly related to the current-induced spin polarization of the topological insulator channel. The calculated voltage change is given by

$$\left[V\left(\vec{M}\right) - V\left(-\vec{M}\right)\right]/I = R_B(\vec{p} \cdot \vec{m}), \quad (1.16)$$

where R_B, $\vec{p}$, and $\vec{m}$ represent ballistic resistance, degree of the spin polarization per unit current in the topological insulator channel, and effective magnetic polarization, respectively.

Recently, experiments on electrical detection of the current-induced spin polarization were demonstrated with the three-terminal potentiometric setup, as proposed in the reference [33], using a magnetic tunnel junction as a voltage detector [34]. Changes in the detected voltage were observed with the magnetization of an FM contact flipping from parallel to anti-parallel directions, and vice versa, to the direction of the current-induced spin polarization, as shown in Figure 1-8(d). The Bi_2Se_3 channels in the experiments have a considerable contribution of unpolarized bulk conduction parallel to the spin-polarized conduction through surface states, suggesting that a larger spin signal is expected in a topological insulator channel with a suppressed bulk conduction.

Spin transfer torque by topological insulator

A spin-polarized current can provide a torque on a magnetic layer, resulting in the magnetization precession or the magnetization switching [35]. Recent studies of bilayers of ferromagnet/heavy metal with a strong spin-orbit coupling have demonstrated spin transfer torques exerted on a magnetic layer [36, 37, 38, 39, 40]. As materials for more efficient spin-orbit-induced torques, topological insulators are suggested [5, 32, 41] due to the spin-polarized current by the inherent helical spin texture of the topological insulator surface state. The spin-polarized current couples to the adjacent magnetic layer, and a spin-transfer torque is applied on the magnetic layer by a flow of spin angular momentum.

Recently, experiments on spin transfer torques generated by topological insulator thin films of Bi_2Se_3 were demonstrated at room temperature by Mellnik and co-workers [42]. We

showed that an electrical current flowing in-plane in a Bi_2Se_3 thin film can indeed exert a strong spin-transfer torque to an adjacent ferromagnetic permalloy (Py) thin film. The Bi_2Se_3 thin films with Se capping layer were synthesized by molecular beam epitaxy in our lab, then the Py layer was deposited by sputtering after decapping the Se layer *in situ*. The strength of current-induced torque was determined by a spin-torque ferromagnetic resonance (ST-FMR) technique [36]. With a microwave current with a fixed frequency, an in-plane magnetic field is applied to precess the Py magnetization by the oscillating current-induced torque [Figure 1-9(b)]. The resulting voltage V_{mix} from mixing between the applied microwave current and the oscillating resistance gives the resonance lineshape [Figure 1-9(c)]. The symmetric and antisymmetric components of the resonance lineshape determine the two vector components of the current induced torque, $\tau_{\parallel}$ (in-plane) and $\tau_{\perp}$ (perpendicular).

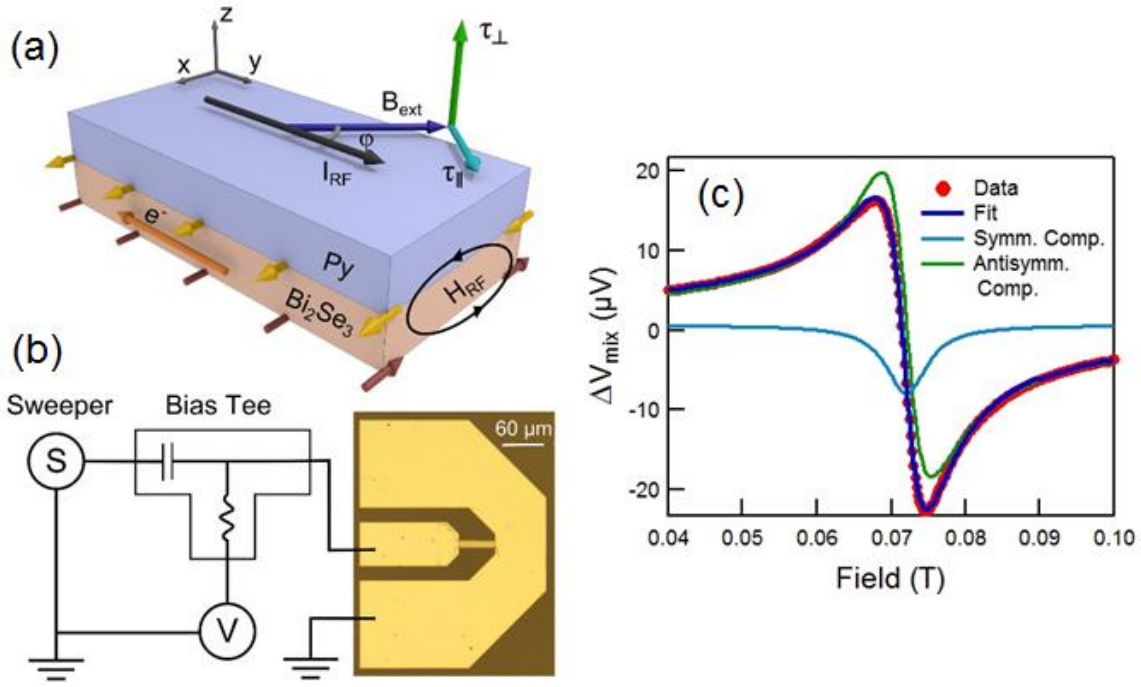

Figure 1-9. Schematics diagram of (a) the Py/Bi_2Se_3 bilayer and (b) the measurement setup. In the schematic (a), the yellow and brown arrows represent spin polarization in the topological insulator. (b) Circuit for the ST-FMR measurement connected to the sample contact geometry. (c) ST-FMR resonance data in an 8 nm Bi_2Se_3/16 nm Py bilayer at room temperature with fits of symmetric and antisymmetric components of the resonance. From reference [42].

Surprisingly, the "spin torque ratio" of Bi_2Se_3 at room temperature is larger than those of any previously measured spin-current source material. The "spin torque ratio" is the figure of merit which describes the strength of the in-plane component of torque per unit of applied charge current density J in the spin-current source material.

$$\theta_{||} \equiv \frac{2e}{\hbar}\frac{J_{s,||}}{J} = \frac{2e}{\hbar}\frac{\sigma_{s,||}}{\sigma} \tag{1.17}$$

where $J_{s,||}$ and $\sigma_{s,||}$ are the in-plane components of the spin current density and spin current conductivity, respectively, while J and σ represent the charge current density and the charge current conductivity. Our results suggest that topological insulators can be used as room-temperature sources of spin torque for very efficient electrical manipulation for memory and logic applications.

Outline

This dissertation research is focused on topological insulator systems hybridized with magnetism. Two different approaches of breaking TR symmetry in the surface state are experimentally studied: 1) magnetic doping of topological insulators and 2) interfacing a magnetic layer to a topological insulator. Also, magnetic tunnel junctions are utilized to evidence the inherent spin-polarized texture of the topological insulator surface state. The importance of the studies of topological insulator systems with magnetism lies in understanding the underlying physics in topological insulators as well as in exploring the potential spintronics applications.

Experimental methods of material synthesis, characterization, and magneto-transport measurements will be reviewed in Chapter 2. Chapter 3 discusses the crystal structures and ferromagnetic properties of the magnetic topological insulator bismuth telluride doped with Mn. Chapter 4 describes detailed studies of hybrid topological insulator/ferromagnet heterostructures

using the conventional dilute magnetic semiconductor (Ga,Mn)As as a highly insulating ferromagnetic material. Magneto-transport evidences of the modified topological insulator surface state by the adjacent magnetic layer are discussed. Finally, in Chapter 5 I describe the experimental demonstration of the electrical detection of the spin-polarized surface state due to the spin-momentum locking in topological insulator films with the chemical potential in the bulk band gap.

Chapter 2

Experimental Methods

For the experiments described in this dissertation, we have employed various experimental techniques of thin film synthesis, material characterization, device fabrication, and electrical transport measurement. The general aim is to fabricate high-quality topological insulator (TI) nanostructures and mesoscopic devices to understand the fundamental physics of the TI surface states by various characterization methods. This chapter focuses on detailed descriptions of experimental techniques and procedures routinely used for the research described in this dissertation.

Molecular beam epitaxy (MBE)

It is crucial for all the entire research projects to grow single crystalline TI thin films of the Bi2Se3 family with minimum defects, such as Se vacancies. We have carried out the molecular beam epitaxy (MBE) growth method for atomic layer-by-layer construction of single crystalline epitaxial layers on top of crystalline "epitaxy ready" substrates.

System overview

Figure 2-1 illustrates the MBE growth process. In a chamber under ultra-high vacuum (UHV) of low 10^{-10} Torr, a molecular beam of evaporated atoms is produced from high-purity elemental source in a heated conventional Knudsen effusion cell. Molecular beams of elements,

such as Bi and Se, for example, reach a heated, crystalline substrate without interacting with each other due to the long mean free paths and condense to form a single-crystalline overlayer, such as Bi_2Se_3. The UHV is maintained by vacuum pumps, such as a cryopump (or a "cryogenic pump") and an ion pump. In a cryopump, gases and vapors are trapped by condensation on a cold surface of a metallic plate cooled by compressed helium, while in an ion pump, gases and molecules are ionized by a strong electrical potential, and the resulting ions are accelerated to strike and eject a cathode material, so that the gases and molecules are trapped by the ejected cathode material. During a growth procedure, the system is cooled down by liquid nitrogen to minimize residual gases for even lower pressure. The MBE system in our lab consists of two commercially available EPI 620 and EPI 930 systems, for II-VI and III-V growths respectively, connected by a buffer chamber, as shown in Figure 2-2(b). A cryopump is used in the II-VI chamber [Figure 2-2(a)], and the III-V chamber is pumped by an ion pump.

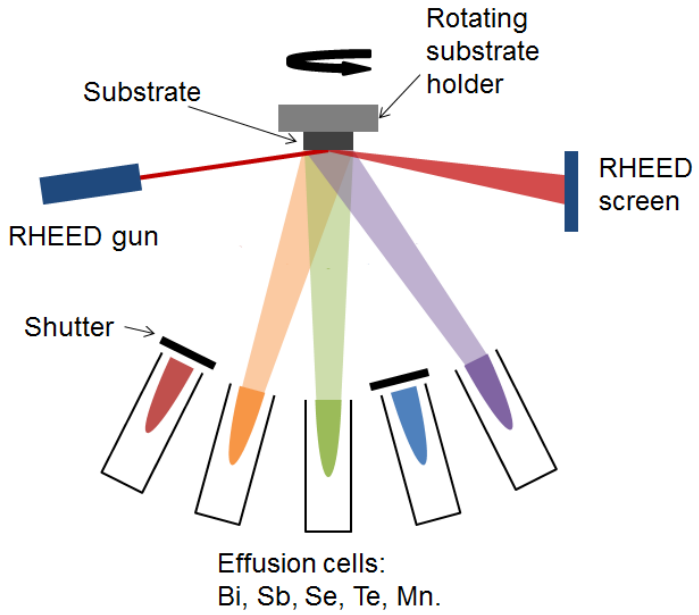

Figure 2-1. A schematic of an MBE growth operation. Molecular beams from effusion cells with open shutters reach a substrate to form a single-crystalline overlayer while the growth of the crystal is monitored by RHEED. Electrons from a RHEED gun approach the substrate at a small angle and are diffracted by the crystal surface to form diffraction patterns on a detector phosphor screen.

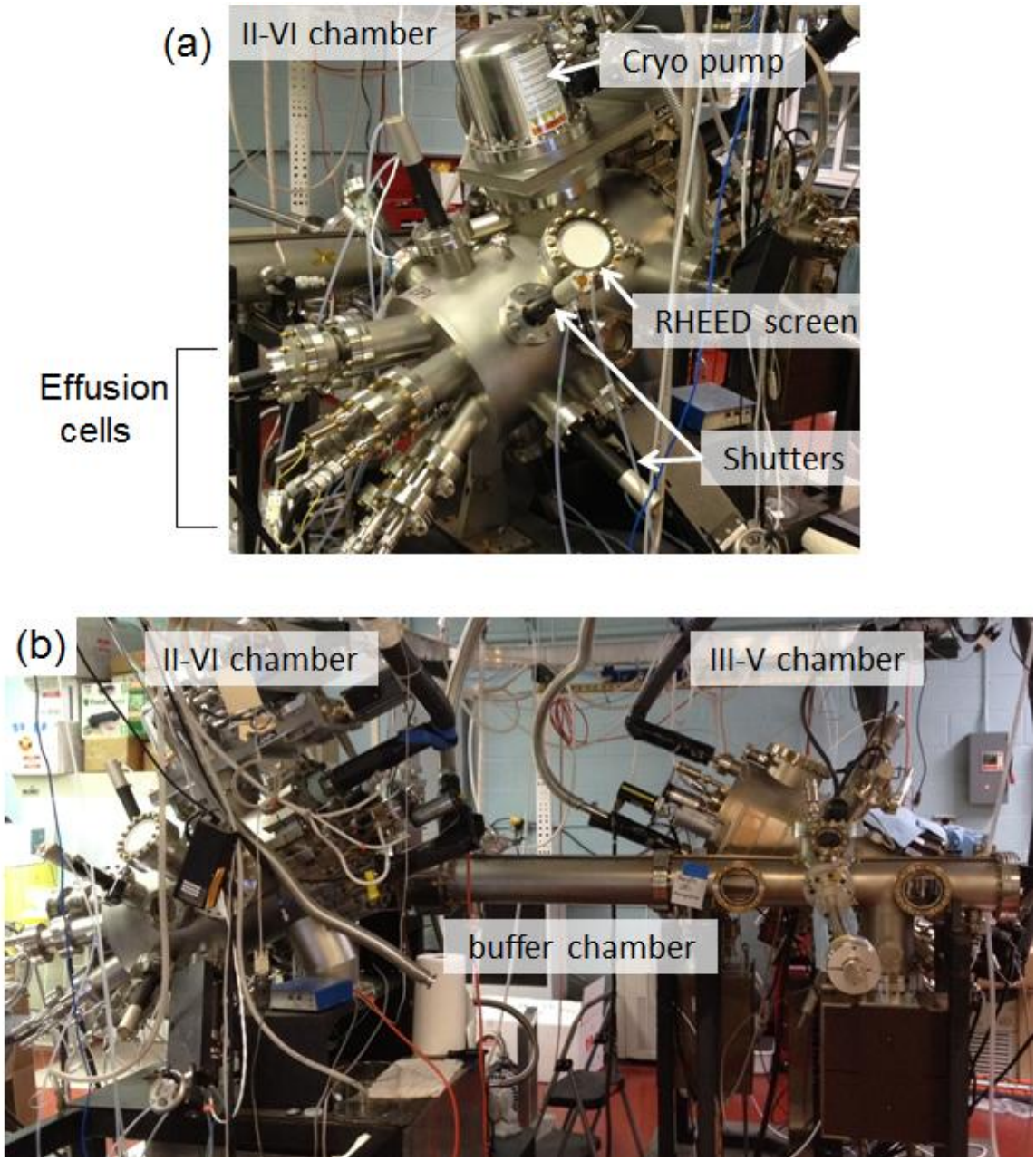

Figure 2-2. Photos of the MBE system. (a) The II-VI chamber (EPI620) is equipped with a cryopump, a RHEED gun/screen, effusion cells of elemental sources of Bi, Sb, Se, Te, and Mn, and an e-beam evaporator cell. (b) The II-VI chamber and III-V chamber (EPI930) connected by a buffer chamber.

TI thin films are grown in the II-VI chamber, which contains conventional Knudsen effusion cells of high-purity elemental sources of Bi, Sb, Se, Te, and Mn, and a 4-pocket e-beam evaporator cell, which provides additional options of doping or thin-film deposition. Currently, in the e-beam evaporator cell we have metallic sources, such as Cr, Fe, Co, and Nb. For the dissertation research, I have been growing TI thin films of Bi_2Se_3, Bi_2Te_3, Mn-doped Bi_2Te_3, $(Bi,Sb)_2Te_3$, and $(Bi,Sb)_2(Te,Se)_3$ on various substrates, such as InP(111)A, GaAs(111)A, GaAs(111)B, GaAs(001), (Ga,Mn)As, Al_2O_3(0001), and $SrTiO_3$(111).

The III-V chamber is utilized for III-V-material-based semiconductor synthesis of thin films or nanowires. The III-V system is equipped with an ion pump, a reflection high-energy electron diffraction (RHEED) gun/screen, a band-edge thermometry system for temperature monitoring, and Knudsen effusion cells of high-purity elemental sources of Ga, As, Mn, Al, Si, Sb, and In. Since the III-V chamber is connected to the II-VI chamber by a UHV buffer chamber, it is possible to grow a heterostructure consisting of II-VI material layers and III-V material layers with clean interfaces. One example is a heterostructure of a $(Bi,Sb)_2(Te,Se)_3$ film on a (Ga,Mn)As layer that is studied in Chapter 4. The (Ga,Mn)As layer is grown on an InP(111)A substrate in the III-V chamber, and the substrate is transferred to the II-VI chamber without breaking the vacuum. Then a TI $(Bi,Sb)_2(Te,Se)_3$ film is grown in the II-VI chamber. In addition, I have used the III-V chamber to desorb native oxide on InP(111)A substrates under As flux for a clean, smooth surface.

During the growth procedure, a surface of a film is monitored by RHEED. A beam of electrons generated by an electron gun is diffracted on a sample surface, and some of the diffracted electrons form diffraction patterns on a phosphor RHEED screen (Figure 2-1). RHEED will be discussed in detail in the thin-film characterization section.

Growth of Bi_2Se_3 thin films

Nanostructures of TI thin films are used for all the dissertation projects. Therefore, it is important to discuss the specific procedures of the TI film growth. I'll describe the step-by-step procedure of the growth of Bi_2Se_3 thin film on an InP(111)A substrate as an example of a TI growth utilizing two MBE systems. The native oxide on the InP(111)A substrate is desorbed under As flux in the III-V chamber, and then the substrate is transferred without breaking the vacuum to another UHV chamber for Bi2Se3 growth.

<Loading>

1. Mount an InP(111)A substrate on a clean molybdenum block by indium bonding on a hot plate at ~210°C.
2. Vent the buffer chamber with N_2 gas.
3. Load the block into the buffer chamber and pump down.
4. Load the block into the III-V chamber.

<Desorbing InP(111)A substrate>

5. Heat up the substrate to a thermocouple temperature of 640°C.
6. Open the shutter of the As cell when the substrate temperature is 500°C.
7. Desorb for ~10 minutes to remove oxide under As-rich environment. Use RHEED to monitor the surface of the substrate as the oxide is removed.
8. Cool the substrate to room temperature.
9. Leave As cell open till it reaches 400°C.
10. Unload the block from the III-V chamber into the buffer chamber.
11. Load the block into the II-VI chamber.

<Growth of a Bi_2Se_3 film>

12. Heat up the substrate to a growth temperature (300-350°C).

13. Open the shutter of the Se cell for 30 seconds.
14. Open the shutter of the Bi cell for a growth of Bi_2Se_3 film. Use RHEED to monitor the morphology of the Bi_2Se_3 surface during the growth.
15. Close the shutter of the Bi cell.
16. Cool the substrate to room temperature. Leave the shutter of the Se cell open until the temperature reaches ~180°C to minimize defects such as Se vacancies.

    <Unloading>
17. Unload the block from the II-VI chamber into the buffer chamber.
18. Vent the buffer chamber with N_2 gas.
19. Unload the block from the buffer chamber.
20. Remove the substrate from the molybdenum block on a hot plate at ~210°C.

Thin film characterization

Reflection high-energy electron diffraction (RHEED)

RHEED is a surface-sensitive technique used to qualitatively characterize a surface of crystalline materials. RHEED is commonly used for *in-situ* monitoring of surface structure during film growth as well as for determining the growth rate by RHEED intensity oscillations.

A beam of monoenergetic electrons (12 keV), generated by an electron gun, hits a film surface at a glancing angle of a few degrees and is diffracted, reflected, or absorbed. The electrons diffracted by the periodic potential of the crystal surface form characteristic patterns on a phosphor screen, while the reflected electrons form a specular beam spot. Due to the small incidence angle of the electrons to the film surface, the penetration depth is very short, so that the diffraction patterns are mostly sensitive to the crystal structure of the top monolayer. “Streaky”

RHEED patterns indicate a smooth 2D surface while "spotty" patterns indicate a 3D growth, such as the forming of surface islands or faceting. Figure 2-3 shows streaky patterns from a desorbed InP(111)A substrate and a Bi_2Se_3 film grown on the substrate.

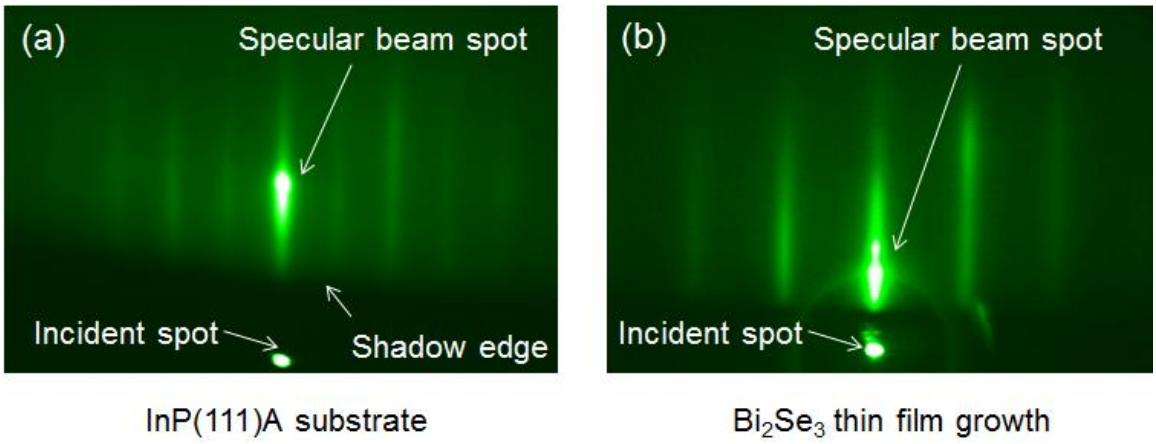

Figure 2-3. Streaky RHEED patterns (a) from a InP(111)A substrate after desorption under As flux and (b) from a Bi_2Se_3 film grown on the InP(111)A substrate.

In the MBE growth process, one atomic layer is grown at a time. The layer-by-layer growth can be monitored by the oscillation of RHEED intensity, especially the intensity of the specular reflection, which makes it possible to directly measure the growth rate. Figure 2-4(a) illustrates the mechanism of how the RHEED intensity oscillates as a top monolayer grows. A flat, complete layer results in a maximum intensity of the specular beam spot. As a layer starts to grow, small islands nucleate, and more electrons are randomly scattered because of the irregular periodic potential of the crystal surface, resulting in a dimmer intensity. After the minimum intensity with the surface coverage of 0.5, the layer becomes smoother, and the intensity increases to reach another maximum with a complete layer. The frequency of the RHEED oscillation corresponds to the growth rate of a monolayer. Figure 2-4(b) shows a RHEED intensity oscillation of a specular beam spot from a Bi_2Te_3 growth on a InP(111)A substrate. The resulting

period is 62.8 seconds, and the frequency is 0.955 oscillations per minute. One unit crystal layer of Bi_2Te_3 is a quintuple layer that is of ~1 nm. Therefore, the growth rate of the Bi_2Te_3 film is 0.955 QL/min (or ~0.955 nm/min).

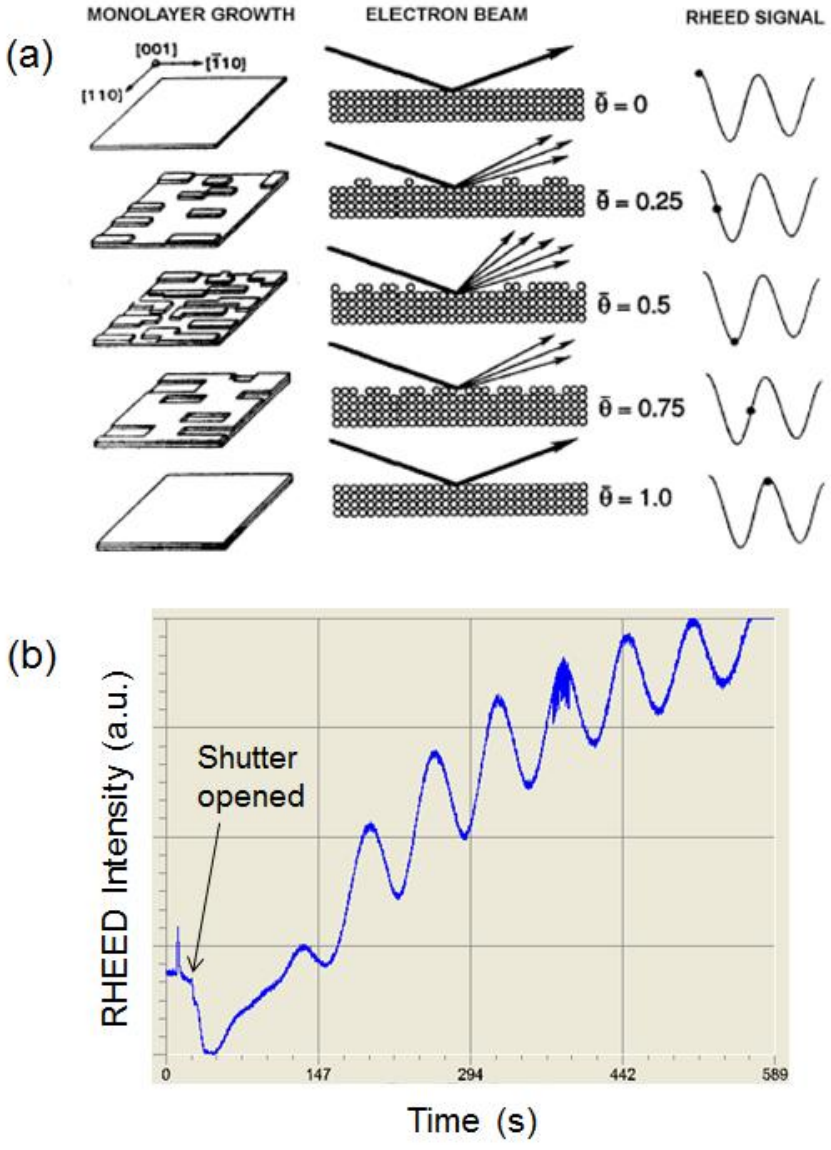

Figure 2-4. (a) An illustration of a monolayer growth in the relation to RHEED specular beam spot oscillation. From reference [43]. (b) RHEED intensity oscillation on a Bi2Te3 surface at an electron energy of 12 keV.

Electrical transport measurement

Hall effect measurement

One of the aims of MBE growth of TI films is the synthesis of films with the chemical potential in the surface state. The position of the chemical potential of TI films can be estimated by carrier densities. The most common way of determining carrier density is the Hall effect measurement. We have routinely carried out Hall effect measurements for the electrical properties, such as carrier density and mobility, of the MBE-grown TI films.

In a conductor, as a magnetic field is applied perpendicular to the flow of current, electrons or holes experience the Lorentz force and move perpendicular to the direction of the current and the magnetic field [44]. For electrons, the measured Hall voltage is given by

$$V_H = -\frac{IB}{nte} \tag{2.1}$$

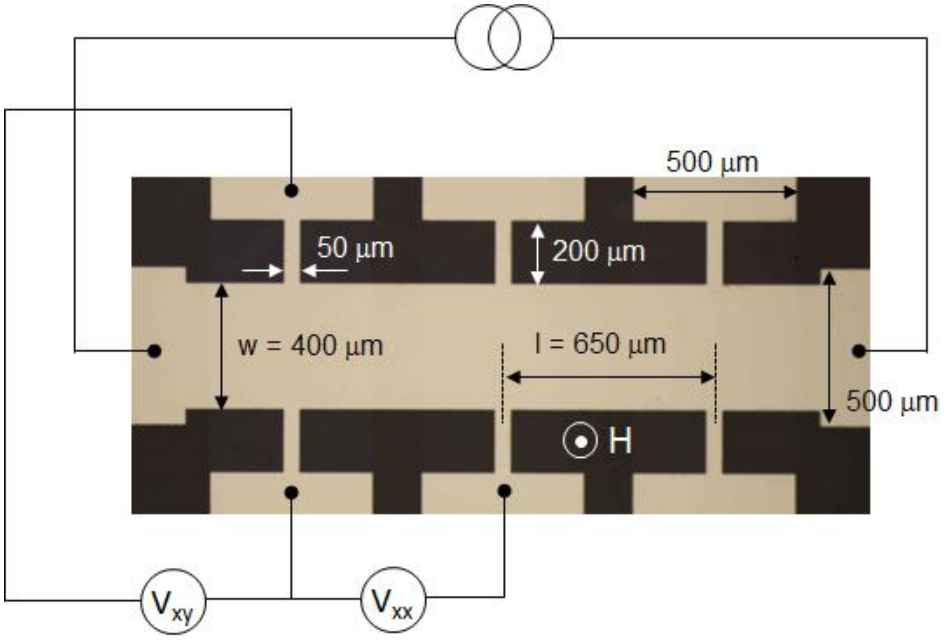

Figure 2-5. A schematic of the Hall measurement setup on a typical Hall-bar geometry. A current flows between the left and right contacts, and two perpendicular contact pads are used to measure the Hall voltage.

where *I, B, n, t* and *e* are the charge current, the magnetic field, carrier density, thickness of the conductor, and the elementary charge, respectively. The Hall voltage for holes has the opposite sign due to the opposite direction of the Lorentz force.

For the Hall effect measurements, we have used Hall bars that are fabricated by a standard photolithography as described in detail in Appendix A. A current flows across the channel while a voltage is measured between the two contacts perpendicular to the current. To determine the carrier density, a Hall voltage needs to be measured as a function of a magnetic field. The slope V_H/B is inversely proportional to the carrier density.

Typically, a longitudinal voltage between two contacts parallel to the direction of a current is measured together with the Hall voltage. The longitudinal voltage measurement provides electrical properties of resistivity and mobility.

Low-temperature magneto-transport measurement

Low-temperature magneto-transport measurement is one of the most important techniques for this dissertation research since we are interested in studies that require cryogenic temperatures. In Chapter 3, we investigate ferromagnetism in magnetic TI samples whose T_C is below 17 K. Quantum corrections of weak antilocalization in magnetoconductance are typically observed below 20 K (in Chapter 4). The background noise signal needs to be suppressed by lowering temperature for the electrical detection of small spin signals (in Chapter 5). For those measurements, a cryogenic system with a magnet is necessary. We have used two cryostat systems in our lab: an Oxford Heliox Helium-3 cryostat and an Oxford Triston Helium-3 vector magnet cryostat.

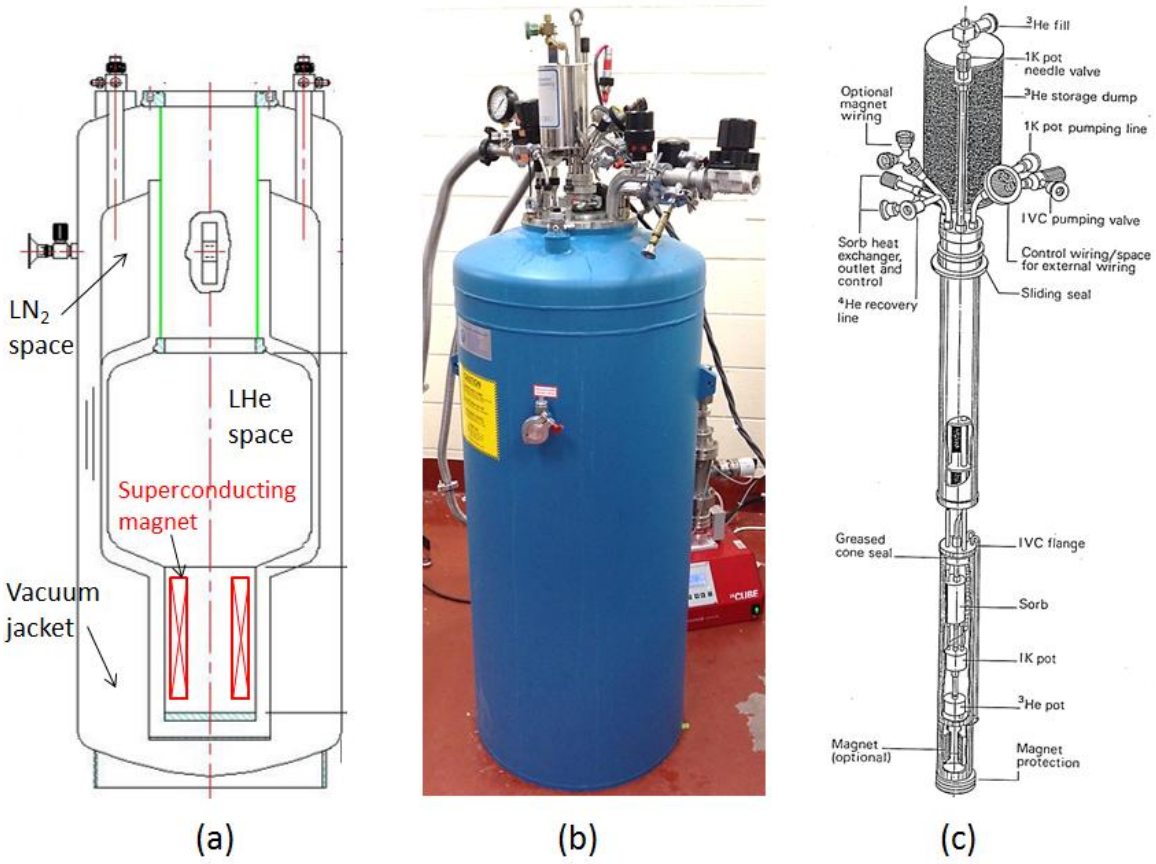

Figure 2-6. (a) An illustration of a liquid Nitrogen-shielded liquid Helium dewar. (b) A picture of an Oxford Heliox Helium-3 cryostat inserted into a liquid Helium dewar. (c) A schematic of an Oxford Heliox Helium-3 cryostat. From reference [45, 46].

Cryostat systems

A pumped Helium-3 cryostat system can be cooled down to a base temperature of ~300 mK. Here we discuss the operation principle of the Oxford Heliox Helium-3 cryostat. Figure 2-6(c) shows a schematic illustration of the cryostat system that consists of a 1 K pot system, a Helium-3 sorption pump system, a sample stage, and the inner vacuum can (IVC). A sample is mounted, and the IVC is sealed and pumped down to 10^{-10} Torr by a turbo pump. The Heliox cryostat insert is first cooled down to 77 K by putting the insert into liquid Nitrogen, and then the

insert is transferred to a liquid-Nitrogen-shielded liquid Helium dewar [Figure 2-6(a)] and cooled down to liquid Helium temperature (4.2 K). The sample can be cooled down to ~1.5 K by introducing and pumping liquid Helium into the 1 K pot. Further cooling down to the base temperature is achieved by a sorption-pumped Helium-3 system. Figure 2-7 illustrates the operation principle. The sorption pump (sorb) is warmed up to 45 K to release absorbed Helium-3 gas. Helium-3 condenses and is collected in the Helium-3 pot. The sorb heater is turned off and cooled when the Helium-3 pot is nearly full of liquid Helium-3. The cooling of the sorb begins to reduce the vapor pressure of Helium-3, and the sample temperature drops to the base temperature. Below the 1 K pot temperature, the sample temperature can be controlled by heating the sorb.

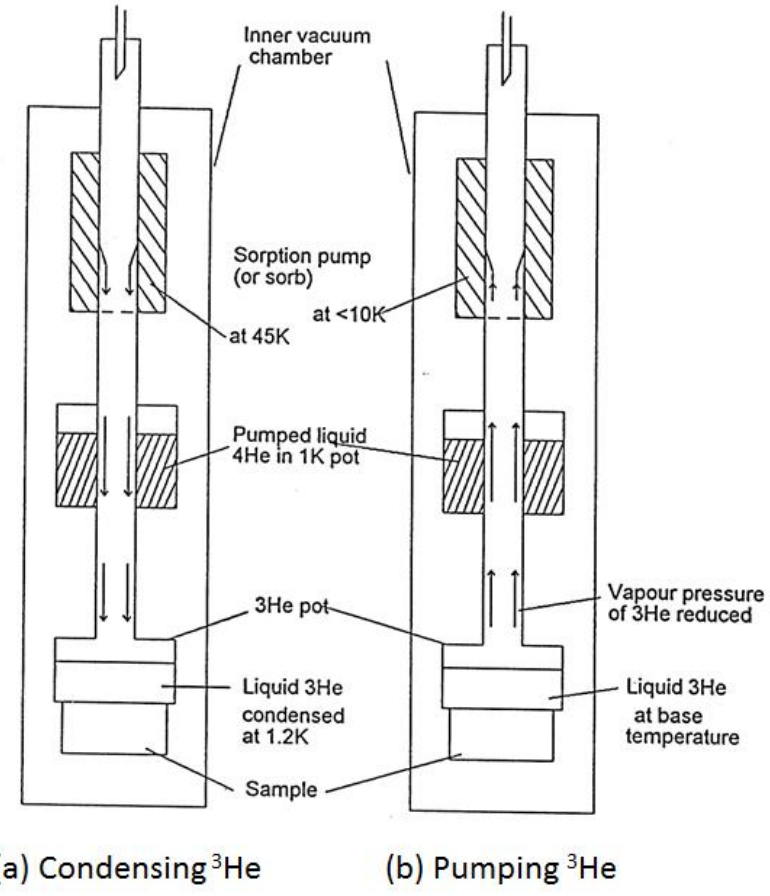

Figure 2-7. An illustration of the operation procedure of (a) condensing and (b) pumping Helium-3. From reference [46].

A similar operation principle of a Helium-3 sorption pump is utilized in the Oxford Triton Helium-3 vector magnet cryostat system. This cryogen-free system does not require liquid Helium, but it cools down using a compressor with a closed-cycle Helium-4 cooling system. The system consists of four separate temperature stages of the pulse tube refrigerator (PTR): the first stage (PT1), the PTR second stage (PT2), the intermediate stage (interstage), and the He3 stage (Figure 2-8). Each stage operates at 50 K, 3 K, 1.5 K, and 0.3 K, respectively. The operating temperature range of the system is between 300 mK and 30 K. At the base temperature of 300 mK, the system holds the temperature for ~40 hours.

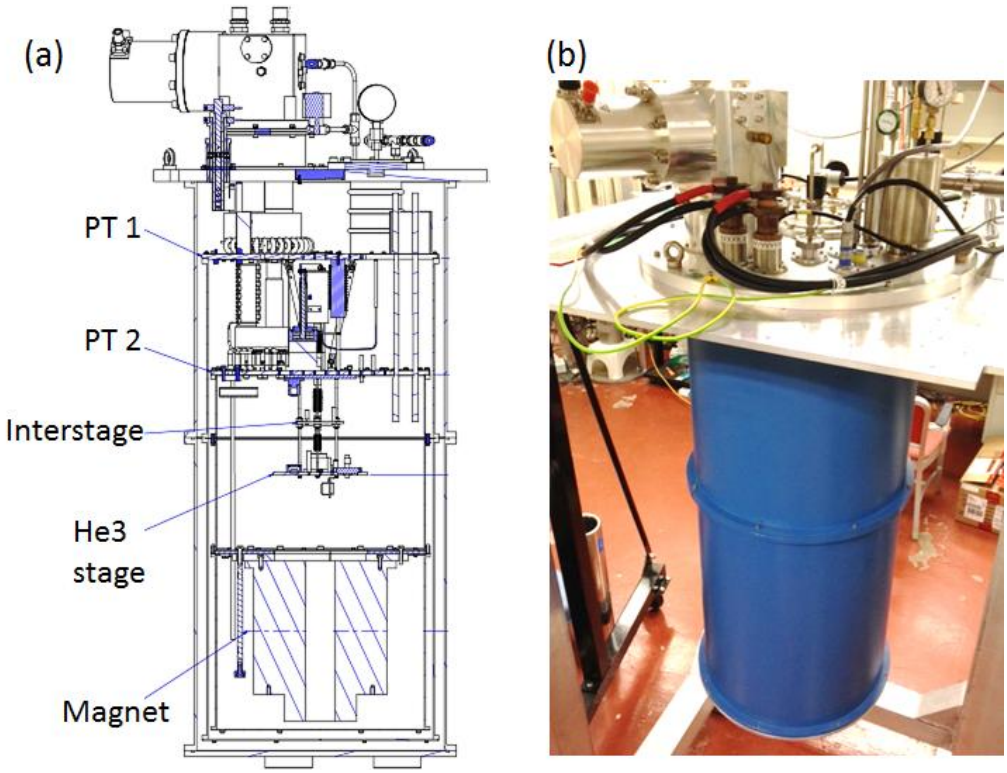

Figure 2-8. A schematic illustration (a) and a picture of the Oxford Triston Helium-3 vector magnet cryostat system. From reference [47].

Superconducting magnets

Both the Heliox cryostat system and the Triton Helium-3 cryostat system utilize superconducting magnets. For the Heliox system, a superconducting magnet capable of generating a magnetic field up to 8 T is immersed in liquid Helium. The field direction is limited to one direction pointing upward. On the other hand, the superconducting magnet in the Triton Helium-3 cryostat system is a vector magnet composed of three superconducting electromagnet coil pairs. The vector magnet system can apply a magnetic field up to 1 T in any 3D direction and 2 T in a direction pointing upward (z direction).

Chapter 3

Ferromagnetism in topological insulator bismuth telluride doped with Mn

In Chapter 1, we discussed that topological insulator (TI) surface states can be modified by introducing magnetism, resulting in new topological quantum phenomena by the broken TR symmetry. In this chapter, from the motivation of breaking TR symmetry in the surface state, magnetic doping of three-dimensional (3D) TI will be discussed and experimentally demonstrated. For this study, we have chosen Mn-doping, which was used in the earlier study of Mn-doped Bi_2Se_3 in our lab [48], and bismuth telluride as a 3D TI. Unlike Mn-doped Bi_2Se_3 thin films, Mn-doped Bi_2Te_3 thin films do not show nanoscale segregation of magnetic atoms and do reveal strong ferromagnetism with perpendicular anisotropy. A detailed study of the structural, magnetic, and magnetotransport properties of the single-crystal, n-type bismuth telluride doped with Mn is described in this chapter. Ferromagnetism was observed with a Curie temperature in the range 13.8–17 K in films with ~2−10% Mn concentration. The Curie temperature does not show any obvious dependence on carrier density in the n-type, Mn-doped bismuth telluride films, suggesting that the observed ferromagnetism is not mediated by charge carriers in the conduction band or in an impurity band. A large part of the text in this chapter is borrowed from a paper recently published in Physical Review B [49].

Introduction

3D TIs have attracted much interest due to the presence of spin-momentum-locked surface states that are protected by time reversal (TR) symmetry [1, 2, 3, 10, 11]. Magnetic

doping of a TI breaks TR symmetry and is predicted to open a gap at the Dirac point [22, 50, 51, 52], resulting in exotic quantum phenomena such as the topological magnetoelectric effect [22], the induction of a magnetic monopole [24], and the quantized anomalous Hall effect [25, 26]. Recent experimental progress towards incorporating ferromagnetism with 3D TIs has indeed led to the realization of such effects, including the observation of a hedgehog spin texture [27], gate-tunable ferromagnetism [53], and a quantized anomalous Hall effect [26]. This interplay between magnetism and topologically protected states is of potential interest for applications in quantum computing and spintronics [5].

Given this context, there is a strong motivation for exploring the magnetic behavior of transition-metal-doped materials such as Bi chalcogenides, which have been established as hosting TI surface states. Indeed, ferromagnetism was studied in a variety of transition-metal-doped chalcogenide compounds well before the interest in these materials as 3D TIs. For instance, ferromagnetic Curie temperatures (T_C) ranging up to 190 K were reported in bulk crystals of Bi_2Te_3 doped with V, Cr, Mn [54, 55, 56], and Fe [57], as well as in thin films grown by molecular beam epitaxy (MBE) [58]. More recent studies of magnetically doped chalcogenides, primarily driven by an interest in topological phenomena, have shown ferromagnetism in a variety of samples: bulk crystals of p-type, Mn-doped Bi_2Te_3 [59], and Fe-doped Bi_2Se_3 [60], as well as thin films of Cr-doped Bi_2Te_3 [61], Cr-doped Bi_2Se_3 [62], n-type, Mn-doped Bi_2Se_3 [48], and Cr-doped $(Bi_{1-x}Sb_x)_2(Te_{1-y}Se_y)_3$ [63, 64]. Other magnetic phases (paramagnetic, antiferromagnetic, and spin glass) have also been observed [56, 60]. Before drawing detailed conclusions about the influence of ferromagnetism on surface states, careful structural and magnetic characterization of these types of samples is needed. For instance, it was recently shown that nanoscale segregation of magnetic atoms can occur at the surface of thin films of Mn-doped Bi_2Se_3 [48], although macroscopic probes of ferromagnetism such as ferromagnetic resonance and polarized neutron reflectivity are consistent with a uniform bulk magnetization [65].

In this chapter, robust bulk ferromagnetism in n-type, Mn-doped bismuth telluride thin films grown by MBE will be demonstrated. At low Mn doping, these films are n type and in the tetradymite phase but still show similar values of T_C as the p-type, tetradymite bulk crystals of Mn-Bi_2Te_3 studied in the past [59]. At higher Mn doping, the crystalline phase changes to one in which some Bi_2Te_3 quintuple layers are separated by Bi bilayers, similar to earlier reports of ferromagnetic, n-type bulk crystals [66]. The next section describes the MBE synthesis of the Mn-doped bismuth telluride thin films. The following section discusses the crystal structure of the MBE-grown films, characterized by x-ray diffraction (XRD) and high-resolution transmission electron microscopy (HRTEM). I then discuss magnetization measurements using a superconducting quantum interference device (SQUID) magnetometry and polarized neutron reflectivity (PNR). The following section discusses measurements of magnetotransport and magnetic anisotropy that are consistent with the results of SQUID magnetometry. Finally, I compare the films to bulk samples and discuss the nature and origin of ferromagnetism in the Mn-doped bismuth telluride films.

Sample synthesis

The Mn-doped bismuth telluride thin films were epitaxially grown on InP(111)A substrates by MBE using high-purity elemental Bi, Mn, and Te in an ultrahigh vacuum ($\sim 10^{-10}$ Torr). Despite the van der Waals bonding to the substrate, the TI film quality is generally improved by reducing the lattice mismatch between the film and the substrate. InP(111)A was chosen because it has an in-plane lattice constant (4.150 Å), which is closer to Bi_2Te_3 (4.380 Å) than GaAs(111) (3.998 Å), Si(111) (3.840 Å), or sapphire (4.751 Å). The InP oxide was desorbed under an Se flux prior to growth, resulting in an approximately 1-nm-thick amorphous region at

the interface, as seen in Figure 3-2. To explore the role of the Mn concentration on the magnetic properties of Mn-doped bismuth telluride, thin films of a wide range of Bi to Mn beam equivalent pressure ratios were synthesized while maintaining a film thickness of ~28–30 nm. In addition, we grew a 68-nm sample for PNR measurements where the InP was desorbed under an As flux. The set of samples and their properties are listed in Table 3-1.

Table 3-1. List of undoped and Mn-doped bismuth telluride thin films with different Mn concentrations. Thickness, beam equivalent pressure ratio (Bi/Mn), Mn atomic percentage (20% relative error) measured and calculated by RBS and SIMS, 2D carrier concentration (n^{2D}), mobility (μ), existence of AHE by magnetotransport measurements, onset temperatures of AHE (±1 K error), and T_C by SQUID magnetometry for each sample are shown.

Sample	t (nm)	Mn/Bi	Mn (%)	n^{2D} (10^{13} cm^{-2})	μ (cm^2/V s)	AHE	T_C (AHE)	T_C (SQUID)
S1	28	0	0	2.9	620	X	–	–
S2	30	0.02	1	3.21	196	X	–	–
S3	30	0.04	2	10.1	98.2	O	11 K	13.8 K
S4	30	0.07	5	14.5	79.2	O	15 K	15.0 K
S5	30	0.13	10	6.51	73	O	16 K	17.0 K
S6	68	0.04	4.5	57.1	107	O	10 K	15.0 K

Crystal structure

The atomic compositions of Mn-doped bismuth telluride films S3, S5, and S6 were analyzed by secondary ion mass spectrometry (SIMS) depth profiles. The total Mn concentration in the highly doped film (S5) was determined by Rutherford backscattering (RBS) to be 10 atom % with 20% relative error. This concentration of S5 was then used to calibrate the SIMS measurements. Samples S1–S5 were of similar thicknesses and grown under similar conditions. The Mn concentration of S3 was found to be ~2% from SIMS and x-ray photoelectron

spectroscopy (XPS). The Mn concentrations of films S1 and S4 were then estimated to be 1% and 5%, respectively, using the Mn/Bi beam-equivalent-pressure ratios relative to S3 and S5. Sample S6 was thicker and was grown with a slightly different geometry in the chamber, resulting in a higher Mn concentration (4.5%) than would have been estimated from just the Mn/Bi pressure ratio relative to the other samples.

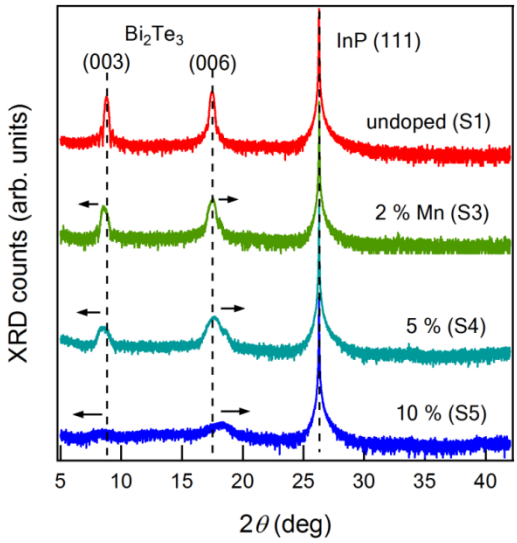

Figure 3-1. XRD of undoped (S1) and Mn-doped bismuth telluride thin films (S3, S4, and S5). (003) and (006) peaks of Bi_2Te_3 shift in opposite directions (black arrows) with increasing Mn concentration, while the (111) peak of InP does not change with Mn doping. Curves are offset for clarity.

The crystal structure of undoped and Mn-doped bismuth telluride films was studied by XRD and TEM. In Figure 3-1(a), the XRD pattern of the undoped film shows sharp Bi_2Te_3 (003) and (006) peaks. Mn doping broadens both peaks and, interestingly, causes the (003) and (006) peaks to shift in opposite directions, with shoulders forming at high Mn concentrations, indicating changes in the crystal structure. The crystal structure of the Mn-doped bismuth telluride film with 5% Mn (S4) was directly imaged by TEM. A basic structural unit of rhombohedral Bi_2Te_3 (tetradymite phase) is a quintuple layer (QL), which consists of five alternating atomic layers, Te-

Bi-Te-Bi-Te. Heavy elements, such as Bi, scatter the electron beam to large angles more effectively than lighter elements, such as Te, allowing the high-angle annular dark field (HAADF) scanning transmission electron microscopy (STEM) image in Figure 3-1(b) to show this elemental arrangement within the repeated QL structure as dim-bright-dim-bright-dim (corresponding to Te-Bi-Te-Bi-Te, as expected). However, a modified structure with additional atomic layers is seen in the upper part of the image. Consistent with the atomic contrast, this modified structure most likely corresponds to the formation of a Bi bilayer between two QLs, as reported in earlier studies of single crystals of bulk, Mn-doped BiTe [66]. This crystalline phase is distinct from tetradymite Bi_2Te_3 and is a member of the $(Bi_2Te_3)m(Bi_2)n$ homologous series. The shifts in the XRD are also consistent with such Bi-rich phases being present. Figures 3-2(b) and (c) show the atomic crystal structure of a QL-Bi_2-QL unit layer and two QLs, respectively. Larger-scale HAADF-STEM images suggest that such Bi bilayers are scattered randomly in different regions of the film. Similar to the case of Bi bilayers in Bi_2Se_3, we expect such a structure to retain its topological character [67]. Mn likely substitutes for Bi in both locations, but from electron energy loss spectroscopy (EELS) line scans, an interstitial position cannot be ruled out. From these TEM and XRD studies, we deduce that adding Mn into Bi_2Te_3 results in the formation of Bi bilayers, with the crystal structure gradually transitioning from pure tetradymite to $(Bi_2Te_3)m(Bi_2)n$, with n/m approaching 0.5 at high Mn concentrations. As we show later, this likely also leads to n doping.

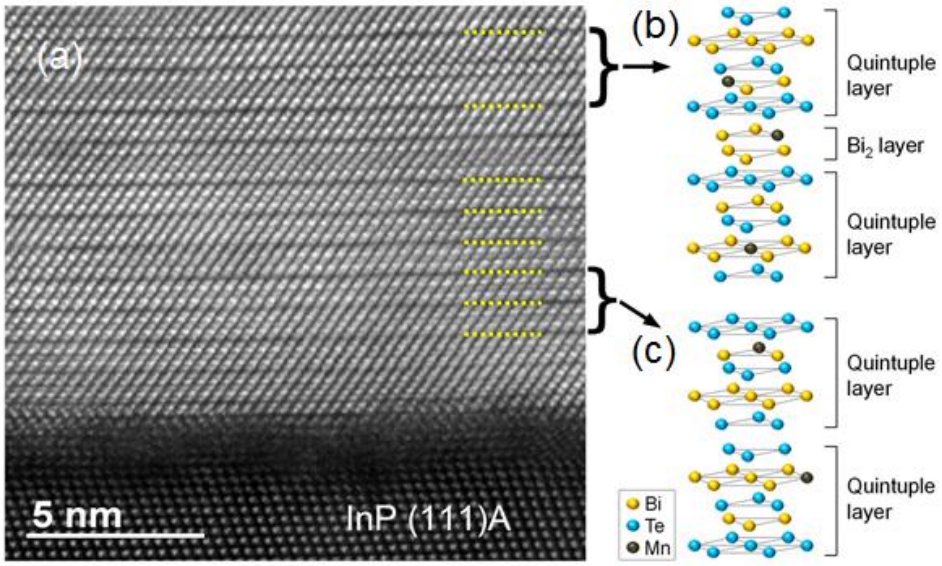

Figure 3-2. A HAADF-STEM image of a Mn-doped bismuth telluride thin film on an InP(111)A substrate with 5% Mn concentration (S4). Dotted yellow lines indicate QLs and unit layers composed of a Bi bilayer sandwiched between two QLs. The atomic crystal structures of (b) a QL-Bi_2-QL unit layer and (c) two Bi_2Te_3 QLs, with Bi partially substituted by Mn.

Magnetic characterization

SQUID magnetometry reveals the onset of ferromagnetism in the Mn-doped bismuth telluride thin films for Mn concentrations larger than 1%. Figure 3-3(a) shows the temperature dependence of the remanent magnetization in films with 2% (S3), 5% (S4), and 10% (S5) Mn concentrations, measured above 5 K after field cooling in a 9-kOe (for SI unit equivalence, 1 Oe = 79.6 A/m) magnetic field perpendicular to the plane (H // (0001)). The T_C of each film was determined by finding the steepest slope and extrapolating a linear fit to zero magnetization. Table I and the inset to Figure 3-3(a) show that the T_C of each is 13.8 K, 15.0 K, and 17.0 K, respectively. Focusing on S2 [Figure 3-3(b)], below T_C we observe ferromagnetic hysteresis of the magnetization with a perpendicular magnetic field. No significant hysteresis was observed with an in-plane magnetic field [H // (1100)]. Similar hysteretic behavior was observed in the

other samples, confirming that the magnetic easy axis is out of plane along the c axis of the Mn-doped bismuth telluride crystal.

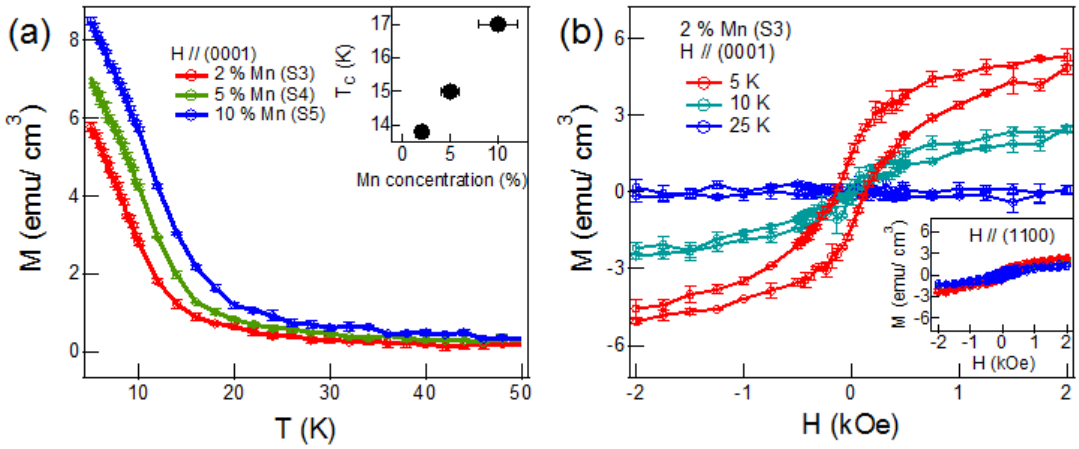

Figure 3-3. SQUID magnetometry. (a) Temperature dependence of magnetization with perpendicular-to-the-plane magnetic field for Mn-doped bismuth telluride thin films with 2% (S3), 5% (S4), and 10% (S5) Mn concentration. Inset plots T_C as a function of Mn concentration. (b) Magnetic field sweep of magnetization with perpendicular-to-the-plane magnetic field for a Mn-doped bismuth telluride thin film with 2% Mn concentration (S3). Inset shows magnetization with in-plane magnetic field sweep for S3 at 5 K (red), 10 K (green), and 25 K (blue). Note that the background magnetization of the InP substrate has been subtracted in (b), but not in the inset due to the negligible contribution of in-plane background. Error bars in (a) and (b) represent standard deviations for magnetization over multiple measurements.

Sample S6 was further studied by PNR at the NIST Center for Neutron Research (NCNR) on the Polarized Beam Reflectometer (PBR). This sample was thicker than the other samples in this study (~68 nm) and was capped with Te to protect the surface from exposure to the atmosphere. The sample was field cooled with an in-plane applied field of 8 kOe. The in-plane external field is necessary because, due to the neutron selection rules, the sample magnetization has to be aligned in plane to observe the magnetic structure. Measurements were then made at 5 K, 20 K, and 45 K (Figure 3-4) with a neutron wavelength of $\lambda = 4.75$ Å. Incident neutrons were

polarized parallel (+) or antiparallel (−) to the applied field, and the reflected (++), (−−) and spin-flip (+−), (−+) intensities were measured. These reflectivity curves include scattering contributions from both the structure and magnetism of the sample and were modeled to extract the parameters that best fit them using REFL1D [68]. The spin-flip intensities were insignificant, indicating that the sample magnetization was aligned with the external field. The difference between the (++) and (−−) reflectivities divided by their sum is called the spin asymmetry and is related to the magnetization of the sample as a function of depth. The sample was further measured by x-ray reflectivity (XRR) to help determine the layer thicknesses used in modeling the fits to the PNR data. The Mn-doped bismuth telluride layer was found to have a uniform scattering length density and magnetization through the thickness of the film [Figure 3-4(e)], with a magnetization of 23.2 emu/cm3 (1 emu = 10−3 A m^2), within about a factor of 2 of that measured from SQUID for this sample. No enhanced magnetism or dead layers at the TI surfaces were needed to model the data. Surprisingly, a highly reduced but measurable uniform magnetization was observed up to 45 K, well above the T_C measured by SQUID and transport measurements. We speculate that the PNR measurement may be averaging over small, randomly distributed regions in the sample that have a higher T_C than the bulk of the film and which were being aligned by the external field. These regions could be chemically different and comprised of Mn_3O_4, for example, which has a T_C near 45 K. This variation in structural composition is unlikely, however, since the film is capped with Te and the structural scattering length density of the film matches that expected for Mn-doped Bi_2Te_3 throughout its entire thickness.

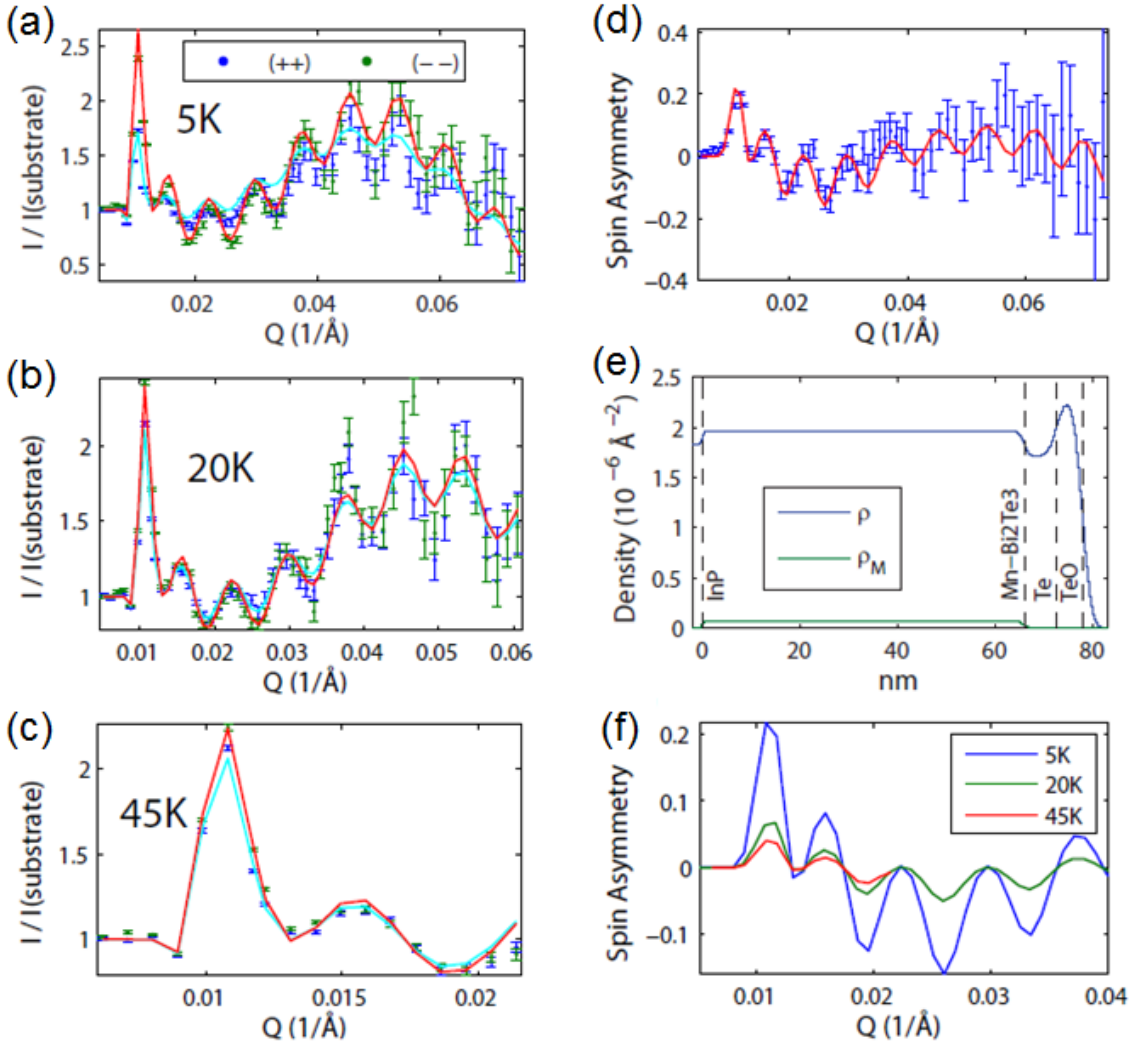

Figure 3-4. PNR magnetometry measured with an in-plane 8-kOe magnetic field. Reflectivity curves and fits (solid lines) for up (++) and down (−−) spin neutrons are plotted on a normalized Fresnel scale at (a) 5 K, (b) 20 K, and (c) 45 K. (d) Spin asymmetry and fit at 5 K. The error bars represent an uncertainly of +/− standard deviation. (e) Structural and magnetic scattering length densities from the 5-K fits for each layer of the sample. The magnetization, proportional to ρ_M (green curve), is uniform across the Mn-doped bismuth telluride layer. (f) Fits to spin asymmetry show a small but measurable magnetization persisting to 45 K, well above the T_C measured by SQUID magnetometry.

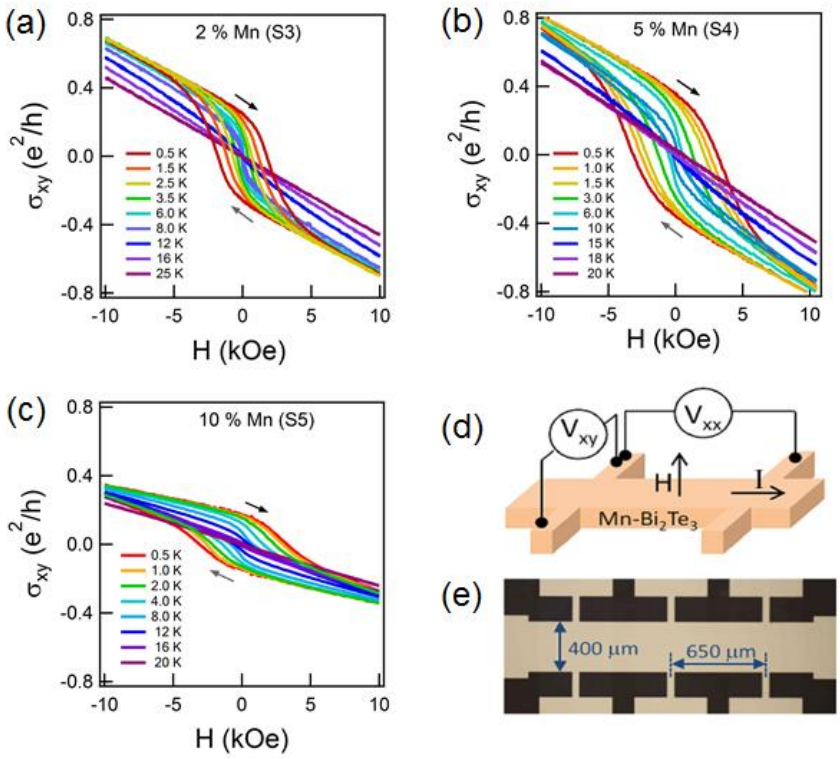

Figure 3-5. Hall conductivity obtained from magnetotransport measurements. A schematic of the measurement setup and a photo image of a Hall bar are shown in (d) and (e), respectively. Panels (a)–(c) show the temperature dependence of the Hall conductivity σ_{xy} for Mn-doped bismuth telluride films with 2% Mn (S3), 5% Mn (S4), and 10% (S5) Mn concentration.

Magnetoconductivity and Hall effect measurements

The carrier density and mobility of the thin films were determined by magnetotransport measurements using Hall bars with 650 × 400 μm^2 channels patterned by conventional photolithography and dry etched in an Ar/Cl plasma. Standard four-probe lock-in measurements at 19 Hz were conducted with perpendicular-to-plane magnetic fields up to 6 T at temperatures down to 0.5 K. A schematic of the measurement setup and an optical microscope image of a typical device are shown in Figures 3-5(d) and (e), respectively. The undoped Bi_2Te_3 film (S1) is n type with a two-dimensional (2D) carrier density of 2.9 × 10^{13} cm^{-2} at 4.2 K. The carrier density with the Fermi energy E_F located at the bottom of the conduction band is estimated to be 2.8 ×

10^{13} cm^{-2}, calculated from the Fermi surface at the conduction band bottom of Bi_2Te_3 obtained by angle-resolved photoelectron spectroscopy (ARPES) [20]. Thus E_F of the undoped Bi_2Te_3 (S1) is located just above the bottom of the conduction band. With increasing Mn doping, the carrier density increases and the chemical potential (E_F) of the Mn-doped films is in the conduction band (Table I). The n-type conductivity and the position of E_F in undoped and Mn-doped bismuth telluride thin films were confirmed by the IR optical measurements of samples of similar composition (but with thickness close to that of S6) [69]. The carrier concentration of sample S6 is somewhat larger than the similarly doped S3 due to its conductive Te capping layer.

We observed a strong anomalous Hall effect (AHE) in the samples with Mn concentrations of 2% or higher (S3, S4, and S5). Hall conductivity σ_{xy} versus perpendicular magnetic field at various temperatures reveals the evolution of the AHE. Figures 3-5(a)–(c) show the temperature dependence of σ_{xy} for S3, S4, and S5, respectively. At temperatures much higher than T_C, σ_{xy} shows a linear dependence on field, but as the temperature decreases the curve becomes nonlinear and then hysteretic below T_C. The onset temperature of the AHE is at around 11 K for 2% Mn concentration (S3). The coercive field gradually increases as the temperature decreases, reaching about 1.8 kOe at 0.5 K in sample S2. The Hall conductivity σ_{xy} is calculated from longitudinal resistivity ρ_{xx} and Hall resistivity ρ_{xy} as $\sigma_{xy} = \rho_{xy}/(\rho_{xy}^2 + \rho_{xx}^2)$, and σ_{xy} is composed of the normal Hall conductivity σ_{xy}^N and the anomalous Hall conductivity σ_{xy}^H as $\sigma_{xy} = \sigma_{xy}^N + \sigma_{xy}^H$. By subtracting the linear ordinary Hall conductivity σ_{xy}^N from σ_{xy}, one can obtain the anomalous Hall conductivity σ_{xy}^H. In Figure 3-6(a), we plot the anomalous Hall conductivity σ_{xy}^H versus perpendicular magnetic field at 0.5K for samples with different Mn concentrations (S3, S4, and S5). The coercive field is larger with higher Mn concentration, but the saturated σ_{xy}^H value is the largest with the intermediate doping (S4). In Figure 3-6(b), the temperature dependence of σ_{xy}^H at zero magnetic field from S3, S4, and S5 shows that the onset

temperature of the AHE hysteresis increases with Mn doping and is consistent with the results from the SQUID measurements.

Besides the AHE, the ferromagnetism in the Mn-doped bismuth telluride can also be seen from the longitudinal magnetoconductivity (MC) with a magnetic field perpendicular to the plane. For the film with 2% Mn concentration (S3), the longitudinal MC $\Delta\sigma_{xx}$ shows hysteresis below 4 K [Figure 3-6(c)]. The hysteretic dips in MC are readily attributed to well-known contributions from domain-wall scattering at the coercive field of the ferromagnet.

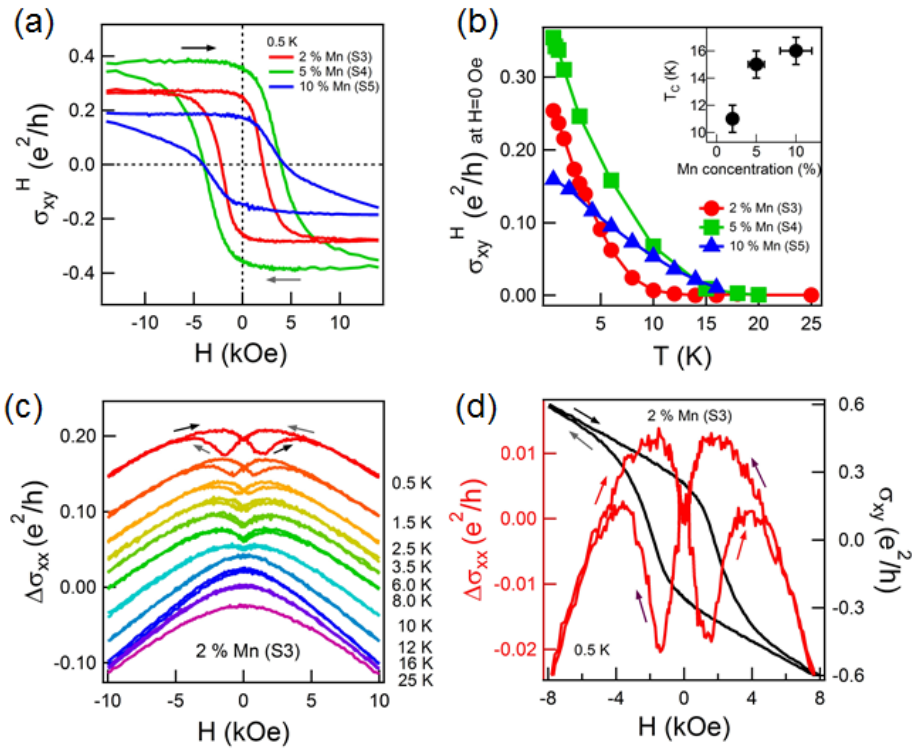

Figure 3-6. Anomalous Hall and longitudinal conductivity from magnetotransport measurements. (a) Anomalous Hall conductivity σ_{xy}^{H} at 0.5 K for various Mn concentrations (S3, S4, and S5). (b) Temperature dependence of σ_{xy} at zero magnetic field with different Mn concentrations (S3: red circles, S4: green squares, and S5: blue triangles). The inset plots T_C as a function of the Mn concentration. Black solid line is a linear fit. (c) Temperature dependence of longitudinal MC $\Delta\sigma_{xx}$ from sample S3. Ferromagnetic hysteresis is shown below 4 K. (d) Longitudinal conductivity $\Delta\sigma_{xx}$ (red) and Hall conductivity σ_{xy} (black) at 0.5 K.

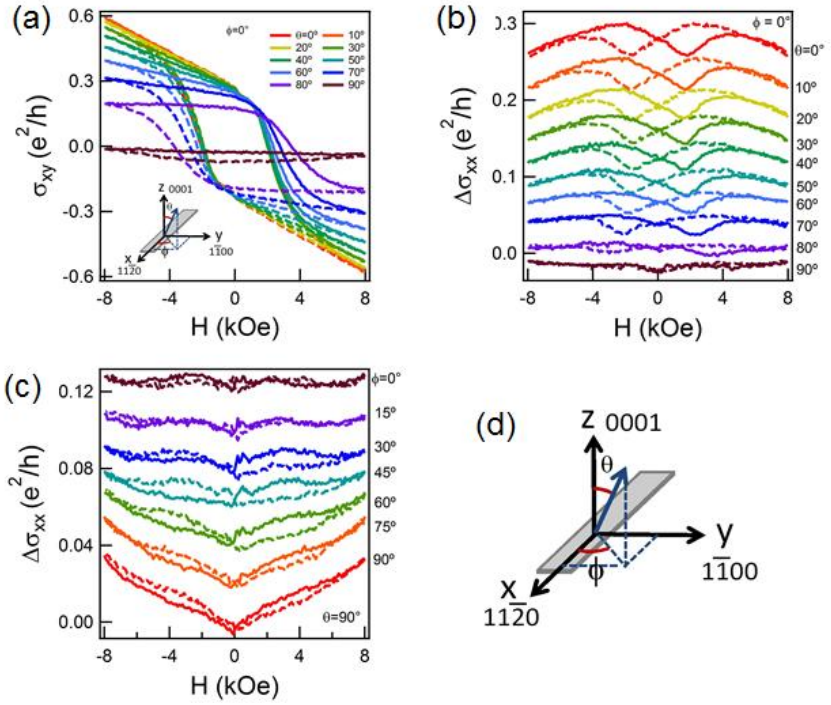

Figure 3-7. Angular dependence of Hall conductivity and longitudinal conductivity of an Mn-doped bismuth telluride thin film with 2% Mn concentration (S3) at 0.3 K. (a) Transverse conductivity σ_{xy} and (b) longitudinal MC $\Delta\sigma_{xx}$ with polar angles of the magnetic field from θ = 0◦ (perpendicular to the plane) to θ = 90◦ (in-plane along channel direction). Solid (dashed) curves are up sweeps (down sweeps). Offset for clarity. (c) Longitudinal MC $\Delta\sigma_{xx}$ with an in-plane magnetic field from φ = 0◦ (along current direction) to φ = 90◦ (perpendicular to the current direction). Offset for clarity. (d) A schematic of a channel with Cartesian coordinates and the corresponding crystal directions.

We also studied magnetotransport with different directions of the magnetic field using a cryogenic vector magnet system at 300mK. The angles θ and φ are defined as the polar angle along the c axis of the crystal and the azimuthal angle from a line along the channel direction of the Hall bar geometry, respectively [see inset to Figure 3-7(a)]. As the direction of the magnetic field changes from perpendicular to the plane (θ = 0°) to in-plane along the channel (θ = 90° and φ = 0°), the amplitude of the AHE hysteresis reduces gradually and disappears at θ = 90° [Figure 3-7(a)]. The magnetic field dependence of the transverse conductivity σ_{xy} is not completely flat at θ = 90° due to a slight misalignment (less than 1°) of the Hall bar geometry to the magnetic

field coordinate. The angular dependence of the longitudinal conductivity σ_{xx} reveals the evolution of the hysteresis by changing the polar angle θ with an azimuthal angle φ fixed to the channel direction, as shown in Figure 3-7(b). As θ increases from 0° to 90°, the magnitude of the hysteresis becomes smaller and the peak position broadens, following the coercive field obtained by transverse conductivity σ_{xy} at each angle. With a magnetic field parallel to the plane (θ = 90), large hysteresis is not shown with azimuth angles [Figure 5-7(c)]. The result of angular dependence of AHE and the longitudinal MC are consistent with SQUID data, which confirms that the easy axis of the Mn-doped bismuth telluride thin film is perpendicular to the plane along the c axis of the crystal.

Anisotropy magnetoresistance

The study of angular dependence of magnetotransport reveals the anisotropic magnetoresistance (AMR) in the Mn-doped bismuth telluride film by showing MC with different directions of the magnetic field sweep with respect to the direction of current [Figures 3-7(b) and 3-7(c)]. For further studies of AMR, we carried out magnetotransport measurements with a constant magnetic field of 5 kOe to saturate the magnetization of the Mn-doped bismuth telluride film(S3) and while sweeping through 360° in the xy plane and the zx plane. In conventional AMR, the magnetoresistivity is expressed as a function of the relative direction of magnetization and current [70]:

$$\rho = \rho_{||} + \left[\rho_{||} - \rho_{\perp}\right]\cos^2\varphi \tag{3.1}$$

where $\rho_{||}$ ($\rho_{\perp}$) is the resistivity with a current direction parallel (perpendicular) to the magnetization and φ is the angle between magnetization and current.

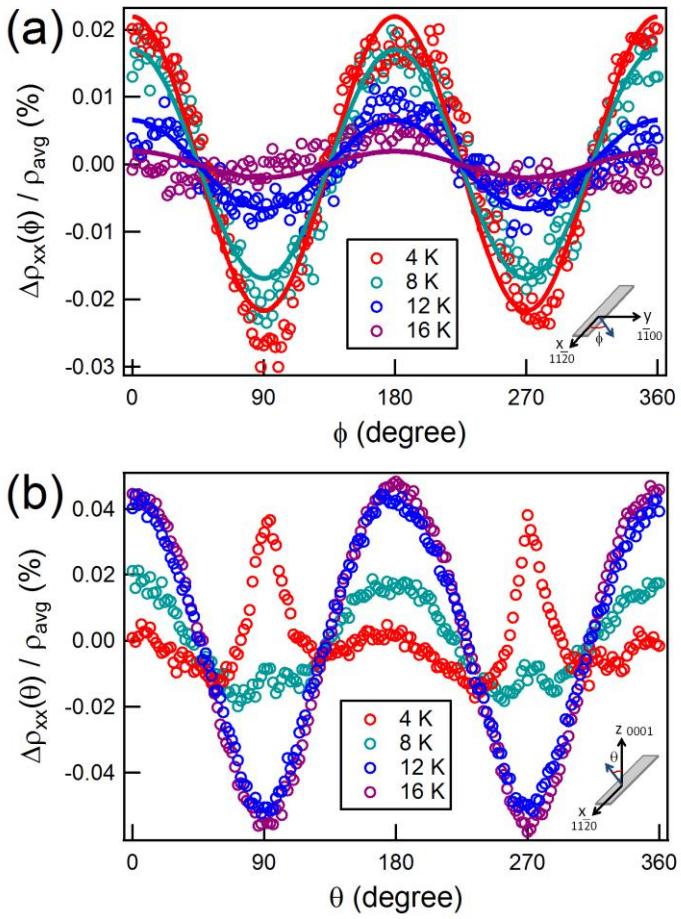

Figure 3-8. Ferromagnetic signatures of AMR in the Mn-doped bismuth telluride film with 2% Mn concentration (S3). Normalized resistivity $\Delta\rho_{xx}/\rho_{avg}$ at a fixed magnetic field (0.5 kOe) (a) with azimuthal angle φ in the xy plane and (b) with polar angle θ in the zx plane at different temperatures. In (a), solid lines are fits by Equation (1).

The magnetoresistivity with a rotating in-plane (xy plane) magnetic field fits well with Equation (3.1). In Figure 3-8(a), the anisotropy weakens as the temperature increases to the ferromagnetic T_C. We note that the magnetoresistivity at 16 K, which is above T_C, is not completely isotropic, which is understood as AMR that is present even in undoped 3D TIs [71, 48]. AMR of undoped films in the zx plane is known to be bigger than that in the xy plane, which explains the sizable AMR of the Mn-doped bismuth telluride film (S3) in the zx plane at 16 K, as shown in Figure 3-8(b). Interestingly, the AMR of S3 in the zx plane below T_C is suppressed as

temperature decreases and the enhancement in resistivity is observed as the magnetic field approaches the direction of current ($\theta = 90°$ and 270°). The AMR results are qualitatively consistent with the results of the angular dependence of the longitudinal MC with magnetic field sweep discussed in this section. The enhancement of resistivity near $\theta = 90°$ and 270° in the zx plane is attributed to the domain-wall scattering when the z component of magnetization flips from +z (−z) direction to −z (+z) direction.

Discussion

Our study of MBE-grown, Mn-doped bismuth telluride thin films is worth comparing with earlier reports on two distinct types of bulk crystals: Mn-doped Bi_2Te_3 and Mn-doped BiTe [59, 66]. Up to 2% Mn concentration, the crystal structure of the MBE-grown Mn-doped films is almost identical to that of pure Bi_2Te_3. In the study of $Bi_{2-x}Mn_xTe_3$ bulk crystals, ferromagnetism was reported over an Mn concentration range of 0.8–1.8 atomic percent ($0.04 \leq x \leq 0.09$) with 9 K $\leq T_C \leq$ 12 K [59]. Within that range, Mn behaved as an acceptor that substitutes for Bi in the Bi_2Te_3 crystal, and conduction was p type. This is similar to the values of T_C in sample S3, except that our sample is n type, suggesting that carrier-mediated ferromagnetism is not playing a role. At higher Mn concentrations in our study, the films gradually incorporate extra Bi bilayers with increasing Mn until the crystal structure becomes comparable to that reported for Mn-doped BiTe bulk crystals, which consisted of repeated structures of Bi bilayers between every other Bi_2Te_3 QL, with Mn atoms preferentially located in the Bi bilayers [66]. Those bulk crystals showed n-type conduction, as in our samples, and had a T_C around 10 K for comparable Mn concentrations (6.25 atom %). Our key conclusion is that neither crystal nor carrier type seems to be playing a dominant role in determining the nature of ferromagnetic order in Mn-doped Bi_2Te_3 or BiTe thin films and bulk crystals.

In conventional diluted magnetic semiconductors, such as (Ga,Mn)As and (In,Mn)As, the ferromagnetic interaction between local moments is mediated via itinerant carriers located in either the valence band or in an impurity band. In a mean-field Zener model, T_C increases with carrier density and with Mn concentration [72]. We do not observe any obvious dependence of T_C on carrier density in our n-type Mn-doped bismuth telluride films. IR spectroscopy studies carried out on thick Mn-doped bismuth telluride samples also suggest that charge carriers are not likely mediators of ferromagnetism, showing little change in the IR spectrum upon cooling across T_C [69]. It is well known that carrier-density-independent ferromagnetism could possibly arise in an inhomogeneous, phase-separated material that contains either readily observable metallic, ferromagnetic inclusions or nanoscale metallic, ferromagnetic phases [73]. Our detailed structural studies clearly rule out the former possibility and—to the extent possible with our present microscopy studies—we do not see any obvious signs of the latter. One of the possible interpretations of the carrier-independent ferromagnetism in the Mn-doped bismuth telluride films is that it is of the van Vleck type, where magnetic impurities are coupled by a large magnetic susceptibility of the band electrons [25]. Ferromagnetism in MBE-grown, Cr-doped $(Bi_xSb_{1-x})_2Te_3$ thin films has been attributed to this mechanism [64]. Another possibility is that of ferromagnetism mediated by Dirac fermions in the surface states [50, 74]. Studies of exfoliated, Mn-doped $Bi_2Te_{3-y}Se_y$ crystals where the chemical potential was gated into the bulk band gap saw an increase in the size of the AHE, a signal similar to that observed in Cr-doped samples, and speculated that the ferromagnetic order was mediated by Dirac electrons [53]. Since the chemical potential in our samples clearly lies in the bulk conduction band, we cannot conclusively address this question. We note, though, that the surface states overlap the conduction band in energy; thus the presence of Dirac electron-mediated exchange might be expected to result in an enhanced ferromagnetic order at the surface, distinct from ferromagnetism in the bulk. However, our PNR

measurements do not show any such signatures, leading us to believe that the van Vleck mechanism is mostly likely responsible for the ferromagnetism observed in our samples.

Conclusions

In conclusion, we have carried out the synthesis and detailed characterization of magnetically doped TI thin films of Mn-doped bismuth telluride grown by MBE. Mn doping induces changes in the crystal structure of Bi_2Te_3, observed by XRD and high-resolution TEM. SQUID magnetometry as well as measurements of AHE as a function of angle revealed ferromagnetism below 17 K with a perpendicular-to-plane easy axis. Our results suggest carrier-independent ferromagnetism in Mn-doped bismuth telluride thin films. Experiments on Mn-doped bismuth telluride films with a wider range of Mn concentrations and with E_F in the bulk band gap are required to further confirm the mechanism of the ferromagnetism. Understanding the ferromagnetic properties of Mn-doped bismuth telluride thin films could possibly provide another pathway to explore the quantum phenomena caused by broken TRS in TI surface states.

Chapter 4

Breaking TR symmetry in ferromagnet/topological insulator heterostructures

In the previous chapter, a detailed study of the magnetically doped three-dimensional (3D) topological insulator (TI) Mn-doped Bi2Te3 was demonstrated as an approach to breaking time-reversal (TR) symmetry. In this chapter, we study a different approach of interfacing a TI with a magnetic layer. The studied model system is a hybrid TI-ferromagnetic (FM) heterostructure wherein a $Ga_{1-x}Mn_xAs$ (FM) with out-of-plane magnetic anisotropy is cleanly interfaced with $Bi_{2-x}Sb_xTe_{3-y}Se_y$ (TI) by molecular beam epitaxy (MBE). From electrical transport measurements of a top-gated heterostructure device, we observed a crossover from positive magneto-conductance to negative magneto-conductance as well as a systematic emergence of an anomalous Hall effect (AHE) as the temperature is lowered or as the chemical potential approaches the Dirac point. The results are interpreted as the opening of a gap at the Dirac point as a result of the exchange coupling between one topological insulator surface state and the ferromagnetic $Ga_{1-x}Mn_xAs$ layer. This suggests that the hybrid system is well suited to explore topological quantum phenomena and to realize hybrid topological insulator/ferromagnet spintronics applications.

Introduction

A 3D TI is characterized by its surface state, which is protected by TR symmetry [1, 2, 3, 10, 11]. The TR symmetry can be broken by doping a TI with magnetic atoms or interfacing a TI surface with a magnetic layer, causing an energy gap opening at the Dirac point in the surface state [22, 50, 51, 52]. Unique quantum phenomena resulting from the broken TR symmetry have been predicted, such as topological magneto-electric effect [22], image magnetic monopole effect

[24], topological Kerr and Faraday rotation [22], and quantum anomalous Hall effect [25]. With the motivation for such effects, synthesis and characterization of magnetically doped 3D TIs with transition metals, such as Mn, Fe, Gd, and Cr have been studied [53, 48, 65, 49, 59, 51, 75, 60, 76, 77, 67, 63, 64, 78, 61, 62], and evidence of a gap opening by broken TR symmetry in magnetically doped TI systems has been demonstrated by direct probe of angle-resolved photoemission spectroscopy (ARPES) [51, 27, 48, 78]. In addition, a spin-resolved ARPES experiment revealed the hedgehog-like spin texture in Mn-doped Bi_2Se_3 films [27]. Also, one of the predicted quantum phenomena, the quantum anomalous Hall effect, was recently demonstrated in ultrathin Cr-doped $(Bi,Sb)_2Te_3$ films [26].

In this chapter, we focus on another way of breaking TR symmetry in TI surface states: interfacing a TI surface to a magnetic layer, especially an insulating FM, to evidence the broken TR symmetry and ultimately to realize topological quantum phenomena and potential spintronics applications. The key advantage of a TI/FM heterostructure over the magnetically doped TI system is the selective modification of one surface by the FM and, in more complicated structures, the possible modification of top and bottom surfaces independently. Magnetic proximity affects only the interfaced surface; thus magnetic properties or the resulting effects are free from the magnetism of bulk or another surface of the TI layer, which, in the case of magnetically doped TI systems, needs to be carefully characterized. To further separate the FM-interfaced TI surface from the electrical coupling to bulk or another surface, the chemical potential needs to be placed in the bulk band gap, and the TI film needs to be thick enough to avoid the surface-to-surface tunneling that can open a hybridization gap in the surface state [21]. To study the magnetic proximity, clean, well-defined TI/ FM interface is necessary. There should also be minimal conduction through the FM, and the FM should have a magnetization component perpendicular to the TI surface to break the TR symmetry. With such a structure, wherein two surfaces are

separated and well-defined, one can study phenomena that are relevant to one surface, such as half quantum Hall effect (or parity anomaly).

TI/FM heterostructures have been experimentally reported using Bi_2Se_3 thin films interfaced with EuS or GdN as FM layers [79, 80, 81]. An EuS-induced ferromagnetic phase in MBE-grown Bi_2Se_3 film was claimed with an assumption of a perpendicular magnetic domain forming at the interface [79]. In the similar structure of Bi_2Se_3 film on EuS, synthesized by pulsed laser deposition, unusual negative magneto-resistance was observed for ultrathin Bi_2Se_3 layers in which top and bottom surfaces were coupled and was interpreted in terms of magnetic proximity effect [80]. Weak anti-localization (WAL) was also suppressed in MBE-grown Bi_2Se_3 films capped by a sputtered ferromagnetic layer of GdN [81]. Recently, a Bi_2Se_3/yttrium iron garnet (YIG) heterostructure has been demonstrated to evidence the magnetic coupling between the Bi_2Se_3 and the ferromagnet insulator YIG up to 130 K [82].

Synthesis and characterization of TI/FM heterostructures

We demonstrate a new approach for a TI/FM heterostructure using a dilute magnetic semiconductor (Ga,Mn)As. The ferromagnetic Curie temperature T_C, resistivity, and magnetic easy axis of (Ga,Mn)As films can be engineered by factors such as the amount of Mn-doping, annealing, and strain [72, 83, 84]. As a desired FM for a TI/FM heterostructure, highly resistive $(Ga_{1-x}Mn_x)As$ with a perpendicular-to-plane component of magnetization is necessary. The high resistivity was achieved by low Mn-doping of $x \approx 0.01$. To obtain the perpendicular component of magnetization, a (Ga,Mn)As film (10 nm) was grown on InP(111)A substrate by MBE.

The superconducting quantum interference device (SQUID) magnetometry on $(Ga_{0.99}Mn_{0.01})As$ with a TI film on top reveals $T_C \approx 50$ K with a magnetic field perpendicular to

plane, as shown in Figure 4-1(a). Clear hysteresis loops were seen with a perpendicular magnetic field below the Tc [Figure 4-1(b)].

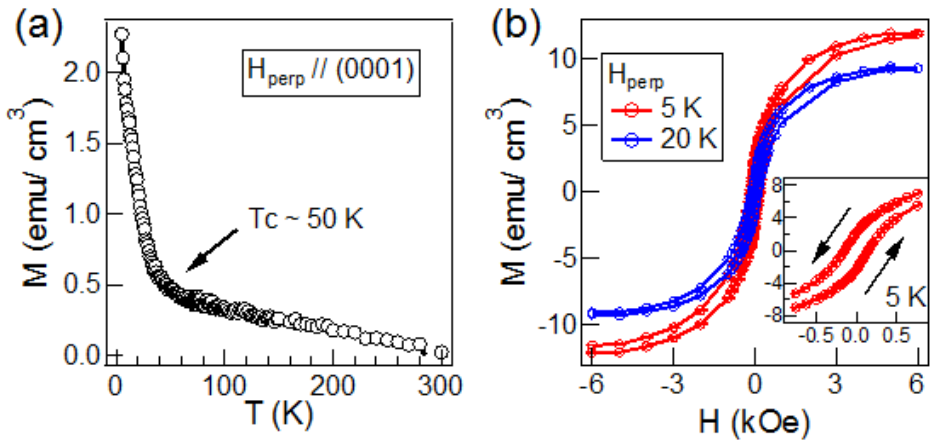

Figure 4-1. SQUID magnetometry of a $(Bi,Sb)_2(Te,Se)_3$/(Ga,Mn)As heterostructure. (a) Temperature dependence of magnetization with perpendicular-to-the-plane magnetic field for the BiSbTe2Se/$(Ga_{0.99}Mn_{0.01})$As heterostructure. T_C of the (Ga,Mn)As layer is around 50 K. (b) Magnetic field sweep of magnetization with perpendicular-to-the-plane magnetic field below T_C of the (Ga,Mn)As layer. Clear hysteresis was observed, as shown in the inset.

The resulting crystal structure of (Ga,Mn)As film on InP(111)A substrate is GaAs(111) structure. In Figure 4-2, x-ray diffraction (XRD) of the (Ga,Mn)As film with a $(Bi,Sb)_2(Te,Se)_3$ film grown on top shows a peak close to the expected position of the GaAs(111) line. The slight offset of the $(Ga_{0.99}Mn_{0.01})$As peak from the GaAs(111) line is due to the modified GaAs lattice constant by Mn substitutions and defects due to the low temperature growth of (Ga,Mn)As. An advantage of (Ga,Mn)As as an FM for a TI/FM heterostructure is the well-defined interface without any amorphous growth or secondary phases, as demonstrated in the previous work of epitaxial growth of Bi-chalcogenide TIs on GaAs(111) crystal [85]. The clean interfaces between adjacent layers are shown in the high-resolution transmission electron microscopy (TEM) image and energy-dispersive spectrometer (EDS) scanning transmission electron microscopy (STEM) image in Figures 4-3 and 4-4.

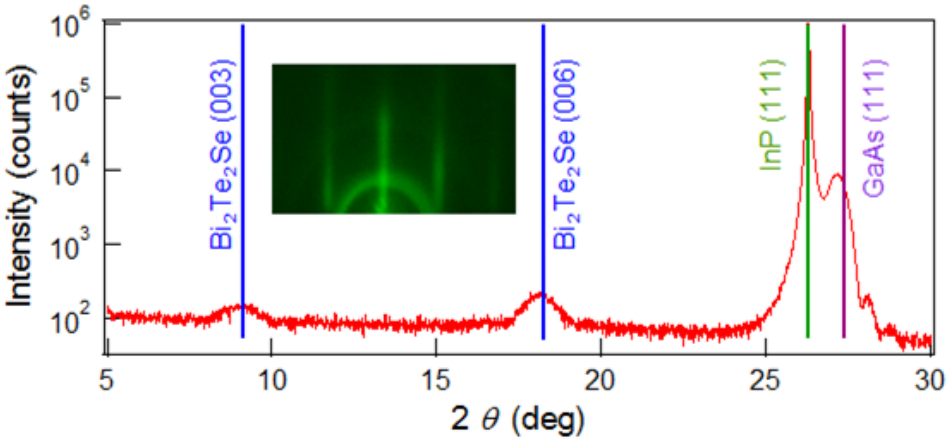

Figure 4-2. XRD of the $(Bi,Sb)_2(Te,Se)_3$/(Ga,Mn)As heterostructure on InP(111)A substrate. Blue, green, and violet lines are calculated positions of Bi_2Te_2Se(003), Bi_2Te_2Se(006), InP(111), and GaAs(111) peaks. The inset is the typical reflection high-energy electron diffraction patterns observed during the $(Bi,Sb)_2(Te,Se)_3$ film growth.

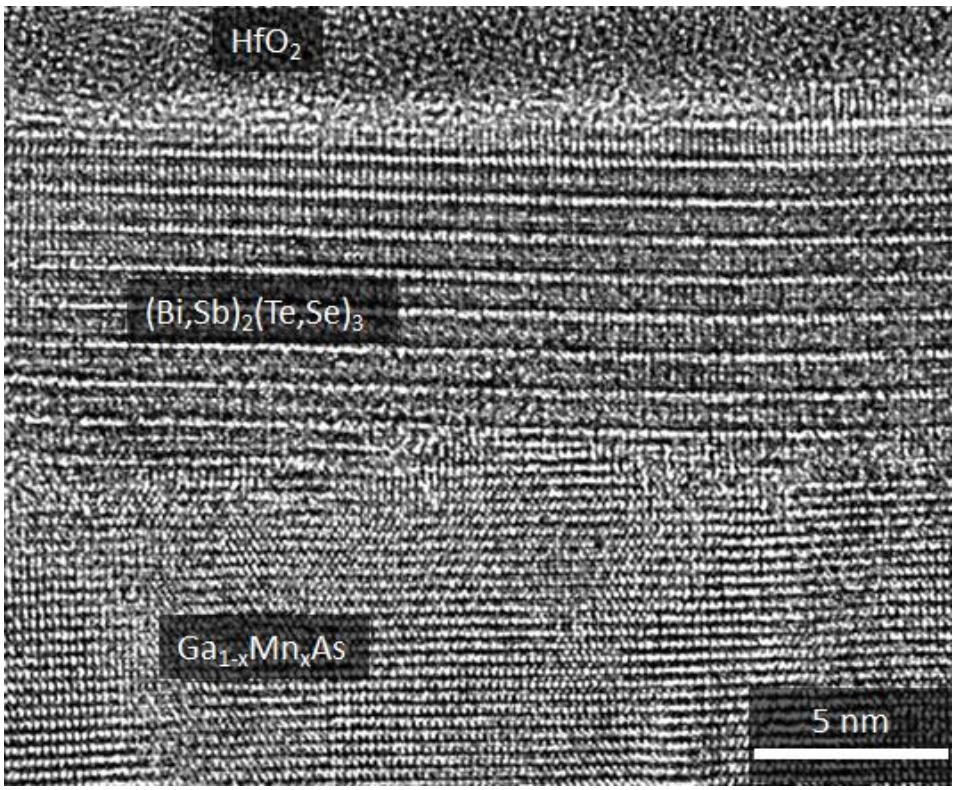

Figure 4-3. High-resolution TEM image of $(Bi,Sb)_2(Te,Se)_3$/(Ga,Mn)As heterostructure with a HfO_2 layer on the TI film. Well-defined interface is seen at the interface of TI/FM.

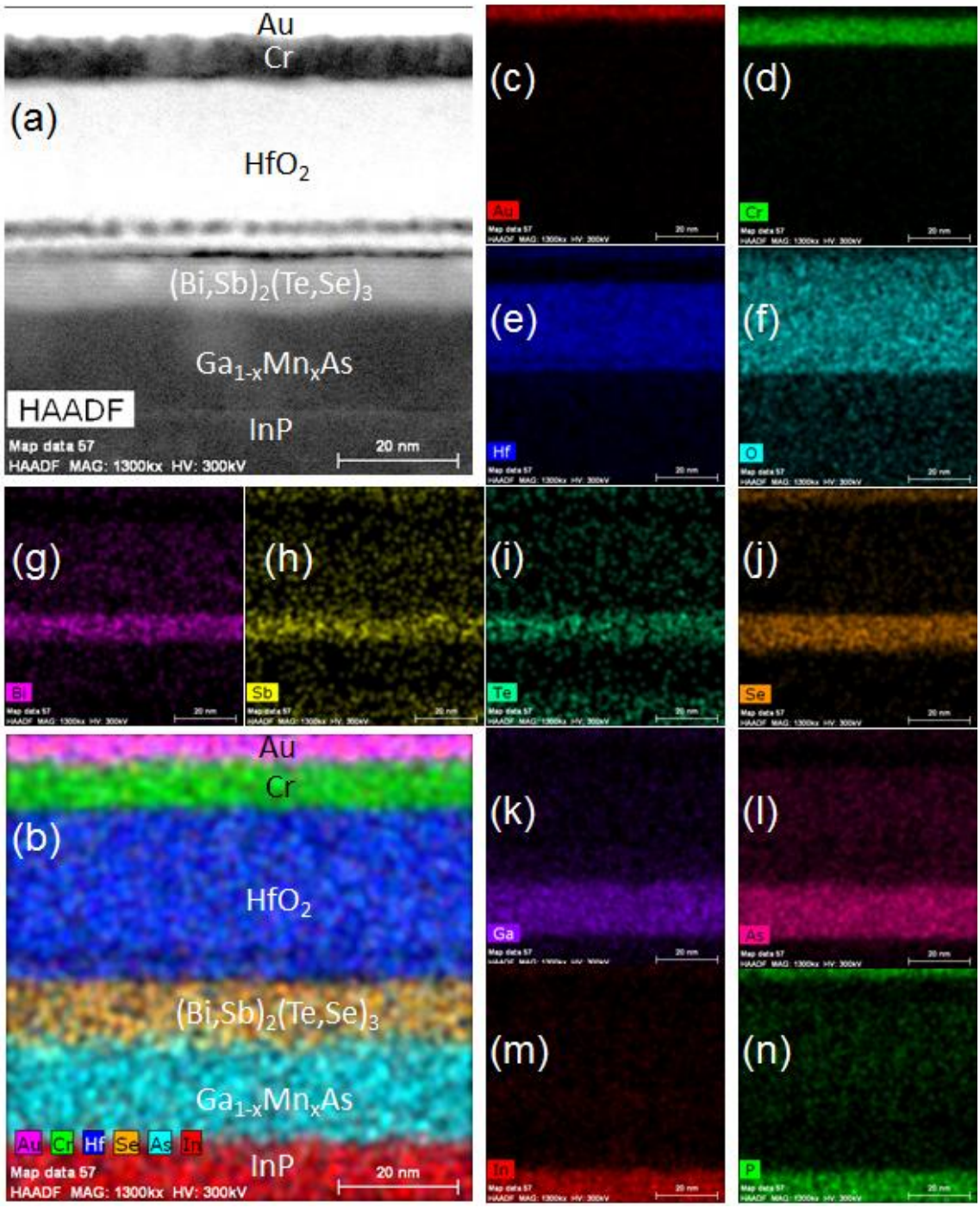

Figure 4-4. (a) High-angle annular dark field (HAADF) STEM image of an Au/HfO_2 top-gated $(Bi,Sb)_2(Te,Se)_3$/(Ga,Mn)As heterostructure. (b) EDS mapping image of Au, Cr, Hf, Se, As, and In, which represent each layer of the top-gated heterostructure device. (c-n) EDS mapping for each element of (c) Au, (d) Cr, (e) Hf, (f) O, (g) Bi, (h) Sb, (i) Te, (j) Se, (k) Ga, (l) As, (m) In, and (n) P.

Top-gated Hall-bar device and ambipolar transport

Although the selective modification of one TI surface interfaced with an FM is an advantage, as mentioned earlier, the buried interface between TI and FM restricts direct probing of the modified TI surface state by ARPES or scanning tunneling microscopy. However, electrical transport measurements provide a route to evidence the modification in the surface state by quantum corrections in the magneto-conductance (MC) and also by AHE. For the transport measurements, we fabricated a top-gated Hall-bar device with high-κ dielectric HfO_2 and Au/Cr gate metal by standard photo-lithography [Figure 4-5 (a)].

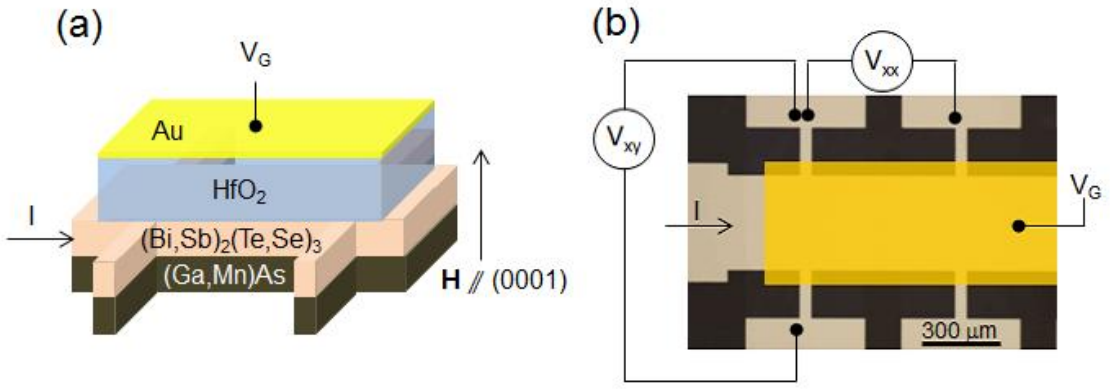

Figure 4-5. (a) A schematic of a top-gated TI/FM Hall-bar device. (d) An optical microscope image of the Hall-bar device (650 × 400 μm^2) with false-colored Au gate metal and the measurement description.

One important question for the electrical transport laterally through the heterostructure is whether a current flows only through the TI layer. The black curve in Figure 4-6(a) is the resistivity when the current flows through the whole TI/FM heterostructure while the red curve shows the resistivity of only the (Ga,Mn)As layer after the TI overlayer was carefully removed by low-power (15 W) Ar plasma. Since the resistivity of the (Ga,Mn)As is more than five orders of

magnitude higher than that of the heterostructure below 30 K, we conclude that the current flows mostly through the TI layer.

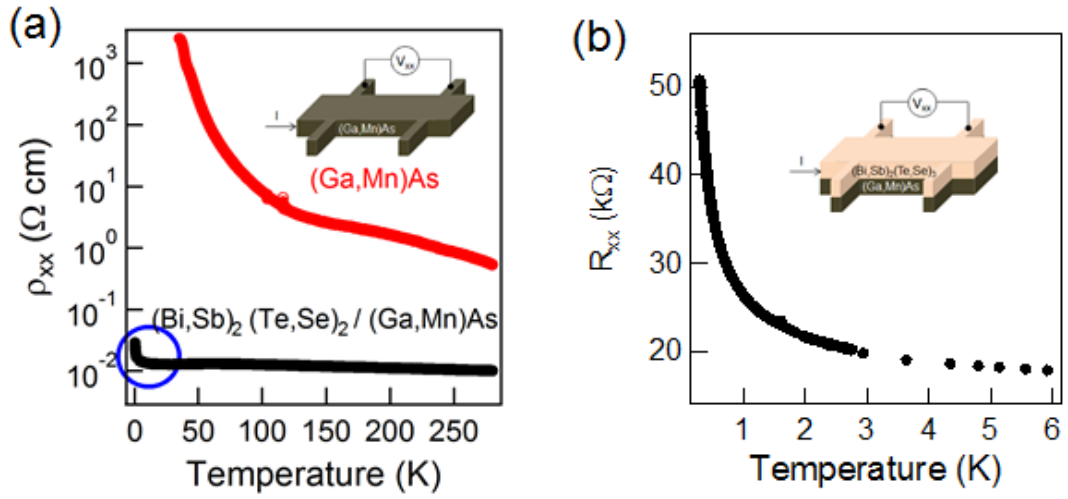

Figure 4-6. (a) Temperature dependence of resistivity of $(Bi,Sb)_2(Te,Se)_3$/(Ga,Mn)As heterostructure channel (black circles) and of only (Ga,Mn)As channel (red circles). Inset is a schematic of device and measurement description of (Ga,Mn)As layer. (b) The longitudinal sheet resistance R_{xx} of $(Bi,Sb)_2(Te,Se)_3$/(Ga,Mn)As heterostructure in the low-temperature regime, marked as a blue circle in (a). Inset is a schematic of device and measurement description of the TI/FM heterostructure.

Longitudinal sheet resistance R_{xx} and Hall resistance R_{xy} of the top-gated TI/FM device as a function of gate voltage show the typical ambipolar transport behavior of TI films (Figures 4-7). R_{xy} changes its sign at around V_G = 0.3 V while R_{xx} meets maximum at V_G = -1.3 V, indicating that the chemical potential is tuned from a position above the Dirac point to a position below the Dirac point near the top of the valence band. The mismatch of the gate-voltages of the charge neutrality point and the R_{xx} peak reveals that the carrier densities of top and bottom surfaces at a certain gate voltage do not match each other, and the two surfaces could even have different types of carriers in a certain range of gate voltage. We cannot determine the position of the chemical potential of the bottom surface interfaced with FM solely from the gate-dependence

of the channel resistance and the Hall resistance of the whole TI layer, but careful studies of quantum corrections to MC and AHE make it possible to determine the position of the chemical potential of the bottom surface.

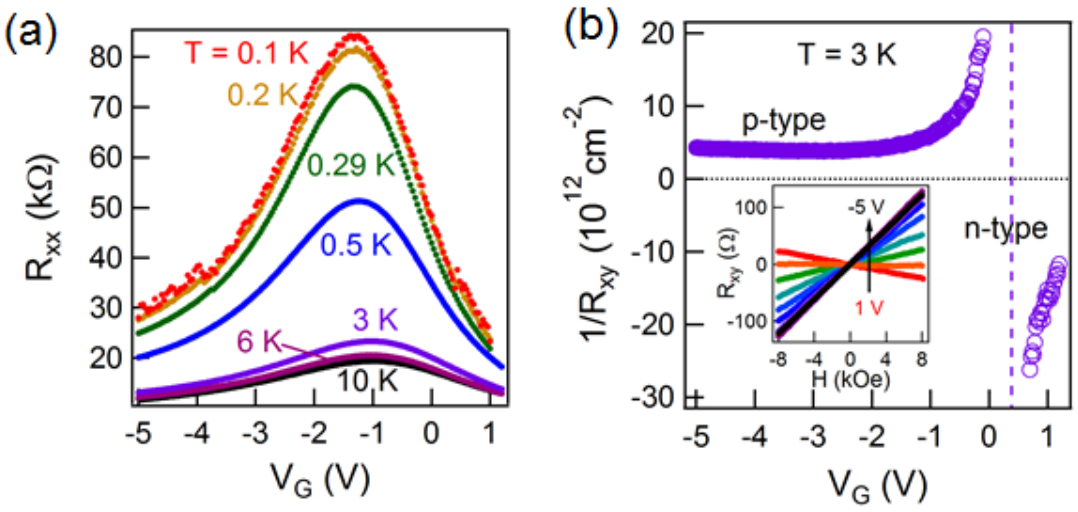

Figure 4-7. (a) Gate-voltage dependence of the longitudinal sheet resistance R_{xx} with zero magnetic field at different temperatures from 0.1 K (red) to 10 K (black). (f) Inverse of Hall resistance R_{xy} in the unit of 2D carrier concentration at 3 K. Inset shows results of Hall measurements with different gate voltages from 1 V to -5 V at 3 K.

Quantum corrections in MC

We now discuss the results of magneto-transport measurements of a top-gated Hall-bar device with both varying temperature [Figure 4-8(a)] and tuning gate-voltage [Figures 4-9(a) and (b)]. In Figure 4-8(a), at a fixed gate-voltage (-5 V) MC with temperature down to 3 K shows positive, parabolic behavior. As the temperature decreases, the positive MC becomes sharper near zero magnetic field, and at lower temperatures below 1 K the positive MC gradually changes to negative MC. One salient feature in the crossover regime is the coexistence of a positive MC peak near zero magnetic field and negative MC for larger magnetic fields. Interestingly, a similar crossover from positive MC to negative MC is also seen with lowering gate voltages at fixed

temperatures (0.1 K and 0.29 K) in Figures 4-9(a) and (b). The two, similar crossovers in MC by temperature dependence as well as by gate-voltage dependence suggest the possibility that there is one physical picture that could explain the effect for both cases.

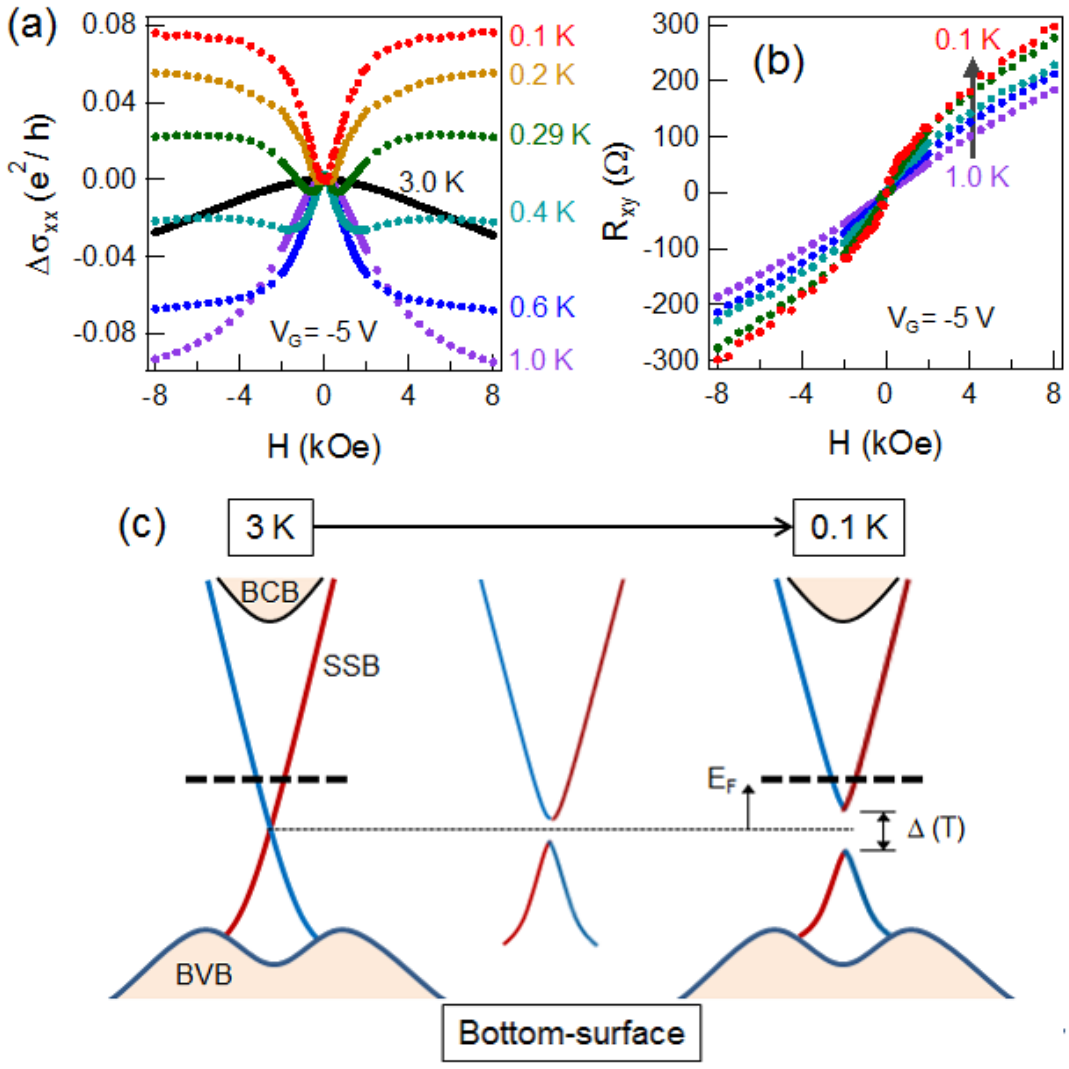

Figure 4-8. Temperature dependence of MC and Hall resistance R_{xy}. (a) Crossover between positive MC (WAL) and negative MC (WL) with a temperature range of 3.0 - 0.1 K at V_G = -5 V. (b) Hall resistance R_{xy} vs. magnetic field below 1.0 K. Clearer AHE is seen as temperature decreases. (c) A cartoon of the band diagram of the bottom-surface. Below 3 K, an energy gap opens, and the size of the energy gap widens as temperature decreases.

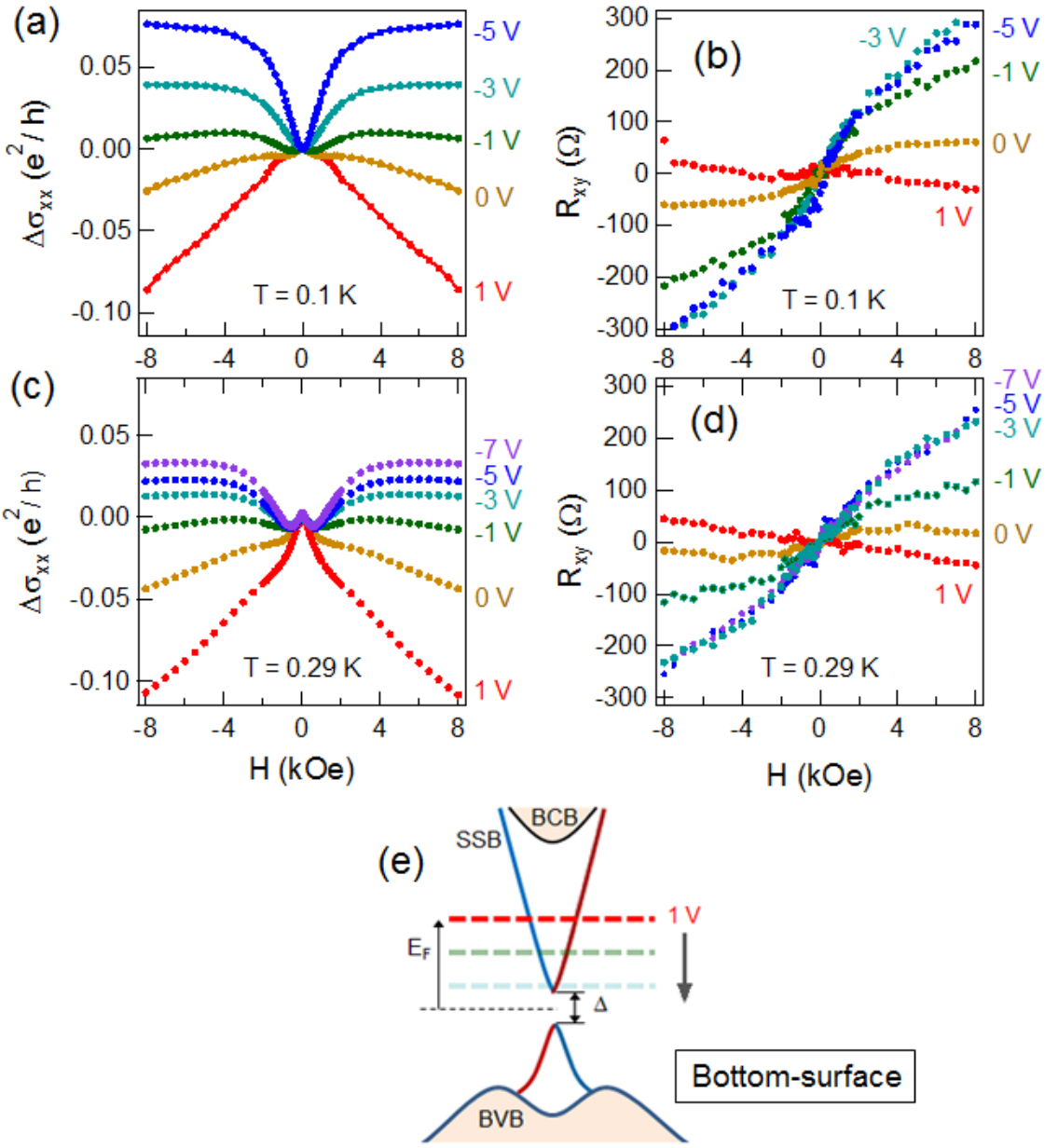

Figure 4-9. Gate-voltage dependence of MC and Hall resistance R_{xy}. (a,b) MC with applied gate voltages at 0.1 K and 0.29 K, respectively. Crossover from positive MC (WAL) to negative MC (WL) observed as gate voltage decreases from 1 V. (c,d) Hall resistance R_{xy} vs. magnetic field with applied gate voltages at 0.1 K and 0.29 K, respectively. The sign change of the slope indicates n- to p-type carrier change by applying gate voltage. AHE is observed near zero magnetic field. (e) A cartoon of the band diagram of the bottom surface interfaced with (Ga,Mn)As. The size of an opened gap Δ is fixed at a certain temperature and the chemical potential is tuned from above and towards the energy gap as the gate voltage decreases from 1 V.

Weak antilocalization and weak localization

The corrections to the classical MC near zero magnetic field can be understood as quantum corrections of WAL and weak localization (WL). For diffusive transport in a disordered metal, the presence (absence) of spin-orbit coupling results in destructive (constructive) interference between time-reversal paths around self-intersecting loops when phase coherence is maintained and thus leads to a quantum enhancement of the classical conductivity known as WAL [86] (WL). Applying a magnetic field adds a phase difference to the paths, destroying the interference and resulting in a negative (positive) MC for the WAL (WL) case. For diffusive transport in a conventional 2D metal, the MC due to WAL and WL is described by the Hikami-Larkin-Nagaoka (HLN) equation [87]:

$$\Delta\sigma(H) = \alpha \frac{e^2}{2\pi^2 h}\left[\psi\left(\frac{1}{2}+\frac{\hbar c}{4el_\phi^2 H}\right) - \ln\left(\frac{\hbar c}{4el_\phi^2 H}\right)\right] \tag{4.1}$$

where α is a prefactor, $\psi(x)$ is the digamma function, and l_ϕ is the coherence length. WAL leads to $\alpha = -1/2$ (symplectic case) while WL by constructive interference leads to $\alpha = 1$ (orthogonal case). In 3D TIs where spin and momentum are strongly "locked," WAL naturally arises from the π Berry phase of electrons going around the Fermi circle of the Dirac surface state [88]. The quantum corrections to the MC for the Dirac surface states are expected to follow the behavior of the HLN formula for a conventional 2D metal with strong spin-orbit coupling. For an ideal 3D TI, when the Fermi energy E_F lies in the bulk conduction band (BCB) or the bulk valence band (BVB), the top and bottom surfaces are coupled by the conducting bulk, and one can expect the prefactor $\alpha = -1/2$, while α becomes -1 when E_F moves into the bulk band gap where the top and bottom surfaces are decoupled by the insulating bulk [89, 90]. We note that the exact value of α can depend on inter-channel scattering [89]. In our case we must consider: 1) the bulk-surface coupling, which is controlled by electrical gating, as well as 2) the effect of magnetic exchange

coupling on the bottom surface of the TI layer. Expected effects of interfacing FM are, as introduced in the beginning of this chapter, the TR symmetry breaking and the resulting gap opening at the Dirac point of the surface state. The π-Berry phase of the TI surface state is believed to be modified by the size of the gap (Δ), as a function of the position of E_F, and brings the crossover between WAL and WL [91].

Crossover between WAL and WL

The modification of the Berry phase $\varphi = \pi(1 - \Delta/2E_F)$ is the most probable explanation of our results with E_F tuned by electrical gating and the magnetic gap Δ opened by the broken TR symmetry by the exchange-coupling with the adjacent FM. When the gap is small or E_F is far away from the Dirac point ($E_F \gg \Delta$), the Berry phase remains as π, leading to WAL. On the other hand, when E_F approaches the gap by lowering gate voltages or when the size of the gap Δ increases by lowering the temperatures, the Berry phase approaches 0, leading to WL. The crossover between WAL and WL in MC has been experimentally demonstrated in TI systems with energy gaps opened by either hybridization or magnetic doping/proximity: ultrathin films in which top and bottom surfaces are hybridized to open a gap [92], magnetically doped TI films in which magnetic ordering opens a gap [48, 61, 93], ultrathin films with magnetic doping [38], and a ultrathin film interfaced with FM [80]. The distinguishing features of our system from the so-far experimentally demonstrated TI systems in terms of the crossover in MC are studies of a magnetic gap in relatively thick TI films with no contribution from hybridization for gap opening and demonstration of the crossover by varying not only the temperature but also the gate voltage in such a system. Particularly, in certain regimes of temperatures and gate voltages, we observe the unique coexistence of a WAL peak near zero magnetic field and WL behaviors at larger

magnetic fields, indicating at least two decoupled transport channels with different dephasing lengths.

Two-carrier model for two TI surfaces

Here we set up a model for lateral transport in a TI film of which the bottom surface is interfaced with FM. An important point to consider is the strength of the coupling between top and bottom surfaces. In the range of gate voltage (-5 V − 1 V) of the studied device, the chemical potential of TI is mostly in the region where the bulk is depleted and the top and bottom surfaces are decoupled, given that the carrier concentration ($n_{2D} \cong 4.3 \times 10^{12}\text{cm}^{-2}$) at V_G = -5 V is low enough to place the chemical potential in the bulk band gap, while at V_G = 1 V the chemical potential is still in the ambipolar transport region [Figure 4-7(b)]. Another evidence of the decoupled surfaces can be seen in the coexistence of WL and WAL at a given temperature and gate voltage. For example, as gate voltage is tuned from -5 V to 1V at 0.29 K, MC becomes negative (WL) for larger magnetic fields while the positive peak (WAL) is still observed for small magnetic fields near zero, as shown in Figure 4-9(b). A gapless surface state results in WAL corrections to MC. We speculate that the contribution of the WL transition is not from the gapless surface state but from the modified surface state of the bottom surface interfacing an FM. The persisting WAL peak near zero magnetic field comes from the gapless surface state of the top surface decoupled from the bottom surface.

For quantitative studies of WAL and WL, we use the HLN equation. Assuming a lateral transport through a TI film with no magnetic proximity, fitting the measured MC with a one-band HLN equation (Equation (4-1) would be expected to give a prefactor α of -1, where each surface contributes -1/2, resulting in α = -1 [94, 95, 96]. In this case, one surface state is modified by the adjacent FM, and, as expected, we do not observe α approaching -1 using a one-band HLN fitting.

If the two surfaces are electrically decoupled, modifying one surface would not affect the α = -1/2 contribution of the another surface. This is the case of our TI system, in which one surface state is modified by the adjacent FM. We do not observe α approaching -1 by one-band HLN fitting. Thus we use a two-carrier model for decoupled top and bottom surfaces with the first prefactor α_0 fixed to -1/2 for a gapless surface state:

$$\Delta\sigma(H) = \sum_{i=0,1} \alpha_i \frac{e^2}{2\pi^2 h} [\psi\left(\frac{1}{2} + \frac{\hbar c}{4el_{\phi,i}^2 H}\right) - \ln\left(\frac{\hbar c}{4el_{\phi,i}^2 H}\right)] \quad (4.2)$$

The values of α_1 of the bottom surface provide an indirect way to estimate E_F position of the bottom surface. At a given temperature, the size of a gap does not change, but the E_F is tunable by electrical gating. Figure 4-10(a) shows that α_1 increases as the gate voltage decreases from 1 V to -5 V (-7 V) at 0.1 K (0.29 K), interpreted as the E_F of the bottom surface is tuned from a position above and towards the magnetic gap, but not below it, as illustrated in Figure 4-9(e). This phenomenon qualitatively agrees with the WAL-WL crossover when the Berry phase is tuned away from π by reducing the Fermi energy closer to the magnetic gap.

Now the gate voltage is fixed at -5 V to place the E_F close to the gap, and α_1 increases as temperature decreases in Figure 4-10(b), interpreted as the size of the magnetic gap Δ widening as the temperature is lowered due to the exchange-coupling with the (Ga,Mn)As layer, as illustrated in Figure 4-8(c).

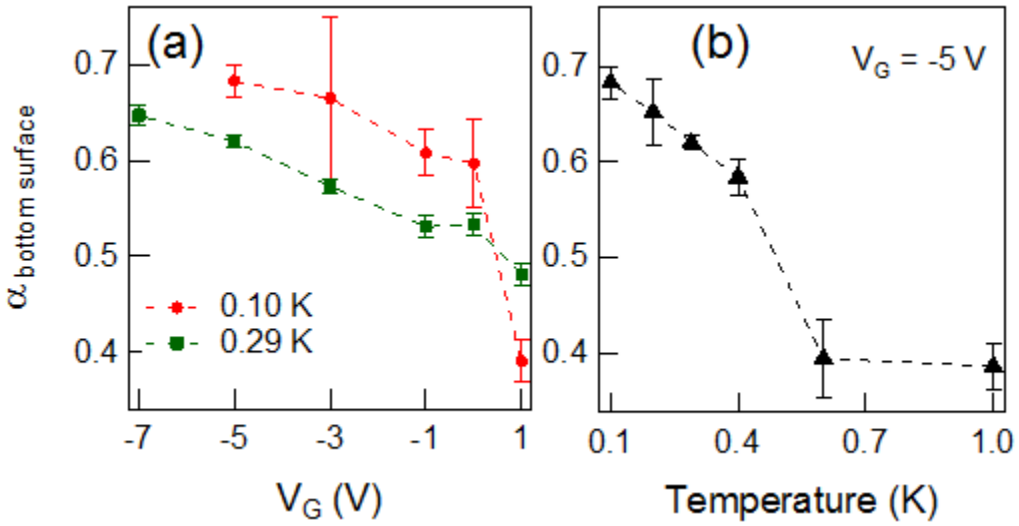

Figure 4-10. The systematic emergence of WL. (a) Gate voltage dependence of the prefactor α_1 for bottom surface ($\alpha_{\text{bottom surface}}$) at 0.10 K (red circles) and 0.29 K (green squares), fit by Equation (4.2). (b) Temperature dependence of the prefactor $\alpha_{\text{bottom surface}}$ with V_G = -5 V (black triangles). Error bars represent an uncertainty with 95 percent confidence.

Anomalous Hall effect

From the Hall measurements [Figure 4-8(b) and Figures 4-9(c,d)], we observed a systematic emergence of AHE as the temperature decreases or as the chemical potential is lowered by tuning gate voltages. However, the absence of hysteresis of the AHE indicates that long-range magnetic ordering is not induced in the bottom surface of the TI film by the adjacent (Ga,Mn)As layer in the range of temperatures (100 mK - 10 K) and gate voltages (-7 V - 1 V) measured.

The emergence of the AHE can be caused by opening an energy gap in the TI surface state, consistent with the interpretation for the crossover in MC. To understand the anomalous Hall contribution from interface between TI and FM, we consider a 2D Dirac model with a finite energy gap (Δ), with the Hamiltonian written as

$$H(k) = \hbar v_F\left(k_x\sigma_y - k_y\sigma_x\right) + \frac{\Delta}{2}\sigma_z, \tag{4.3}$$

where $\sigma_{x,yz}$ are the Pauli matrices with basis states of spin-up and spin-down states of real spin, and v_F is the Fermi velocity. The Hall conductance can be evaluated from the TKNN formula [7], and for the above two-band model, a simplified version is given by

$$\sigma_{xy} = \frac{e^2}{h}\int \frac{d^2k}{4\pi}\hat{\mathbf{d}}\cdot\left(\frac{\partial \mathbf{d}}{\partial k_x}\times\frac{\partial \mathbf{d}}{\partial k_y}\right) \tag{4.4}$$

with the **d** vector defined as $d_x = -\hbar v_F k_y$, $d_y = \hbar v_F k_x$, $d_z = \Delta/2$, $d^2 = (\hbar v_F)^2k^2 + (\Delta/2)^2$, and $\hat{\mathbf{d}} = \mathbf{d}/|\mathbf{d}|$**.** Calculation of Equation (4.4) using the given **d** vector for the above two-band model gives

$$\sigma_{xy}\left(E_F < \frac{|\Delta|}{2}\right) = \frac{e^2}{2h} \tag{4.5}$$

in the insulating regime, in which all the contributions of Hall conductivity come from the valence band.

For the metallic regime where E_F lies above the gap ($E_F > |\Delta|/2$), we have additional contribution to Hall conductivity from the conduction band besides the contribution from the valence band, which is given by

$$\sigma_{xy}^{c} = -\frac{e^2}{h}\int_0^{k_F}\frac{d^2k}{4\pi|d|^3}\mathbf{d}\cdot\left(\frac{\partial \mathbf{d}}{\partial k_x}\times\frac{\partial \mathbf{d}}{\partial k_y}\right). \tag{4.6}$$

The minus sign accounts for the opposite contribution from the conduction band. Calculation with above **d** vector makes the Hall conductivity as

$$\sigma_{xy}^{c} = \frac{e^2}{2h}\left[\frac{\Delta}{2}\left((\hbar v_F)^2k^2 + \left(\frac{\Delta}{2}\right)^2\right)^{-1/2} - 1)\right]. \tag{4.7}$$

Therefore, the total Hall conductivity for the metallic regime is

$$\sigma_{xy}\left(E_F > \frac{|\Delta|}{2}\right) = \frac{e^2}{2h}\frac{\Delta}{2E_F} \tag{4.8}$$

with $E_F = \sqrt{(\hbar v_F)^2 k^2 + \left(\frac{\Delta}{2}\right)^2}$. Equation (4.8) shows that the Hall conductivity is half-quantized in the insulating regime of a single Dirac model, and the half-integer quantum Hall conductivity monotonically decreases as E_F moves higher above the energy gap or as the gap gradually closes with an E_F fixed to a position near the gap.

Since our results are not in the regime of the quantized Hall conductivity, the observed Hall conductivity is smaller than $e^2/2h$; however, the observed conductivity follows the qualitative behavior of Equation (4.8). Figures 4-11(c) inset and (d) inset clearly show the systematic emergence of the anomalous Hall term R_{xy}^{AH} with respect to the gate voltage and temperature, where R_{xy}^{AH} is obtained after subtracting the ordinary Hall term R_{xy}^{OH} from the Hall resistance as $R_{xy}^{AH} = R_{xy} - R_{xy}^{OH}$. In the figures, we show R_{xy}^{AH} instead of σ_{xy}^{AH} since, in the calculation of $\sigma_{xy} = R_{xy}/(R_{xx}^2 + R_{xy}^2)$, the R_{xx} term contains a large contribution from the top surface, which makes it difficult to distinguish the effects only from the bottom surface. The expression for R_{xy} from σ_{xy} can be written as:

$$R_{xy}\left(E_F > \frac{|\Delta|}{2}\right) = \frac{\sigma_{xy}}{\sigma_{xx}^2 + \sigma_{xy}^2} \cong \frac{m^2}{2he^2\tau^2}\frac{1}{n^2}\frac{\Delta}{2E_F} \tag{4.9}$$

with σ_{xx} from the Drude model $\sigma_{xx} = e^2\tau n/m$ where n, m, and τ are the carrier density, the effective mass, and the relaxation time between collisions. For $E_F > |\Delta|/2$, n increases as E_F increases (moves away from the gap). Similarly, in the Hall conductivity, the change in R_{xy} reveals a systematic modification of the energy gap and the chemical potential.

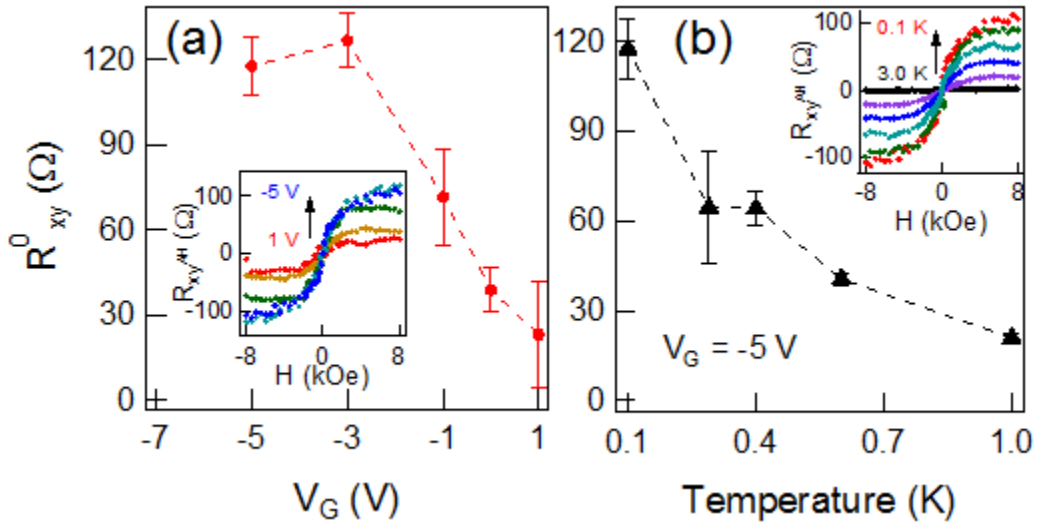

Figure 4-11. The systematic emergence of AHE. (a) Gate voltage dependence of the anomalous Hall resistance R^0_{xy} at 0.10 K (red circles). Inset is the anomalous Hall resistance R^{AH}_{xy} at each V_G: 1 V (red), 0 V (orange), -1 V (green), -3 V (cyan), and -5 V (blue). (d) Temperature dependence of R^0_{xy} with V_G = -5 V. Inset is the anomalous Hall resistance R^{AH}_{xy} at 3.0 K (black), 1.0 K (violet), 0.6 K (blue), 0.4 K (cyan), 0.29 K (green), and 0.1 K (red). Error bars represent an uncertainty with 95 percent confidence.

As the chemical potential lowers, approaching the energy gap by tuning the gate voltage from 1 V to -5 V, the estimated magnitude of the anomalous Hall resistance R^0_{xy} increases. R^0_{xy} is the intercept obtained by extrapolating a linear line of the high-field Hall resistance. In the case of a closed gap ($\Delta = 0$), R^0_{xy} is zero. When a gap opens and widens, the non-zero R^0_{xy} monotonically increases. Figure 4-11(b) shows the monotonic increase of the anomalous Hall resistance R^0_{xy} with decreasing temperature, interpreted as the widening of the gap with decreasing temperature. Similarly, Figure 4-11(a) shows the evolution of R^0_{xy} as the chemical potential lowers towards the energy gap. The interpretation of both temperature dependence and gate-voltage dependence of the AHE as a result of the magnetic gap opening is consistent with the interpretation of the systematic quantum corrections to the MC with varying temperature and gate voltage, discussed in the previous section.

The onset temperature of AHE as well as WL is much smaller than the T_C of the adjacent FM layer, indicating that the exchange-coupling between electrons in the TI bottom surface and Mn moments in (Ga,Mn)As is much weaker than the exchange coupling between Mn moments in (Ga,Mn)As (Figure 4-12).

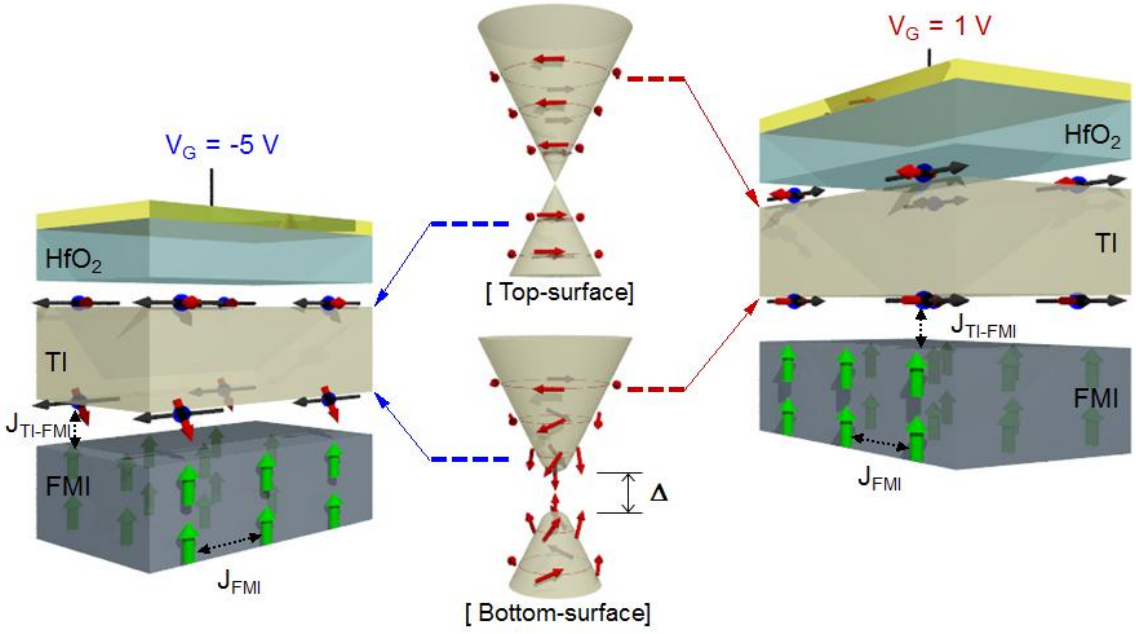

Figure 4-12. A schematic of a gapless Dirac surface state for the top surface, a magnetic-gapped surface state with hedgehog spin texture for the bottom surface, and top-gated TI/FM heterostructure devices with V_G = -5 and 1 V. Green arrows represent the magnetization of the FM (Ga,Mn)As layer, and gray arrows and red arrows in TI layer represent the directions of electron propagation and its spin, respectively. J_{FM} is the exchange-coupling constant between Mn moments in (Ga,Mn)As while J_{TI-FM} is the relatively weaker exchange-coupling constant between electrons in TI bottom surface and Mn moments in (Ga,Mn)As.

Summary

In summary, we synthesized and characterized a TI/FM heterostructure of a TI film $(Bi,Sb)_2(Te,Se)_3$ on a dilute magnetic semiconductor (Ga,Mn)As. The $(Ga_{0.99}Mn_{0.01})As$ layer is highly resistive, with a perpendicular component of magnetization below ~50 K. With an optimal

Bi to Sb ratio, the chemical potential was placed in the surface state, further tuned by electrical top-gating. The crossover between WAL and WL, as well as the systematic emergence of AHE, was observed with varying temperature and gate voltage, interpreted as a result of a gap opening in the Dirac surface state due to the TR symmetry breaking by the exchange-coupling between the TI surface state and the adjacent (Ga,Mn)As. The results suggest that the systematic changes in MC and AHE can be used as indirect probes to estimate the E_F position and the existence of the magnetic gap opening in the modified surface state.

Chapter 5

Electrical detection of a spin-polarized topological insulator surface state

In this chapter, we study the use of a topological insulator (TI) as a spin generator for potential spintronics applications. We demonstrate the electrical detection of the inherent spin polarization of TI using a magnetic tunnel junction. TI $(Bi,Sb)_2Te_3$ thin film was synthesized by molecular beam epitaxy with an optimal composition of Bi and Sb to place the chemical potential in the surface state. With a permalloy (Py)/Al_2O_3 magnetic tunnel junction fabricated on a $(Bi,Sb)_2Te_3$ channel, we observed hysteretic spin signals occurring at the magnetic switching field of the ferromagnet. The results are interpreted in terms of the interaction between the spin-polarized current on a TI surface and the magnetization of the ferromagnet. The detection of the spin polarization on a topological insulator is an essential step towards spintronics applications of TI.

Introduction

A three-dimensional (3D) TI has spin-polarized, gapless Dirac surface states in the bulk band gap induced by strong spin-orbit coupling [1, 2, 3]. The inherent spin polarization of the surface state is a unique property of TI for spintronics applications, as suggested by the proposals for potential TI spintronics devices [5, 97]. But it is only recently that experiments directly related to spintronics and the current information technologies have been demonstrated in TI systems. Spin transfer torque generated by TI Bi_2Se_3 films turned out to be the strongest among the spin-torque source materials measured to date [42]. The magnetization switching through giant spin-orbit torque induced by an in-plane current was observed in a magnetically-doped-TI/TI bilayer

system [98]. Detection of the inverse spin Hall effect by spin-pumping in Bi_2Se_3 suggests that Bi_2Se_3 is a viable material for spin detection devices [99].

Direct detection of the spin-polarized surface state by electrical transport measurements has been a great challenge, while the spin-helical Dirac surface state has been optically probed by spin-resolved, angle-resolved photoemission spectroscopy measurements [88]. Theoretical proposals have suggested that the spin-momentum locking of the surface state results in a change of magneto-resistance in a TI system with a ferromagnetic metal contact for injection or detection of the spin-polarized current [32, 33]. Additionally, very recently, electrical detection of spin polarization due to the spin-momentum locking in Bi_2Se_3 was demonstrated in spite of the high bulk conduction with the chemical potential lying in the conduction band [34].

In this chapter, we study the electrical probing of the spin-polarized surface state in TI thin films with suppressed bulk conduction. When a current is flowing through a TI film, the direction of the spin polarization on the top surface is opposite to that on the bottom surface. If the top and bottom surfaces are coupled by bulk conduction, the resulting spin signals from each surface will cancel each other. Thus, with the chemical potential placed in the bulk band gap, an enhancement of the detected spin signal is anticipated due to the spin-polarized current of one surface that is electrically decoupled from another surface.

Synthesis and characterization

We have grown 3D TI $(Bi,Sb)_2Te_3$ thin films on semi-insulating InP(111)A substrates by molecular beam epitaxy (MBE) in an ultrahigh vacuum ($< 2 \times 10^{-10}$ Torr). 10-nm-thick single crystalline $(Bi,Sb)_2Te_3$ films were synthesized by thermal evaporation of elemental Bi, Sb, and Te using conventional Knudsen cells. The ratio of Bi and Sb composition was carefully determined to be 1:1 to place the chemical potential into the bulk band gap. During the growth, the surface of

the single crystalline film is monitored by reflection high-energy electron diffraction (RHEED), as shown in Figure 5-1(a).

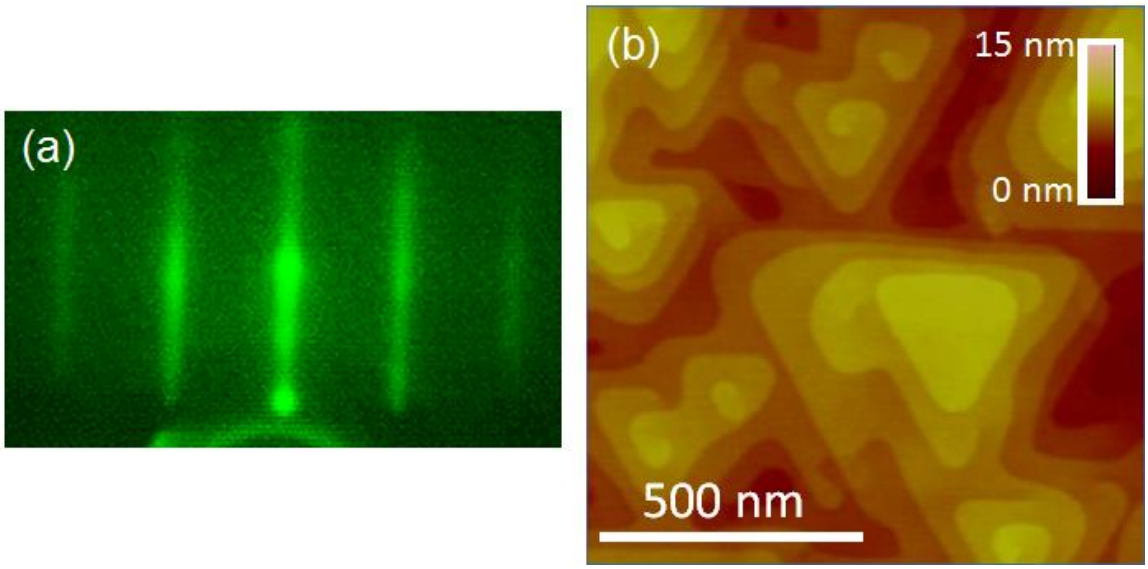

Figure 5-1. (a) Streaky RHEED patterns observed during the MBE growth of a $(Bi,Sb)_2Te_3$ film. (b) A typical AFM image of a surface of a $(Bi,Sb)_2Te_3$ film.

Electrical properties of a $(Bi,Sb)_2Te_3$ thin film were characterized by electrical transport measurements using a Hall-bar geometry with a channel dimension of 200 × 600 μm^2. Hall measurement [Figure 5-2(a)] reveals that the conduction of the film is by n-type carriers with a calculated 2D carrier density of 2.04×10^{13} cm^{-2} at 4.2 K, which suggests that the chemical potential is below the bottom of the conduction band since the carrier density of Bi_2Te_3 is estimated to be 2.8×10^{13} cm^{-2} when the chemical potential is placed at the bottom of the conduction band. The longitudinal magneto-resistance with a magnetic field perpendicular to the plane shows the quantum corrections of weak anti-localization (WAL) to the classical MR near zero magnetic field at 4.2 K [Figure 5-2(b)]. As discussed in a section of chapter 4, WAL is observed in 3D TIs due to the π Berry phase of electrons in the Dirac surface state [88].

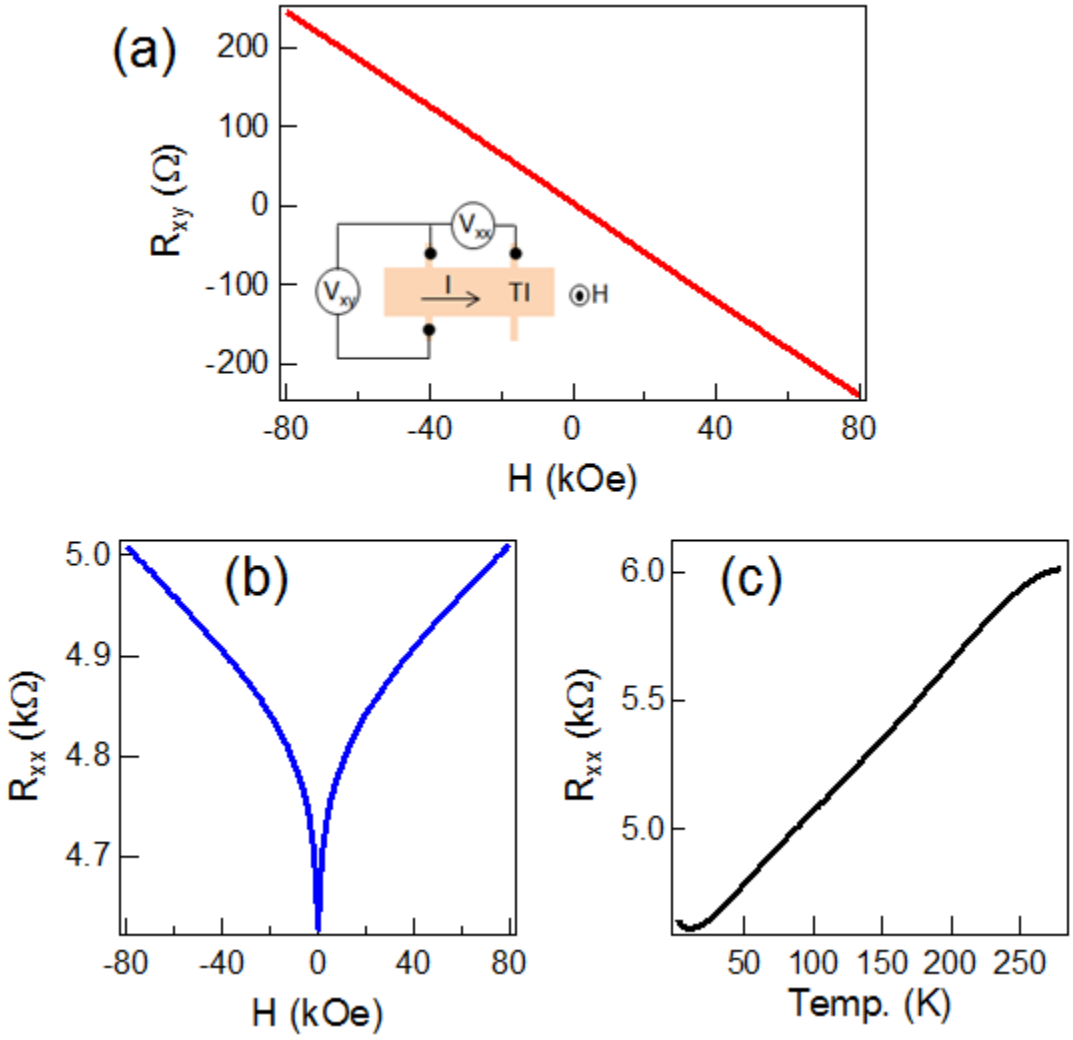

Figure 5-2. Magneto-transport properties of a 10 QL $(Bi,Sb)_2Te_3$ thin film. (a) The result of the Hall measurement at 4.2 K. Inset is a schematic of a Hall-bar geometry and the measurement setup with a magnetic field perpendicular to the plane. (b) Longitudinal magneto-resistance at 4.2K. (c) Longitudinal resistance as a function of temperature.

Device fabrication

Lateral spin transport devices with a magnetic tunnel junction of Py/Al_2O_3 on a cross-shaped $(Bi,Sb)_2Te_3$ channel were prepared. A 1.6-2.1 nm-thick Al_2O_3 tunnel barrier was inserted between the e-beam-evaporated Py layer and TI film in order to overcome the conductivity

mismatch between the two layers. As shown in the atomic force microscopy (AFM) image in Figure 5-1(b), surfaces of MBE-grown TI films have 1-nm steps of a unit layer (quintuple layer) of chalcogenide TIs, which require conformal deposition of an insulating layer to prevent a current leaking through sidewalls of the steps. We used Al_2O_3 by atomic layer deposition (ALD) for the conformal deposition, and we found that a smoother surface was obtained with an Al_2O_3 seed layer (0.3 nm) by RF sputtering prior to the ALD deposition of the Al_2O_3 layer. The surface morphologies of Al_2O_3 on a Bi_2Se_3 film with or without a seed layer are compared by AFM images and the height profiles, as shown in Figure 5-3. A slightly non-linear I vs V characteristic was observed with a three-terminal geometry at 4.2 K while only a linear behavior was seen at 300 K (Figure 5-4).

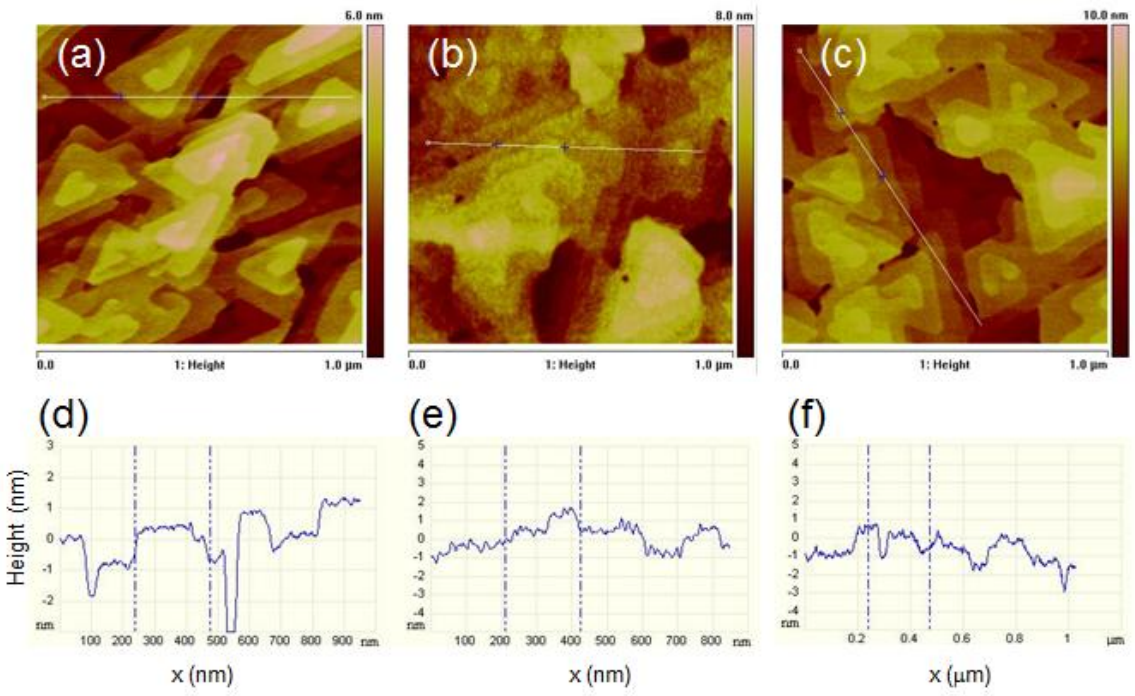

Figure 5-3. AFM images of (a) bare Bi2Se3, (2) 1.5nm Al_2O_3 by ALD on Bi_2Se_3 and (c) 1.5 nm Al_2O_3 by ALD on a 0.3 nm Al_2O_3 seed layer by sputtering on Bi_2Se_3. Height profiles for each white line in the AFM images are plotted in (d), (e), and (f), respectively.

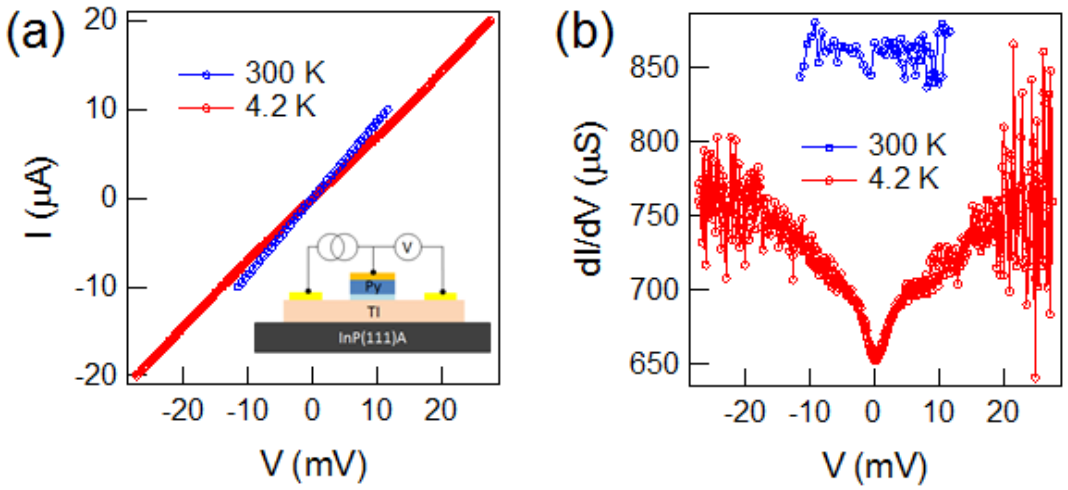

Figure 5-4. Characterization of a Py/Al2O3 tunnel junction on a TI channel. (a) DC current as a function of DC voltage at 300 K and 4.2 K. Inset shows a three-terminal measurement setup. (b) AC differential conductance (dI/dV) as a function of DC voltage.

To restrict the detection of spin signals from a TI top surface only, the magnetic tunnel junction was fabricated on a section of a bare $(Bi,Sb)_2Te_3$ surface while the nearby surface was covered by an insulating layer of 60 nm Si_3N_4, as illustrated in Figures 5-5(a) and (b). The tunnel junction is used as a spin detector when a DC current flows through TI. An in-plane magnetic field perpendicular to the current direction is applied to align the Py magnetization parallel to the direction of the spin-polarization of the TI surface state, which is perpendicular to the current direction [Figure 5-5(e)]. With flipping the direction of Py magnetization parallel or anti-parallel to the spin direction [Figure 5-5(c)], we observed hysteretic spin signals at the magnetic switching field (~30 Oe) of the ferromagnet Py (Figure 5-6).

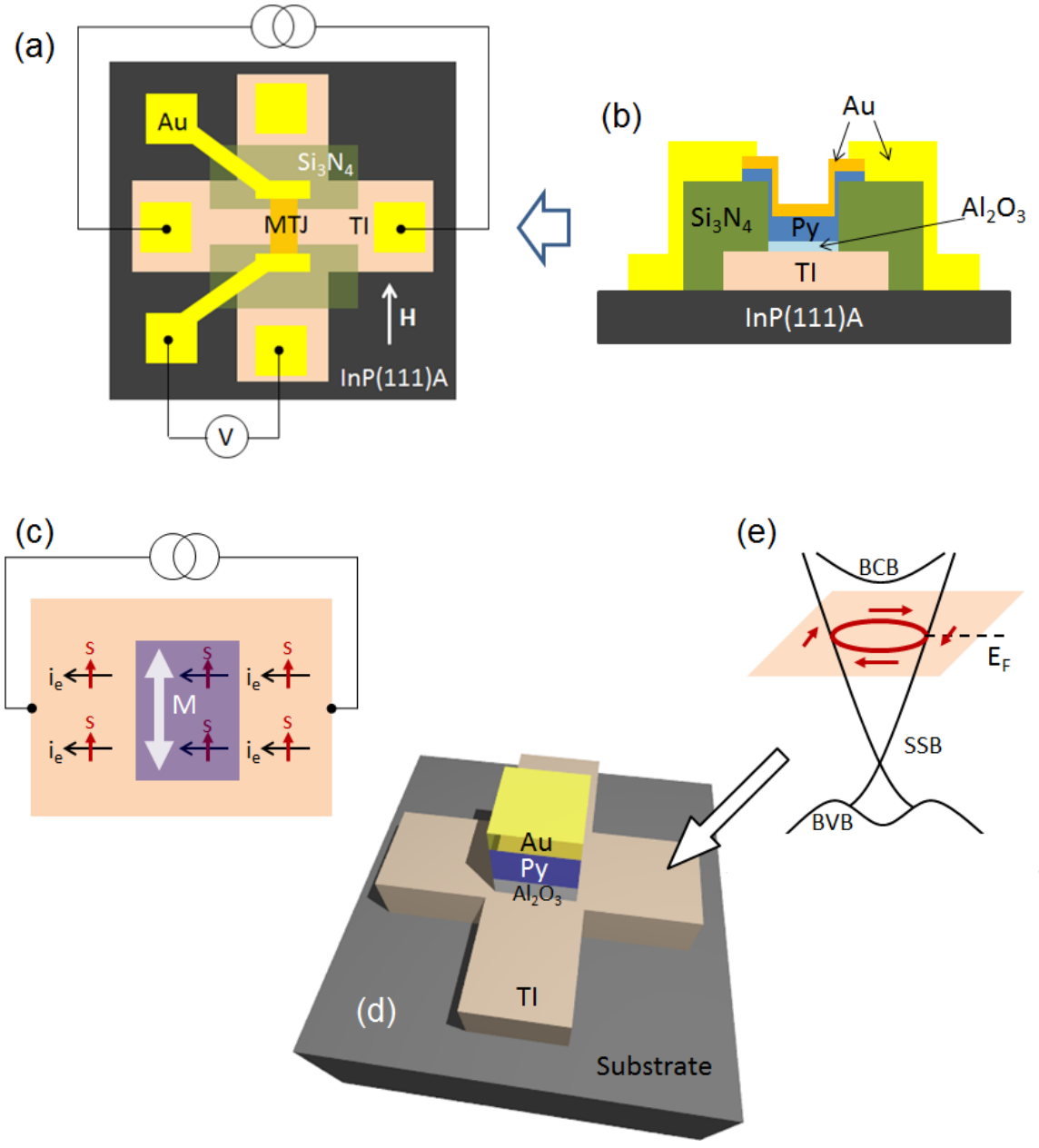

Figure 5-5. (a) A schematic of a device of a Py/Al_2O_3 junction on a TI channel with a measurement setup for detecting TI spin polarization. (b) A side view of the device schematic. (c) An illustration of the direction of the TI spin polarization (red arrows) with an electron current (black arrows) flowing to the left. The direction of the magnetization of Py (white arrow) is aligned parallel or anti-parallel to the direction of spin polarization for detection. (d) A device schematic in 3D. (e) A cartoon of the band diagram of $(Bi,Sb)_2Te_3$ film with Fermi energy E_F placed below the bottom of the bulk conduction band (BCB). Spin directions are depicted as red arrows.

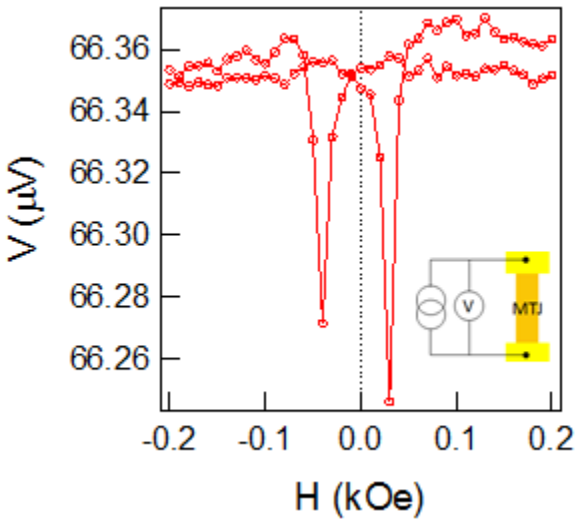

Figure 5-6. Anisotropic magnetoresistance of a Py contact with a dimension of 40 × 80 μm^2, measured at 4.2 K. The coercive field is around 30 Oe. Inset is a schematic of a two-terminal measurement setup.

Results and discussions

Figures 5-7(a-e) show the hysteretic behavior of the detected voltage from the measurement setup shown in Figure 5-5. As a magnetic field is swept from a negative value, far beyond the saturation field of the Py layer, to a positive value, the detected voltage jumps down (up) at the coercive field of the Py layer for positive (negative) currents, with the direction of the electron propagation to the left (right). The changed voltage with positive magnetization $[V(\vec{M})]$, along the direction of the positive magnetic field, recovers back to the original values $[V(-\vec{M})]$ with a down-sweep, resulting in a hysteresis near zero magnetic field. The change in the detected voltage and the resulting hysteresis can be interpreted in terms of the interaction between the spin-polarized current on the TI top surface and the magnetization of the Py layer through the Al_2O_3 tunnel barrier.

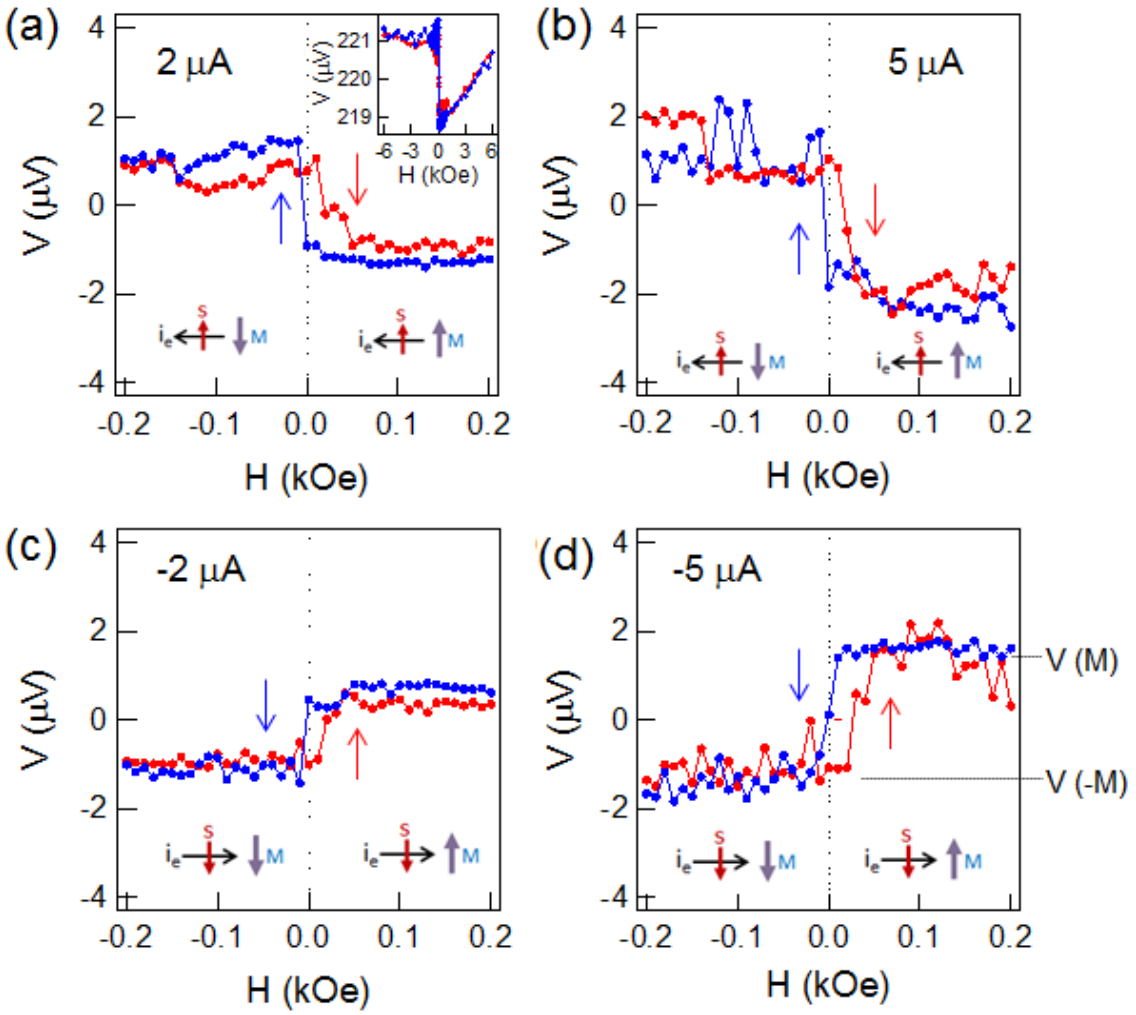

Figure 5-7. Detected voltage with respect to the magnetic field up-sweep (red) and down-sweep (blue) for different DC currents of (a) 2 A, (b) 5 A, (c) -2 A, and (d) -5 A. Each plot is offsetted except the inset to (a), which is a wider-field-ranged plot of (a). All the measurements were carried out at 4.2 K. Relative directions of an electron current on TI top surface (black), current-induced spin polarization (red), and the magnetization of Py (cyan) are illustrated as the insets to each plot.

For a given current, the direction of spin polarization is determined by the helical spin texture of the TI surface state according to the direction of the current. With a magnetic field sweep, the magnetization of a ferromagnet flips, while the direction of the spin polarization is unchanged. In the case of positive currents [Figures 5-7(a) and (b)], the Py magnetization flips from antiparallel to parallel states relative to the spin direction with a magnetic field up-sweep, resulting in the negative change in the detected voltage $\left[V\left(\vec{M}\right) - V\left(-\vec{M}\right)\right]$. On the other hand, for negative currents [Figures 5-7(c) and (d)], the change in the detected voltage $\left[V\left(\vec{M}\right) - V\left(-\vec{M}\right)\right]$ is positive. These results support the interpretation of detection of spin polarization with respect to the direction of the Py magnetization. In case of negative currents, the direction of the spin polarization is opposite to the case of the positive currents. In other words, the relative direction of the Py magnetization to the spin direction is from the parallel state to the anti-parallel state with a magnetic field up-sweep. The theoretical proposal [33] of the three-terminal potentiometric with an FM electrode predicted that the detected voltage is proportional to the projection of the spin polarization onto the detector FM magnetization. The voltage change when reversing the FM magnetization is directly related to the current-induced spin polarization of a TI channel. The calculated voltage change is given by

$$\left[V\left(\vec{M}\right) - V\left(-\vec{M}\right)\right]/I = R_B(\vec{p} \cdot \vec{m}), \tag{5.1}$$

where R_B, $\vec{p}$, and $\vec{m}$ represent ballistic resistance, degree of the spin polarization per unit current in the TI channel, and effective magnetic polarization, respectively. Although our measurements were conducted in the diffusive regime, the linear relation of the voltage change as a function of current (Figure 5-8) can be qualitatively explained by Equation (5.1).

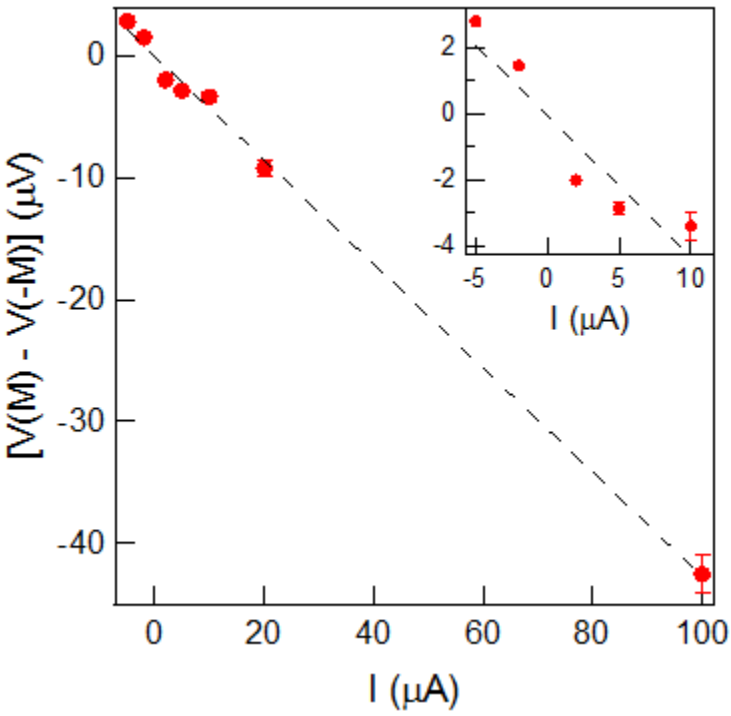

Figure 5-8. The change in voltage $[V(\vec{M}) - V(-\vec{M})]$ as a function of current. Linear t to the data points is depicted as a black dotted line. The inset is a zoomed-in plot of the blue-circled area. The error bars represent the standard deviations for the change in voltage over multiple measurements.

Conclusions and future directions

In conclusion, we have carried out electrical measurements of spin polarization inherently induced by a current through a 3D TI thin film, using a Py/Al_2O_3 magnetic tunnel junction as a spin detector. The MBE-grown 3D TI $(Bi,Sb)_2Te_3$ films were engineered to have the chemical potential in the surface state (below the bottom of the conduction band) by adjusting Bi and Sb composition to ~1:1, so that the top surface, interfacing the magnetic tunnel junction, is decoupled from the bottom surface by insulating bulk. We observed hysteretic behaviors of the detected voltage as a function of an in-plane magnetic field, perpendicular to the direction of current, in order to align the Py magnetization parallel to the TI spin polarization. We interpret

our results as the detection of the current-induced spin polarization of TI by means of the magnetization switching of the ferromagnetic layer in the magnetic tunnel junction. As speculated, our results with a TI film of which the chemical potential is placed between the conduction band and the Dirac point reveal a larger spin signal (the change in the detected voltage) with about two orders of magnitude lower current density through the TI layer in comparison with the recently reported experimental results [34].

Tuning the chemical potential across the bulk band gap by electrical gating may lead to further evidence of the electrical detection of the helically spin-polarized TI surface state. It is expected that larger spin signals would be observed with lower current density as the position of the chemical potential moves towards the Dirac point. For this study, we have successfully carried out back-gating through $SrTiO_3$ substrates to observe the ambipolar transport in TI films. The details are provided in Appendix B. Fabrications of magnetic tunnel junctions on a back-gated device and the electrical measurements of spin signals are in progress. In addition, the electrical detection of the TI spin-polarization at higher temperatures will be necessary for the potential spintronics applications.

Appendix A

Details of device fabrication process

Fabrication of various devices for this dissertation research has been carried out in the Nanofabrication Lab at The Pennsylvania State University utilizing photo and electron-beam lithography, wet and dry etching, and depositions of metal and oxide layers. In this appendix, fabrication steps of Hall bars (discussed in Chapter 3), top-gated Hall-bar devices (discussed in Chapter 4), and magnetic tunnel junctions on TI channels (discussed in Chapter 5) will be described in detail.

Fabrication steps of Hall bars

The first step of the fabrication is to prepare a photomask for photolithography. Patterns of Hall-bar geometries were designed using a computer-aided design software (L-edit). The designed patterns were defined on a Cr-coated blank mask by a Heidelberg DLW66 laser writer, and the resulting Cr layer unprotected by photoresist was wet-etched. Using the prepared photomask, Hall bars with usual channel dimensions of 400 μm in width and 650 μm in length were fabricated by photolithography and wet/dry etching. The procedure for fabrication of a TI Hall bar is provided as follows:

1. Dehydrate the sample at 110°C for 1-2 minutes on a hot plate.
2. Apply photoresist (AZ ECI 3012 or Shipley 1813) on the sample and spin at 5000 rpm for 45 seconds.
3. Bake the sample at 110°C for 90 seconds and cool down to room temperature.

4. Place the sample on a mask aligner (Karl Suss MA/BA6) and align it with a desired pattern using a microscope.
5. Expose with UV light (365 nm wavelength) at a power of 8 mW for 8 seconds.
6. Develop the exposed sample in MF CD-26 for 60 seconds, rinse it with deionized (DI) water, and dry with N_2 gas.
7. Etch the bared part of the TI film by Ar plasma milling. The typical condition used by a Tegal 6540 plasma etcher is a power of 100 W with 40 sccm Ar flow, resulting in an etch rate of ~0.5 nm/sec for Bi_2Se_3 etching. For wet-etching, use hydrobromic acid-based etchant [2g potassium dichromate (K2Cr2O7) powder, 174.5 mL HBr, and 500 mL DI water] with a typical etch rate of ~1 nm/s.
8. Remove photoresist with acetone, and rinse with isopropanol (IPA). If necessary, sonicate in acetone for a few seconds.

Fabrication steps of top-gated Hall-bar devices

In Chapter 4, top-gated Hall-bar devices were used for magneto-transport measurements to study the resulting effects of the broken TR symmetry in the surface state as the chemical potential is tuned by top-gating. The procedure of a Hall-bar fabrication is almost the same as described above. The additional steps are an evaporation of a thin HfO_2 layer before the Hall-bar fabrication, a photolithography process for bilayer photoresist on the Hall bar of a TI/(Ga,Mn)As heterostructure, and HfO_2/Au deposition for top-gating. The general procedure is as follows:

1. Evaporate (e-beam) 3 nm HfO_2 on top of the TI layer. The HfO_2 layer is intended to protect the TI surface from degradation during the fabrication process and to function as a seed layer for ALD HfO_2 deposition.

2. Perform photolithography processes (from step 1 to step 5 as described in the previous section) to define a Hall-bar geometry.
3. Etch the TI/(Ga,Mn)As heterostructure using Ar plasma milling. To etch TI and (Ga,Mn)As layers together, a longer etch time of about 5 minutes is needed for 100 W power. Note that the etch rate of a (Ga,Mn)As layer is slower than that of TI film.
4. Perform photolithography processes for the bilayer photoresist to deposit the gating dielectric HfO_2 and gating metal Au.
    a. Spin LOR 2A on the sample at 5000 rpm for 45 seconds.
    b. Bake the sample at 175°C for 3 minutes and cool down to room temperature.
    c. Spin AZ ECI 3012 (or Shipley 1813) on the sample at 5000 rpm for 45 seconds.
    d. Bake the sample at 110°C for 90 seconds and cool down to room temperature.
    e. Expose with UV light for 8 seconds.
    f. Develop in MF CD-26 for 60 seconds, rinse with DI water, and dry with N_2 gas.
5. Clean the surface softly, using low-power Ar plasma to remove possible photoresist residues and native oxide prior to the ALD HfO_2 deposition. Ar plasma at 15 W for 20 seconds was typically used in the Tegal 6540 plasma etcher.
6. Deposit 20-30 nm HfO_2 at 110°C by ALD (Kurt J. Lesker ALD150LE or Cambridge Savannah 200).
7. Deposit 5 nm Ti (or Cr) as an adhesion layer and 40 nm Au by e-beam evaporation (Kurt J. Lesker Lab-18 E-Gun & Thermal Evaporator).
8. Lift off the HfO_2/Ti/Au layers by removing the bilayer photoresist with acetone and/or photoresist stripper (Remover PG). May heat up the Remover PG at 65°C or use sonicator if necessary.

Fabrication steps of magnetic tunnel junctions on TI channels

Electrical spin signals detected by a magnetic tunnel junction on a TI channel are not much bigger than the background noise. Therefore, it is important to fabricate clean interfaces of tunnel junctions and other contacts on TI channels. TI surfaces were carefully cleaned by low-power Ar plasma before any deposition of oxides or metals.

1. Perform photolithography processes for the bilayer photoresist (from step 4 as described in the previous section) to define Au contacts on TI.
2. Clean the bared TI surface softly using low-power Ar plasma for the Ti/Au contact deposition. Ar plasma at 15 W for 20 seconds was used in the Tegal 6540 plasma etcher.
3. Deposit 5 nm Ti and 40 nm Au by e-beam evaporation (Lab-18 Evaporator).
4. Lift off the Ti/Au layers by removing the bilayer photoresist with acetone and/or Remover PG.
5. Perform photolithography processes to define a cross-shaped TI channel.
6. Etch the bared part of the TI layer by Ar plasma milling in the Tegal 6540 plasma etcher. Ar plasma of 100 W was used for 40 seconds with 40 sccm flow.
7. Remove photoresist with acetone.
8. Perform photolithography processes for bilayer photoresist to define an insulating layer of Si_3N_4.
9. Deposit a ~60 nm Si_3N_4 layer by plasma-enhanced chemical vapor deposition (Applied Materials P-5000 OECVD Cluster Tool) at a substrate temperature of 150°C.
10. Lift off the Si_3N_4 layers by removing the bilayer photoresist with acetone and/or Remover PG.

11. Perform photolithography processes for the bilayer photoresist to define magnetic tunnel junctions in the middle of TI channels.
12. Clean the bared TI surface softly using low-power Ar plasma in a sputtering tool (Kurt J. Lesker CMS-18 Sputter). Ar plasma at 15 W was used for 20 seconds.
13. Right after the Ar plasma cleaning, deposit a seed layer of ~3 Å Al_2O_3 in the sputter chamber. For the Al_2O_3 deposition, an Al target was sputtered under an Ar and O_2 environment (O_2 15%).
14. Move the sample to an ALD tool as soon as possible. Deposit 1.3-1.8 nm Al_2O_3 at 110°C by ALD (Kurt J. Lesker ALD150LE or Cambridge Savannah 200).
15. Deposit ~20 nm Py and a thin Au capping (2-5 nm) layer by e-beam evaporation (Lab-18 Evaporator).
16. Lift off the Al_2O_3/Py/Au layers by removing the bilayer photoresist with acetone and/or Remover PG.
17. Perform photolithography processes for bilayer photoresist to define Ti/Au contact pads connected to the magnetic tunnel junctions.
18. Deposit 5 nm Ti and 40 nm Au by e-beam evaporation (Lab-18 Evaporator).
19. Lift off the Ti/Au layers by removing the bilayer photoresist with acetone and/or Remover PG.
20. (Optional) Perform photolithography processes to cover the magnetic tunnel junction and the bared TI surface to protect them from further oxidation or degradation caused by air exposure.

The fabrication procedure of the magnetic tunnel junctions on TI channels is schematically illustrated in Figure A-1(a), and optical microscope images of the devices are shown in Figure A-1(b).

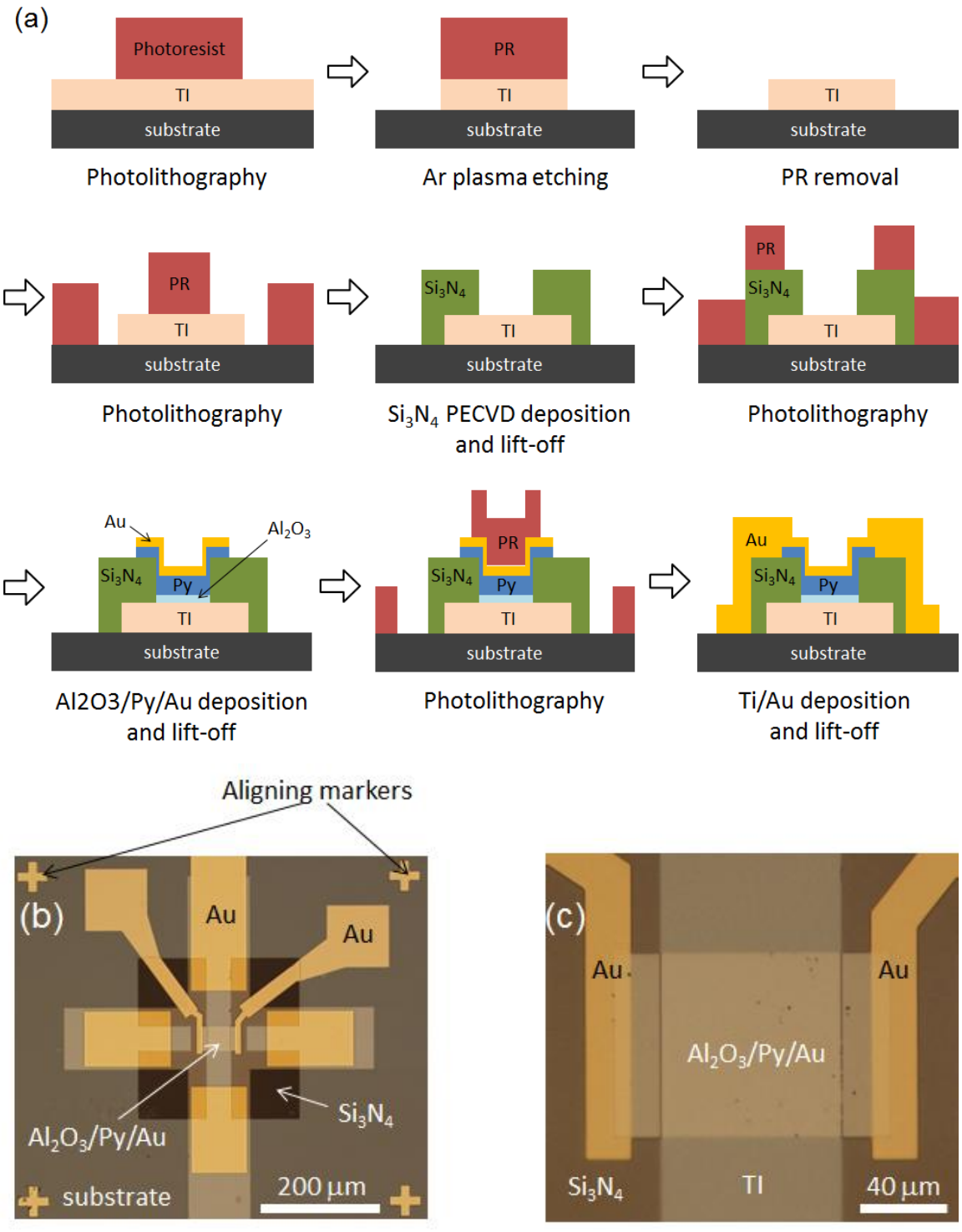

Figure A-1. (a) Illustrative schematics of the fabrication process for a magnetic tunnel junction device on a TI channel. (b,c) Optical microscope images of a fabricated device with different magnifications.

Appendix B

Ambipolar transport in TI by back-gating

In Chapter 5, electrical gating to tune the chemical potential across the bulk band gap of TI was proposed to further evidence the helical TI surface states and to observe larger spin signals from the spin-polarization in the TI surface. In this appendix, I'll describe the details of the sample preparation and the results of the ambipolar transport of TI thin films by back-gating through $SrTiO_3$ substrates.

Synthesis of TI thin films on $SrTiO_3$ by MBE

In order to rule out the contribution of bulk conduction in a 3D TI, one needs to place the chemical potential into the bulk band gap. Plain, MBE-grown Bi_2Te_3 thin films show the n-type conduction while Sb_2Te_3 thin films reveal the p-type conduction [100]. With an optimal Bi:Sb ratio, 3D TI $(Bi,Sb)_2Te_3$ thin films with the chemical potential placed in the bulk band gap were grown on $SrTiO_3$ substrates by MBE. The thickness of the thin films was kept in a range of 8-10 QLs for further control of the chemical potential by back-gating. High-κ dielectric $SrTiO_3$(111) substrates were prepared by annealing under an oxygen gas environment. Figure B-1 shows the surface morphology of an $SrTiO_3$(111) substrate by AFM after annealing at 900-960°C under an oxygen environment for 2 hours. Flat terraces with small steps of ~2 Å are typically observed after the annealing.

For an MBE growth of a $(Bi,Sb)_2Te_3$ film, the annealed $SrTiO_3$(111) substrate was transferred to the II-VI chamber, heated up to a thermo-couple temperature of 500°C for

desorption, and then cooled down to a growth temperature of 310-325°C. A $(Bi,Sb)_2Te_3$ film was grown with the beam-equivalent pressure ratios of Te:(Bi+Sb) and Sb:(Sb+Bi) as ~6 and ~0.6, respectively, and with the growth rate of ~1.5 QL/min.

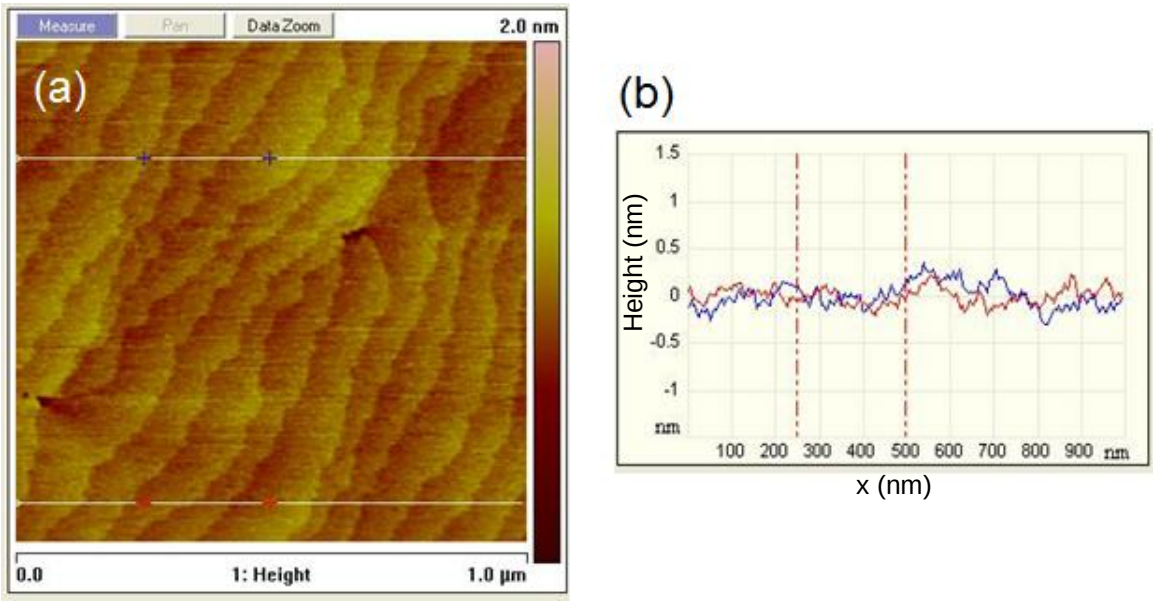

Figure B-1. (a) An AFM image of an annealed $SrTiO_3$ substrate. A white, horizontal line with blue (red) crosses represents cross-sectional line cut which is plotted in blue (red) in (b) the height profile.

Ambipolar transport of TI

The position of the chemical potential in a $(Bi,Sb)_2Te_3$ film was estimated by carrier densities obtained by Hall effect measurements, which were carried out by driving a current through a Hall-bar geometry of 650 × 400 μm^2 channel dimensions and measuring a transverse voltage with a perpendicular magnetic field [Figure B-2(a)]. The Hall bar was fabricated by a conventional photolithography as described in Appendix A.

Low bulk conduction by the given Bi:Sb ratio enables further electrical tuning of the chemical potential through the Dirac point in the TI surface state. A gate voltage was applied to a ~8 QL $(Bi,Sb)_2Te_3$ thin film through a ~500-μm-thick high-κ dielectric $SrTiO_3$ substrate.

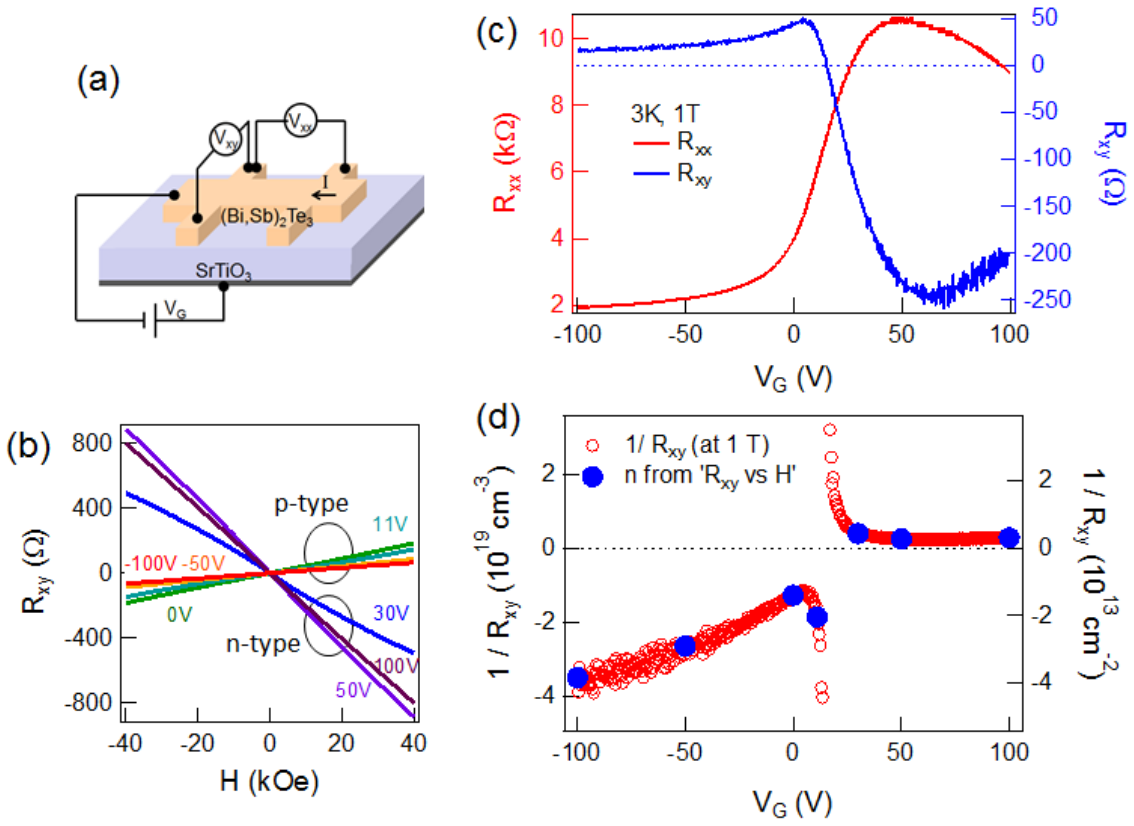

Figure B-2. Ambipolar transport of a $(Bi,Sb)_2Te_3$ film with back-gating through $SrTiO_3$ substrate. (a) An illustration of a $(Bi,Sb)_2Te_3$ Hall-bar geometry on $SrTiO_3$ substrate with a measurement setup of longitudinal (V_{xx}) and transverse (V_{xy}) voltages with a gate voltage (V_G). (b) Transverse resistance R_{xy} with perpendicular magnetic field sweep at gate voltages of 100 V (purple), 50 V (violet), 30 V (blue), 11 V (cyan), 0 V (green), -50 V (orange), and -100 V (red). (c) Gate-voltage dependence of the longitudinal resistance R_{xx} (red, left axis) and the Hall resistance R_{xy} (blue, right axis) with a perpendicular magnetic field of 1 T applied. (d) Gate-voltage dependence of the inverse of the Hall resistance $1/R_{xy}$ (red circles) in the unit of 3D (left axis) and 2D (right axis) carrier concentrations. Blue solid circles represent the carrier concentrations calculated from the Hall measurement curves with different gate voltages in (b). All data were measured at 3 K.

Figure B-2(b) shows a sign change in the slopes of the Hall resistance R_{xy} as a function of a magnetic field with different gate voltages from 100 V to -100 V, interpreted as an electrical carrier type change from n type to p type as the chemical potential is tuned from a position above the Dirac point (n-type carrier) to a position below the Dirac point (p-type carrier). The sign change in R_{xy} is more clearly seen in the gate-voltage dependence of R_{xy} with a perpendicular magnetic field fixed to 1 T [Figure B-2(c)]. As the gate voltage sweeps from 100 V to -100 V, negative R_{xy} (n-type carrier) reaches its minimum at 60 V and zero at 15 V, and then R_{xy} becomes positive (p-type carrier), reaches its maximum at 5 V and decreases slowly. Near the charge neutrality point at 15 V, where $R_{xy} = 0$, the number of n-type carriers and the number of p-type carriers in the TI film are comparable. From the gate-voltage dependence of R_{xx} [Figure B-2(c)], we see the maximum at around 50 V. The mismatch of the gate voltage of the charge neutrality point and the gate voltage of R_{xx} maximum indicates that the carrier densities of top and bottom surfaces are not the same at a given gate voltage, which is typically observed with electrical gating of TI films since the distance of one surface from the gate-metal is slightly different from that of another surface due to the finite thickness of the TI film. Also, band bending at the surface of a TI film [101] can be another reason for the carrier-density difference.

Additional information on charge conduction of bulk and surface states is provided by an analysis of magnetoresistance. In Figure B-3(a), longitudinal resistance R_{xx} as a function of a magnetic field shows negative magnetoresistance for all the gate voltages. The sharp cusps near zero magnetic field are the WAL quantum corrections to the classical magnetoresistance and can be analyzed by the theory of WAL [87]. Fits by the HLN Equation (4.1) give values of the prefactor α and the coherence length l_{ϕ}.

In 3D TI thin films, as discussed in Chapter 4, WAL corrections are expected due to the π Berry phase of electrons in the Dirac surface state [88]. We discussed that the prefactor α

depends on the position of the chemical potential and the coupling between the top and bottom surfaces by the bulk conduction. When the top and bottom surfaces are coupled by conducting bulk carriers, the prefactor α is -1/2, but as the two surfaces are decoupled by placing the chemical potential into the bulk band gap, α becomes -1 [89, 90]. In Figure B-3(b), α shows the two stages of values of -1/2 and -1. From $V_G = 100$ V down to 30 V, α stays near -0.9 (close to -1), it changes to -1/2 as V_G lowers below 30 V. From the results, we learn that the top and bottom surfaces are mostly decoupled in the V_G range from 100 V to 30 V, and then they start to be coupled by the conducting bulk. As we know from the Hall measurements, the conducting bulk carriers at lower gate voltages are p-type carriers from the valence band.

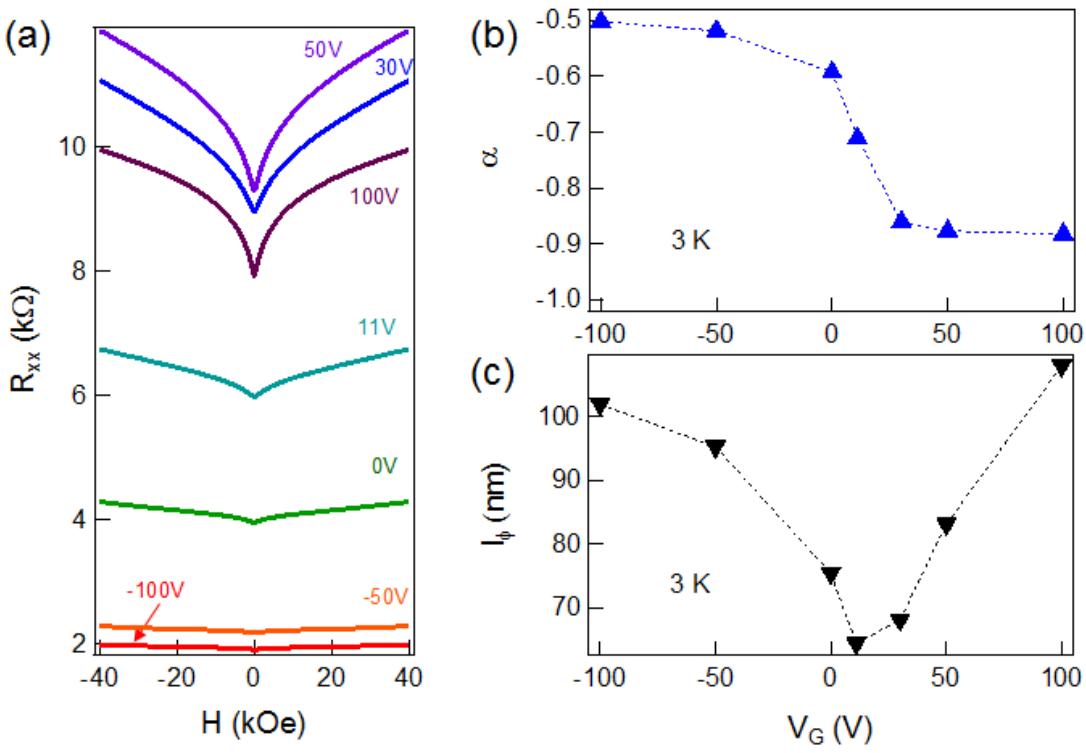

Figure B-3. (a) Longitudinal resistance R_{xx} as a function of a perpendicular magnetic field at different gate voltages measured together with transverse resistance. Gate-voltage dependence of (a) the prefactor α and (b) the coherence length l_ϕ obtained by fitting the magnetoresistance curves in (a) by the HLN Equation (4.1). All data were taken at 3 K.

In summary, we have successfully synthesized TI thin films on $SrTiO_3$ substrates and demonstrated electrical back gating through a $SrTiO_3$ substrate. Hall measurements reveal the ambipolar transport in a TI film by showing the change of charge carrier types with different gate voltages as well as the change in the longitudinal resistance. The analysis of magnetoresistance with respect to the gate voltage confirms that the chemical potential of the TI film is tuned from a position in the surface state with suppressed bulk carriers to a position in the valence band with conducting p-type bulk carriers.

Bibliography

[1] M. Z. Hasan and C. L. Kane, *Rev. Mod. Phys.* **82**, 3045 (2010).

[2] X.-L. Qi and S.-C. Zhang, *Physics Today* **63**, 33 (2010).

[3] J. E. Moore, *Nature* **464**, 194 (2010).

[4] V. Mourik, K. Zuo, S. M. Frolov, S. R. Plissard, E. P. A. M. Bakkers, and L. P. Kouwenhoven, *Science* **336**, 1003 (2012).

[5] D. Pesin and A. H. MacDonald, *Nature Materials* **11**, 409 (2012).

[6] K. Klitzing, G. Dorda, and M. Pepper, *Phys. Rev. Lett.* **45**, 494 (1980).

[7] D. Thouless, M. Kohmoto, M. Nightingale, and M. den Nijs, *Phys. Rev. Lett.* **49**, 405 (1982).

[8] B. A. Bernevig, T. L. Hughes, and S.-C. Zhang, *Science* **314**, 1757 (2006).

[9] M. Konig, S. Wiedmann, C. Brune, A. Roth, H. Buhmann, L. W. Molenkamp, X.-L. Qi, and S.-C. Zhang, *Science* **318**, 766 (2007).

[10] L. Fu and C. Kane, *Phys. Rev. B* **76**, 045320 (2007).

[11] D. Hsieh, D. Qian, L. Wray, Y. Xia, Y. S. Hor, R. J. Cava, and M. Z. Hasan, *Nature* **452**, 970 (2008).

[12] C. L. Kane and E. J. Mele, *Phys. Rev. Lett.* **95**, 226801(2005).

[13] K. S. Novoselov, *Science* **306**, 666 (2004).

[14] L. Fu, C. L. Kane, and E. J. Mele, *Phys. Rev. Lett.* **98**, 106803 (2007).

[15] J. Moore and L. Balents, *Phys. Rev. B* **75**, 121306 (2007).

[16] R. Roy, *Phys. Rev. B* **79**, 195322 (2009).

[17] H. Zhang, C.-X. Liu, X.-L. Qi, X. Dai, Z. Fang, and S.-C. Zhang, *Nature Physics* **5**, 438 (2009).

[18] Y. Xia, D. Qian, D. Hsieh, L. Wray, A. Pal, H. Lin, A. Bansil, D. Grauer, Y. S. Hor, R. J. Cava, *et al.*, *Nature Physics* **5**, 398 (2009).

[19] D. Hsieh, Y. Xia, L. Wray, D. Qian, A. Pal, J. H. Dil, J. Osterwalder, F. Meier, G. Bihlmayer, C. L. Kane, *et al.*, *Science* **323**, 919 (2009).

[20] Y. L. Chen, J. G. Analytis, J.-H. Chu, Z. K. Liu, S.-K. Mo, X. L. Qi, H. J. Zhang, D. H. Lu, X. Dai, Z. Fang, *et al.*, *Science* **325**, 178 (2009).

[21] M. Neupane, A. Richardella, J. Sánchez-Barriga, S. Xu, N. Alidoust, I. Belopolski, C. Liu, G. Bian, D. Zhang, D. Marchenko, *et al.*, *Nature Communications* **5** (2014).

[22] X.-L. Qi, T. L. Hughes, and S.-C. Zhang, *Phys. Rev. B* **78**, 195424 (2008).

[23] I. Garate and M. Franz, *Phys. Rev. Lett* **104**, 146802 (2010).

[24] X.-L. Qi, R. Li, J. Zang, and S.-C. Zhang, *Science* **323**, 1184 (2009).

[25] R. Yu, W. Zhang, H.-J. Zhang, S.-C. Zhang, X. Dai, and Z. Fang, *Science* **329**, 61 (2010).

[26] C.-Z. Chang, J. Zhang, X. Feng, J. Shen, Z. Zhang, M. Guo, K. Li, Y. Ou, P. Wei, L.-L. Wang, *et al.*, *Science* **340**, 167 (2013).

[27] S.-Y. Xu, M. Neupane, C. Liu, D. Zhang, A. Richardella, L. A. Wray, N. Alidoust, M. Leandersson, T. Balasubramanian, J. Sánchez-Barriga, et al., *Nature Physics* **8**, 616 (2012).

[28] J. D. Jackson, *Classical Electrodynamics Third Edition*, Wiley, 1998.

[29] N. Nagaosa, J. Sinova, S. Onoda, A. H. MacDonald, and N. P. Ong, *Rev. Mod. Phys.* **82**, 1539 (2010).

[30] C.-X. Liu, X.-L. Qi, X. Dai, Z. Fang, and S.-C. Zhang, *Phys. Rev. Lett* **101** (2008).

[31] I. Zutic and S. Das Sarma, *Rev. Mod. Phys.* **76**, 323 (2004).

[32] A. A. Burkov and D. G. Hawthorn, *Phys. Rev. Lett* **105**, 066802 (2010).

[33] S. Hong, V. Diep, S. Datta, and Y. P. Chen, *Phys. Rev. B* **86**, 085131 (2012).

[34] C. H. Li, O. M. J. van 't Erve, J. T. Robinson, Y. Liu, L. Li, and B. T. Jonker, *Nature Nanotechnology* **9**, 218 (2014).

[35] J. Slonczewski, *Journal of Magnetism and Magnetic Materials* **159**, L1 (1996).

[36] L. Liu, T. Moriyama, D. C. Ralph, and R. A. Buhrman, *Phys. Rev. Lett* **106** (2011).

[37] I. M. Miron, K. Garello, G. Gaudin, P.-J. Zermatten, M. V. Costache, S. Auffret, S. Bandiera, B. Rodmacq, A. Schuhl, and P. Gambardella, *Nature* **476**, 189 (2011).

[38] L. Liu, C.-F. Pai, Y. Li, H. W. Tseng, D. C. Ralph, and R. A. Buhrman, *Science* **336**, 555 (2012).

[39] S. Emori, U. Bauer, S.-M. Ahn, E. Martinez, and G. S. D. Beach, *Nature Materials* **12**, 611 (2013).

[40] K.-S. Ryu, L. Thomas, S.-H. Yang, and S. Parkin, *Nature Nanotechnology* **8**, 527 (2013).

[41] D. Culcer, E. H. Hwang, T. D. Stanescu, and S. Das Sarma, *Phys. Rev. B* **82** (2010).

[42] A. R. Mellnik, J. S. Lee, A. Richardella, J. L. Grab, P. J. Mintun, M. H. Fischer, A. Vaezi, A. Manchon, E. A. Kim, N. Samarth, and D. C. Ralph, *Nature* 511, 449 (2014).

[43] M. Ohring, *The Materials Science of Thin Films*, Academic Press, 1992.

[44] E. H. Hall, *American Journal of Mathematics* **2**, 287 (1879).

[45] http://www.precisioncryo.com/styled.html.

[46] Oxford Instrument, Scientific Research Division, Witney, England, *Heliox Sorption pumped ^{3}He Insert, Operator's Handbook,*, 1994.

[47] Oxford Instrument, Nanoscience, Oxon, UK, *Triton-^{3}He Refrigerator, Operator's Handbook*, 2010.

[48] D. Zhang, A. Richardella, D. W. Rench, S.-Y. Xu, A. Kandala, T. C. Flanagan, H. Beidenkopf, A. L. Yeats, B. B. Buckley, P. V. Klimov, *et al.*, *Phys. Rev. B* **86**, 205127 (2012).

[49] J. S. Lee, A. Richardella, D. W. Rench, R. D. Fraleigh, T. C. Flanagan, J. A. Borchers, J. Tao, and N. Samarth, *Phys. Rev. B* **89**, 174425 (2014).

[50] Q. Liu, C.-X. Liu, C. Xu, X.-L. Qi, and S.-C. Zhang, *Phys. Rev. Lett.* **102**, 156603 (2009).

[51] Y. L. Chen, J.-H. Chu, J. G. Analytis, Z. K. Liu, K. Igarashi, H.-H. Kuo, X. L. Qi, S. K. Mo, R. G. Moore, D. H. Lu, *et al.*, *Science* **329**, 659 (2010).

[52] L. A. Wray, S.-Y. Xu, Y. Xia, D. Hsieh, A. V. Fedorov, Y. S. Hor, R. J. Cava, A. Bansil, H. Lin, and M. Z. Hasan, *Nature Physics* **7**, 32 (2011).

[53] J. G. Checkelsky, J. Ye, Y. Onose, Y. Iwasa, and Y. Tokura, *Nature Physics* **8**, 729 (2012).

[54] J. S. Dyck, P. Hájek, P. Lošťák, and C. Uher, *Phys. Rev. B* **65**, 115212 (2002).

[55] J. S. Dyck, C. Drašar, P. Lošťák, and C. Uher, *Phys. Rev. B* **71**, 115214 (2005).

[56] J. Choi, H.-W. Lee, B.-S. Kim, S. Choi, J. Choi, J. H. Song, and S. Cho, *J. Appl. Phys.* **97**, 10D324 (2005).

[57] V. Kulbachinskii, A. Kaminskii, K. Kindo, Y. Narumi, K. Suga, P. Lostak, and P. Svanda, *Physica B: Condensed Matter* **311**, 292 (2002).

[58] Y.-J. Chien, *Transition metal-doped Sb2Te3 and Bi2Te3 diluted magnetic semiconductors*, PhD dissertation, The University of Michigan, 2007.

[59] Y. S. Hor, P. Roushan, H. Beidenkopf, J. Seo, D. Qu, J. G. Checkelsky, L. A. Wray, D. Hsieh, Y. Xia, S.-Y. Xu, *et al.*, *Phys. Rev. B* **81**, 195203 (2010).

[60] Y. H. Choi, N. H. Jo, K. J. Lee, J. B. Yoon, C. Y. You, and M. H. Jung, *J. Appl. Phys.* **109**, 070000 (2011).

[61] L. Bao, W. Wang, N. Meyer, Y. Liu, C. Zhang, K. Wang, P. Ai, and F. Xiu, *Scientific Reports* **3**, 2 (2013).

[62] P. P. J. Haazen, J.-B. Laloe, T. J. Nummy, H. J. M. Swagten, P. Jarillo-Herrero, D. Heiman, and J. S. Moodera, *Appl. Phys. Lett.* **100**, 082404 (2012).

[63] J. Zhang, C.-Z. Chang, P. Tang, Z. Zhang, X. Feng, K. Li, L.-l. Wang, X. Chen, C. Liu, W. Duan, *et al.*, *Science* **339**, 1582 (2013).

[64] C.-Z. Chang, J. Zhang, M. Liu, Z. Zhang, X. Feng, K. Li, L.-L. Wang, X. Chen, X. Dai, Z. Fang, *et al.*, *Advanced Materials* **25**, 1065 (2013).

[65] H. J. von Bardeleben, J. L. Cantin, D. M. Zhang, A. Richardella, D. W. Rench, N. Samarth, and J. A. Borchers, *Phys. Rev. B* **88**, 075149 (2013).

[66] J. W. G. Bos, M. Lee, E. Morosan, H. W. Zandbergen, W. L. Lee, N. P. Ong, and R. J. Cava, *Phys. Rev. B* **74**, 184429 (2006).

[67] T. Valla, H. Ji, L. M. Schoop, A. P. Weber, Z.-H. Pan, J. T. Sadowski, E. Vescovo, A. V. Fedorov, A. N. Caruso, Q. D. Gibson, *et al.*, *Phys. Rev. B* **86**, 241101 (2012).

[68] P. A. Kienzle, J. Krycka, N. Patel, and I. Sahin, REFL1D (Version 0.6.19) [Computer Software], 2011.

[69] B. C. Chapler, K. W. Post, A. R. Richardella, J. S. Lee, J. Tao, N. Samarth, and D. N. Basov, *Phys. Rev. B* **89**, 235308 (2014).

[70] R. C. O'Handley, *Modern Magnetic Materials: Principles and Applications*, Wiley-Interscience, 1999.

[71] J. Wang, H. Li, C. Chang, K. He, J. S. Lee, H. Lu, Y. Sun, X. Ma, N. Samarth, S. Shen, and *et al*., *Nano Research* **5**, 739 (2012).

[72] A. H. MacDonald, P. Schiffer, and N. Samarth, *Nature Materials* **4**, 195 (2005).

[73] T. Dietl, *Nature Materials* **9**, 965 (2010).

[74] D. A. Abanin and D. A. Pesin, *Phys. Rev. Lett.* **106**, 136802 (2011).

[75] Y. Okada, C. Dhital, W. Zhou, E. D. Huemiller, H. Lin, S. Basak, A. Bansil, Y.-B. Huang, H. Ding, Z. Wang, *et al.*, *Phys. Rev. Lett* **106**, 206805 (2011).

[76] D. West, Y. Y. Sun, S. B. Zhang, T. Zhang, X. Ma, P. Cheng, Y. Y. Zhang, X. Chen, J. F. Jia, and Q. K. Xue, *Phys. Rev. B* **85**, 081305 (2012).

[77] Y. R. Song, F. Yang, M.-Y. Yao, F. Zhu, L. Miao, J.-P. Xu, M.-X. Wang, H. Li, X. Yao, F. Ji, *et al.*, *Appl. Phys. Lett.* **100**, 242403 (2012).

[78] C.-Z. Chang, P. Tang, Y.-L. Wang, X. Feng, K. Li, Z. Zhang, Y. Wang, L.-L. Wang, X. Chen, C. Liu, *et al.*, *Phys. Rev. Lett* **112**, 056801 (2014).

[79] P. Wei, F. Katmis, B. A. Assaf, H. Steinberg, P. Jarillo-Herrero, D. Heiman, and J. S. Moodera, *Phys. Rev. Lett* **110**, 186807 (2013).

[80] Q. I. Yang, M. Dolev, L. Zhang, J. Zhao, A. D. Fried, E. Schemm, M. Liu, A. Palevski, A. F. Marshall, S. H. Risbud, *et al.*, *Phys. Rev. B* **88**, 081407 (2013).

[81] A. Kandala, A. Richardella, D. W. Rench, D. M. Zhang, T. C. Flanagan, and N. Samarth, *Appl. Phys. Lett.* **103**, 202409 (2013).

[82] M. Lang, M. Montazeri, M. C. Onbasli, X. Kou, Y. Fan, P. Upadhyaya, K. Yao, F. Liu, Y. Jiang, W. Jiang, *et al.*, *Nano Lett.* **14**, 3459 (2014).

[83] K. C. Ku, S. J. Potashnik, R. F. Wang, S. H. Chun, P. Schiffer, N. Samarth, M. J. Seong, A. Mascarenhas, E. Johnston-Halperin, R. C. Myers, *et al.*, *Appl. Phys. Lett.* **82**, 2302 (2003).

[84] F. Matsukura, M. Sawicki, T. Dietl, D. Chiba, and H. Ohno, *Physica E: Low-dimensional Systems and Nanostructures* **21**, 1032 (2004).

[85] A. Richardella, D. M. Zhang, J. S. Lee, A. Koser, D. W. Rench, A. L. Yeats, B. B. Buckley, D. D. Awschalom, and N. Samarth, *Appl. Phys. Lett.* **97**, 262104 (2010).

[86] H. Suzuura and T. Ando, *Phys. Rev. Lett* **89**, 266603 (2002).

[87] S. Hikami, A. I. Larkin, and Y. Nagaoka, *Progress of Theoretical Physics* **63**, 707 (1980).

[88] D. Hsieh, Y. Xia, D. Qian, L. Wray, J. Dil, F. Meier, J. Osterwalder, L. Patthey, J. Checkelsky, N. Ong, *et al.*, *Nature* **460**, 1101 (2009).

[89] I. Garate and L. Glazman, *Physical Review B* **86**, 035422 (2012).

[90] H.-Z. Lu and S.-Q. Shen, *Physical Review B* **84**, 125138 (2011).

[91] H.-Z. Lu, J. Shi, and S.-Q. Shen, *Phys. Rev. Lett* **107**, 076801 (2011).

[92] M. Lang, L. He, X. Kou, P. Upadhyaya, Y. Fan, H. Chu, Y. Jiang, J. H. Bardarson, W. Jiang, E. S. Choi, *et al.*, *Nano Lett.* **13**, 48 (2013).

[93] J. J. Cha, M. Claassen, D. Kong, S. S. Hong, K. J. Koski, X.-L. Qi, and Y. Cui, *Nano Lett.* **12**, 4355 (2012).

[94] J. G. Checkelsky, Y. S. Hor, R. J. Cava, and N. P. Ong, *Phys. Rev. Lett* **106**, 196801 (2011).

[95] H. Steinberg, J.-B. Laloe, V. Fatemi, J. S. Moodera, and P. Jarillo-Herrero, *Phys. Rev. B* **84**, 233101 (2011).

[96] J. Chen, X. Y. He, K. H. Wu, Z. Q. Ji, L. Lu, J. R. Shi, J. H. Smet, and Y. Q. Li, *Phys. Rev. B* **83**, 241304 (2011).

[97] F. Mahfouzi, N. Nagaosa, and B. K. Nikolic, *Phys. Rev. Lett.* **109**, 166602 (2012).

[98] Y. Fan, P. Upadhyaya, X. Kou, M. Lang, S. Takei, Z. Wang, J. Tang, L. He, L.-T. Chang, M. Montazeri, *et al.*, *Nature Mater.* **13**, 699 (2014).

[99] P. Deorani, J. Son, K. Banerjee, N. Koirala, M. Brahlek, S. Oh, and H. Yang, *arXiv:* 1404.1146 (2014).

[100] Z. Zeng, T. A. Morgan, D. Fan, C. Li, Y. Hirono, X. Hu, Y. Zhao, J. S. Lee, J. Wang, Z. M. Wang, *et al.*, *AIP Advances* **3**, 072112 (2013).

[101] M. Bahramy, P. King, A. de la Torre, J. Chang, M. Shi, L. Patthey, G. Balakrishnan, P. Hofmann, R. Arita, N. Nagaosa, *et al.*, *Nature Communications* **3**, 1159 (2012).

VITA

Joon Sue Lee

Education:

Ph.D. in Physics, Pennsylvania State University, University Park, PA, 2014

M.S. in Physics, Seoul National University, Seoul, Korea, 2007

B.S. in Physics Education and Electrical Engineering, Seoul National University, Korea, 2005

Publications:

J. S. Lee, A. Richardella, R. D. Fraleigh, C.-X. Liu, W. Zhao, N. Samarth, "Engineering the Breaking of Time-reversal Symmetry in Gate-tunable Hybrid Ferromagnet/Topological Insulator Heterostructures", in preparation.

M. Jamali, **J. S. Lee**, Y. Lv, Z. Zhao, N. Samarth, J.-P. Wang, *arXiv:*1407.7940.

R. Mellnik, **J. S. Lee**, A. Richardella, J. L. Grab, P. J. Mintun, M. H. Fischer, A. Vaezi, A. Manchon, E.-A. Kim, N. Samarth, D. C. Ralph, *Nature* **511**, 449 (2014).

B. C. Chapler, K. W. Post, A. R. Richardella, **J. S. Lee**, J. Tao, N. Samarth, D. N. Basov, *Phys. Rev. B* **89**, 235308 (2014).

J. S. Lee, A. Richardella, D. W. Rench, R. D. Fraleigh, T. C. Flanagan, J. A. Borchers, J. Tao, N. Samarth, *Phys. Rev. B* **89**, 174425 (2014).

Z. Zeng, T. A. Morgan, D. Fan, C. Li, Y. Hirono, X. Hu, Y. Zhao, **J. S. Lee**, J. Wang, Z. M. Wang, S. Yu, M. E. Hawkridge, M. Benamara, and G. J. Salamo, *AIP Advances* **3**, 072112 (2013).

J. Wang, H. Li, C.-Z. Chang, K. He, **J. S. Lee**, X.-C. Ma, N. Samarth, Q.-K. Xue, M. Xie, M. H. W. Chan, *Nano Research* **5**(10), 739 (2012).

D. Zhang, J. Wang, A. DaSilva, **J. S. Lee**, H. R. Gutierrez, M. H. W. Chan, J. K. Jain and N. Samarth, *Phys. Rev. B* **84**, 165120 (2011).

R. Richardella, D. Zhang, **J. S. Lee**, D. Rench, A. Koser, A. L. Yeats, B. B. Buckley, D. D. Awschalom and N. Samarth, *Appl. Phys. Lett.* **97**, 262104 (2010).

S. W. Cho, H. K. Choi, **J. S. Lee**, D. Jeong, H. J. Kim, T. Hwang, K. H. Kim, and Y. D. Park, *Appl. Phys. Lett.* **91**, 122514 (2007).

H. Choi, **J. S. Lee**, S. W. Cho, W. O. Lee, S. B. Shim, and Y. D. Park, *J. Appl. Phys.* **101**, 063906 (2007).

J. S. Lee and G. Lee, *New Physics: Sae Mulli* (in Korean), **52** (2006).